Theoretical and physical modelling of the thermal performance of water wall systems

By

Ting WU

A thesis submitted in fulfilment of the requirements for the degree of

Master of Philosophy

School of Civil Engineering

Faculty of Engineering and Information Technologies

The University of Sydney

2016

This page is intentionally left blank.

Declaration

I hereby declare that the work presented in this thesis is solely my own work and that, to the best of my knowledge, the work is original except where otherwise indicated by reference to other authors. No part of this work has been submitted for any other degree or diploma.

Ting Wu

March, 2016

Acknowledgements

Abstract

Saving energy in buildings is critical for the combat against global energy crisis and climate change. For this purpose, a number of passive solar technologies have been developed for buildings, which have attracted a growing research interest over the last few decades. Among the various passive solar strategies, water wall is an excellent solution which can maintain thermal comfort in buildings while reducing energy consumption. Existing water wall studies are mainly based on simple heat balance models (HBM), in which convective heat transfer coefficients are assumed constant and the radiation exchange between internal surfaces is commonly neglected. Furthermore, the application of the Computational Fluid Dynamics (CFD) approach to water wall research is very rare and has been reported for steady state conditions only. These research gaps are addressed in this study through the development of a comprehensive transient heat balance model (THBM) and unsteady CFD modelling of water wall systems.

The thesis covers the following topics:

Firstly, in order to identify a proper turbulent model for the CFD study and examine the effect of internal surface-to-surface radiation transfer on the numerical solution of the convective flow, the turbulent natural convection with and without radiation transfer in two-dimensional (2D) and three-dimensional (3D) air-filled differentially heated cavities is numerically investigated using various RANS (Reynolds Averaged Navier-Stokes) turbulence models and the Discrete Ordinates radiation model. Both qualitative and quantitative data are presented to demonstrate the effects of radiation transfer on the numerical solution of the convective flow in the cavity and to evaluate the accuracy of five common two-equation RANS models. The numerical results are compared against published experimental and DNS (direct numerical simulation) data. It is found that the shear-stress transport (SST) k-ω model has the best overall performance in terms of capturing the main features of the flow and predicting time-averaged quantities.

Secondly, a comprehensive conjugate conduction-convection-radiation model for transient analysis of a semi-transparent water wall system is developed based on the conventional HBM. The THBM accounts for time variations of both internal and external convective heat transfer coefficients, the radiation emitted by external surfaces, and the

radiation exchanges between internal surfaces. The THBM is validated against both in-situ measurements and data produced by DesignBuilder, a commercial building energy simulation code. A good agreement between the predicted results of the THBM and DesignBuilder and the field data is achieved. The validated THBM is then adopted for various sensitivity analyses in order to explore the thermal performance of the semi-transparent water wall system under different configurations. It is found that reducing the transmissivity of the Perspex or glass walls is the most effective, practical and economical way to improve the thermal performance of the semi-transparent water wall system.

Finally, the thermal performance of an opaque water wall system is numerically investigated using the SST k-ω turbulence model and the Discrete Ordinates radiation model for typical winter and summer climate conditions in Sydney, Australia. With a periodic sol-air temperature specified on the external surface, the energy performance of the water wall system is examined over a range of water wall thicknesses. The CFD model is compared with the above experimentally validated THBM, and a fair agreement between the CFD model and the THBM results is achieved. The present numerical results indicate that the performance of the opaque water wall system is improved by increasing the thickness of the water column under the winter climate condition. It is also found that less supplementary energy is required in winter than that in summer in order to maintain a comfortable interior temperature. Further, a comparison between the present water wall system and a conventional concrete wall system shows that the water wall system performs significantly better than the concrete wall system of the same thickness in the winter climate of Sydney, whereas both the water wall and concrete wall systems have a similar performance in terms of energy savings in the summer climate of Sydney.

Table of Contents

List of Figures

List of Tables

List of Publications

Journal Papers

1. Wu, T. and Lei, C., 2015. On numerical modelling of conjugate turbulent natural convection and radiation in a differentially heated cavity. *International Journal of Heat and Mass Transfer*, 91, 454-466.

2. Wu, T. and Lei, C., 2016. A review of research and development on water wall for building applications. *Energy and Buildings*, 112, 198-208.

3. Wu, T. and Lei, C., Thermal modelling and experimental validation of a semi-transparent water wall system. To be submitted.

4. Wu, T. and Lei, C., CFD Simulation of the thermal performance of an opaque water wall system. *Solar Energy*, revision under review.

Conference Proceeding

1. Wu, T. and Lei, C., Comparison of various RANS models for conjugate turbulent natural convection with radiation in a cavity. *Proceedings of the 6th International Symposium on Advances in Computational Heat Transfer*, Rutgers University, Piscataway, USA, 25-29 May 2015. Paper No. CHT-15-093.

2. Wu, T. and Lei, C., Effect of tinting on the thermal performance of a semi-transparent water wall system. *Proceedings of the First Pacific Rim Thermal Engineering Conference, PRTEC*, March 13-17, 2016, Hawaii's Big Island, USA. Paper No. PRTEC-14593 (extended abstract).

1. Introduction

1.1 Background

At the present time, the energy consumption by residential and commercial buildings accounts for nearly one quarter of the total worldwide consumption of delivered energy and it is predicted that the building energy consumption will increase by approximately 1.6% per year from 2010 to 2040 [1]. Almost half of the building's energy consumption is for operating heating, ventilating, and air-conditioning (HVAC) systems [2]. Under this circumstance, saving energy from the HVAC systems in buildings becomes critical for the combat against the ongoing energy crisis and climate change.

Thermal energy storage (TES) is a technology that stores thermal energy over a particular period of time and releases the stored energy at a different time. It has a great potential for reducing the energy consumption in buildings. Over the past several decades, growing research interest has been devoted to this area [3]. The TES technologies for buildings can be classified into sensible heat storage and latent heat storage according to the media used for heat storage. In latent heat storage systems, a large amount of heat is stored or released during a phase change process (e.g. melting/solidification or gasification/liquefaction) of the storage medium. Phase change materials (PCMs) offer a high density for TES and require a smaller temperature difference between storing and releasing heat than sensible heat storage systems. However, PCMs also have some drawbacks. Inorganic PCMs are usually corrosive, unstable, and tend to delay solidification (supercooling), whereas organic PCMs are flammable and have relatively low volumetric latent heat storage capacity and low thermal conductivity [4, 5]. Moreover, no PCM is suitable for the full temperature range of all seasonal conditions even in a fixed location [6].

In sensible heat storage systems, heat is stored or released with the temperature change of the storage medium. Sensible heat storage materials with high heat capacities, such as concrete, brick and water, have been used as thermal mass in dwellings in order to moderate the temperature of internal spaces and to reduce the need for summer cooling and winter heating. Sensible heat storage materials can be used for both short-term TES and long-term TES. Short-term TES means that thermal energy is stored during the day and released during the night, whereas long-term TES often works over a yearly cycle of heat storage and release.

Among the various short-term TES systems, water wall is an excellent solution which can maintain thermal comfort in buildings while reducing energy consumption. The water wall system has unique advantages over other short-term TES technologies as it may allow part of the solar radiation to enter the buildings, and thus reduce the need for lighting during the daytime. The semi-transparent nature of the water wall system also gives the architecture aesthetic advantages over opaque walls. In addition, the cost of the water wall system is significantly lower than that of thermal storage walls using PCMs. Further, the heat stored in water may be redistributed by convection, and thus a water wall provides quicker heat exchange than a concrete or brick wall.

1.2 Literature Review

According to the different configurations, water walls can be generally grouped into the following four types: water wall with an opaque building envelope, water wall with a semi-transparent building envelope, water wall with PCMs, and water wall in conjunction with other passive technologies.

1.2.1 Water Wall with an Opaque Building Envelope

Water walls are often incorporated into an opaque building envelope such as metallic plates, opaque PVC pipes, concrete or insulation panels, which separate living spaces from the ambient (refer to Fig. 1.1). This is the basic configuration of water walls.
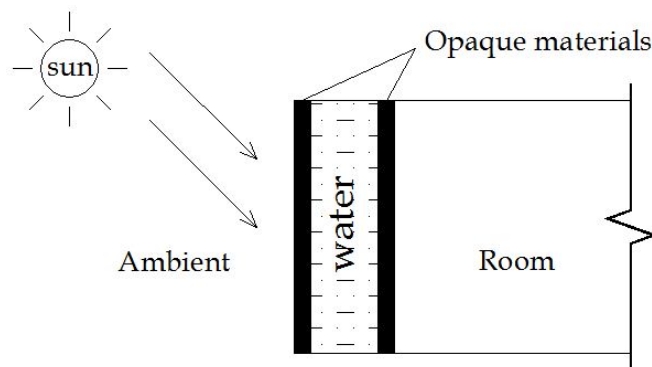
Fig. 1.1 Sketch of a water wall with an opaque building envelope.

The early research of opaque water wall was initially conducted by Balcomb & McFarland [7] and McFarland & Balcomb [8] using a simple empirical method called Solar Load Ratio Method. They estimated the thermal performance of a Trombe wall and a water wall with or without night-time insulation and with or without a reflector. The results showed that the

water wall achieved a higher monthly solar heating fraction (i.e. the percentage of the space heating load supplied by the passive solar system) than that of the Trombe wall. They also found that the performance of the water wall was enhanced by decreasing the R-value of the night-time insulation, the number of glazing and the wall absorptivity and by increasing the wall emissivity, the thermal storage capacity and the additional building mass.

Subsequently, a more realistic approach called heat balance model (HBM) has been developed for the water wall research and was widely adopted in the literature [e.g. 9-12]. The HBM is based on the energy conservation concept to establish energy balance associated with conductive, convective and radiative heat transfer in order to obtain surface and fluid (i.e. water and air) temperatures. This approach usually embodies the following four major assumptions [13]:

- uniform fluid (air or water) temperature throughout a selected zone
- uniform surface temperatures
- grey and diffuse radiative surfaces
- one-dimensional heat conduction through all the surfaces of interest

It is clear that the temperature stratification in the water column and the living space is neglected in the HBM. As a consequence, the HBM can only capture the main features of a system and is suitable for assessing the bulk performance of the system, rather than providing the details of temperature variations throughout the system. Nevertheless, this approach is highly effective and is capable of simulating large-scale systems over an extended period of time. Therefore, the HBM can be used for energy savings analysis over a daily, monthly or even yearly cycle.

By adopting the HBM, the thermal performance of the opaque water wall has been extensively investigated through various comparisons between the opaque water wall and other passive technologies [e.g. 14, 15]. It is commonly reported that the opaque water wall system produced a less room temperature fluctuation than other thermal storage water wall systems, such as Trombe wall [16], and a better thermal performance can be achieved by increasing the capacity of water storage [17].

Experimental modelling is another direct and effective way to investigate the thermal performance of the opaque water wall systems. The application of an opaque water wall system in a residential house was reported by Sutton & McGregor [18]. They built two passive solar heating houses to compare a north-facing concrete wall with a water storage wall in Australia. The monitored data showed that the house with the opaque water wall saved more than half of

the annual energy consumption for heating compared to the conventional house with the concrete wall. Turner et al. [19] fabricated a water wall comprising 7.6-cm diameter opaque plastic tubes embedded into a conventional stud wall. The system was operated over a 24-hour cycle including 6 hours active charge with hot ambient air during the day and 18 hours passive discharge. The results showed that the wall temperature was still 2.6°C higher than the room temperature after 18 hours of discharge, which reduced the heating load of the house.

Apart from the residential applications described above, opaque water wall in greenhouse has also attracted much research attention. Sørensen [20] carried out a full-scale prototype experiment in a 12-m^2 greenhouse in Denmark with four black-painted drums containing 0.8-m^3 water. It was reported that a considerable stratification formed in the drums with the bottom temperature 4~10°C lower than the top temperature, depending on the season. With the assistance of the inexpensive thermal energy storage by water, the air temperature inside the greenhouse was maintained at approximately 5~8°C above the outside temperature in winter. The experimental models of the greenhouse are also used for the validation of the HBMs. The TES effect of a water wall in a passive greenhouse has been studied in [21-23]. Their results indicated that the water wall offered a much higher room air temperature than the ambient in winter and the air temperature fluctuation inside the room decreased with the increase of the water mass. A fair agreement between the predicted and experimental results was reported in the above investigations.

Whilst the analytical methods such as the HBM and the experimental modelling have been investigated extensively, few papers have reported computational fluid dynamics (CFD) modelling of the opaque water wall systems. CFD is a powerful numerical approach that has been widely adopted to solve a wide range of scientific and engineering problems [e.g. 24-26] which can account for the complex heat transfer processes and resolve full details of the convective flows in both water and air. Karabay et al. [27] studied the thermal performance of a concrete wall with embedded water pipes filled with constant-temperature water using the Shear Stress Transport (SST) *k-ω* turbulence model coupled with Surface-to-Surface radiation model. The model was two-dimensional (2D) and the flow was assumed to be turbulent. The simulations were performed for steady state conditions only. A comparison of the water pipe wall heating system and a floor heating system showed that a better thermal comfort condition with the thermal stratification of less than 1°C/m was achieved in the water pipe wall heating system.

1.2.2 Water Wall with a Semi-transparent Building Envelope

Water wall can also be coupled with a semi-transparent outside building façade such as light-permeable plastic or glass, which allows part of the sunlight to penetrate from outside into the water wall. The internal side of the water wall can be either semi-transparent or opaque (refer to Fig. 1.2), and depending on the material of the internal wall, sunlight may penetrate further into the room.
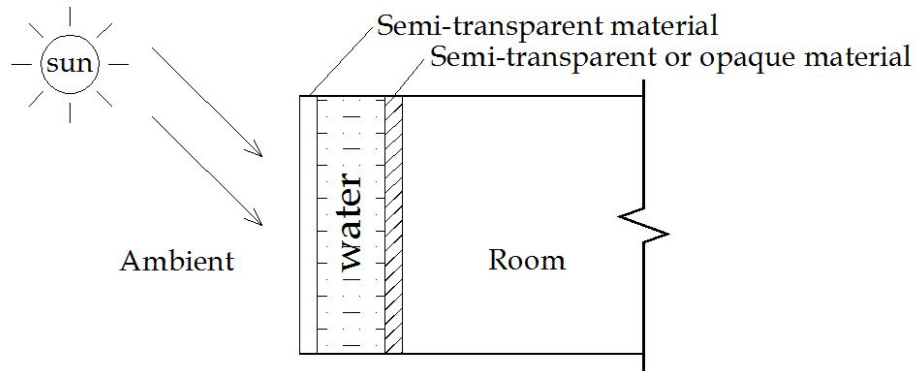
Fig. 1.2 Sketch of a water wall with a semi-transparent building envelope.

The studies of the semi-transparent water wall have been investigated experimentally and analytically using the HBM by many researchers. Among the experimental investigations, Fernández-González [28] summarised the thermal performance of five different passive solar test-cells (direct gain, Trombe wall, water-tube wall, sunspace, and roof pond). For the water-tube wall, four translucent water tubes, each holding 0.25 m^3 of water, were installed in an 11.9 m^2 (4.88 m by 2.44 m) test-cell. The results showed that, despite its large thermal storage capacity (e.g. 2.84 times the thermal storage capacity of the Trombe wall test-cell), the water-tube wall test-cell had the second highest maximum swing of the diurnal operative temperature, surpassed only by the direct gain test-cell. Adams et al. [29] conducted a comparative laboratory experiment in order to obtain the optimal thickness of the water column in a small-scale semi-transparent water wall. They used a halogen bulb to simulate solar irradiation. Three different water column thicknesses (i.e. 3", 6" and 9" respectively) were tested by turning on the heat source for 5 hours, then switching off the heat source and monitoring the temperature changes of the water and the room. The results showed that the three-inch water wall could not regulate the room temperature as the other water walls with larger thicknesses, and the room temperature variation associated with the six and nine-inch water walls was minimal.

The analytical study of the thermal performance of water storage walls under five different configurations was initially carried out by Balcomb et al. [30]. Their results indicated that the

water storage placed at the back of a glass panel and that placed at the back of a transparent insulation panel performed appreciably better than the others. Using building energy simulation (BES) program SolPass, Liu & Feng [31] compared the performance of a Trombe wall and a semi-transparent water-tube wall for optimising indoor thermal environment and reducing building energy consumption. Their simulation results indicated that the semi-transparent water-tube wall obtained more than ten times solar gains than that of the Trombe wall in winter.

A popular configuration of the semi-transparent water wall is transwall, which has a semi-transparent baffle inside the water column. The transwall was first designed by Fuchs & Mcclelland [32], who compared the thermal performance of the transwall with a Trombe wall and a direct solar gain system. They found that the solar heating fraction in the transwall passive heating system could be very close to or exceed that of the Trombe wall. Recently, a transparent water storage envelope (TWSE) module, which was very similar to the transwall, was developed by Liu & Shen [33, 34] for improving the overall energy efficiency of commercial buildings. They investigated the thermal resistance and thermal inertia index of a 378-mm thick TWSE module and suggested that the water should be discharged in winter and replaced by air in order to achieve effective thermal insulation.

The quest for understanding the thermal performance of transwall motivated a number of comparative studies. Nayak [35, 36] compared the thermal performance of several different types of thermal storage walls, including Trombe wall, transwall, water Trombe wall and water concrete wall. It was found that the transwall was more effective than other walls in meeting the daytime heating load. However, the water Trombe wall and the water concrete wall are better from the viewpoints of reducing temperature swings and the overall day-and-night performance. Tiwari [37] and Tiwari et al. [38] compared the thermal performance of various south-facing walls, namely glass wall, active air collector wall opaque water wall, transwall and isothermal mass under winter condition. The results showed that the transwall and the opaque water wall were preferred for residential heating at night, whereas the glass wall and the air collector wall were desirable for heating during sunshine hours. An overall better performance was achieved in the transwall than that of the isothermal mass and the water wall.

A number of studies have considered optimising the thermal performance of a semi-transparent water wall. Among them, Sodha et al. [39] investigated the effects of a trap material inside a transwall and the thickness distribution of the transwall on the thermal performance. They found that the thickness of the water column between the trap and the outside glazing should be smaller than the thickness of the water column between the trap and the room in order to obtain a lower temperature fluctuation of the system. Following the above investigation,

Upadhya et al. [40] studied the optimum distribution of the water column thickness in the transwall for a heated room. The results showed that, when the water columns inside and outside of the trap material were of an equal thickness, the water temperature, the indirect gain and the heat flux from the wall to the room were maximised, and the room air temperature fluctuation was minimised.

The application of the transwall in a horticultural glasshouse has been studied analytically by Nisbet & Kwan [41]. Two 2.3-m transwalls consisting of clear plastic bags filled with water-dye mixture were erected behind external glazing. The annual energy savings of this system was reported to be around 20%, depending on evapotranspiration, for two sites including the West of Scotland and Southeast England. Nisbet & Mthembu [42] also investigated the energy savings potential of a water-dye filled transwall module and a water-gel filled transwall module in a conventional residential house in the UK. It was concluded that a transwall module filled with a water-dye solution released more heat during the evening compared with the water-gel filled module of a similar size. The optimum dye concentration of Lissamine Red 3GX was 20 ppm and the optimum water column thickness was about 150 mm for the weather conditions of western Scotland and southern France.

1.2.3 Water Wall with Phase Change Materials

Although water wall has almost the largest heat capacity among the sensible heat storage systems, its heat capacity is still relatively small compared to that of the latent heat storage systems (e.g. PCMs). The conjunctive use of water wall with PCMs may take the advantages of both the water wall and the PCMs and thus achieve better thermal performance. The PCMs may be placed at the external side, internal side or both sides of the water wall (refer to Fig. 1.3), resulting in different thermal performance. PCMs in conjunction with a water wall to form a link wall in a sunspace for a cold climate were examined in [43]. The thermal performance of this composite water/PCM wall was compared with several other configurations including a sunspace without a link wall, a sunspace with a water wall as a link wall, a sunspace with a PCM wall as a link wall and a sunspace with movable insulation panels. They found that the combined PCMs and water wall as a link wall gave the best thermal performance among all the configurations. The lowest temperature fluctuation was observed when the thickness of the water wall and the PCM wall was equal, and a comfortable temperature for the living space was achieved when the ambient temperature was around 0°C.
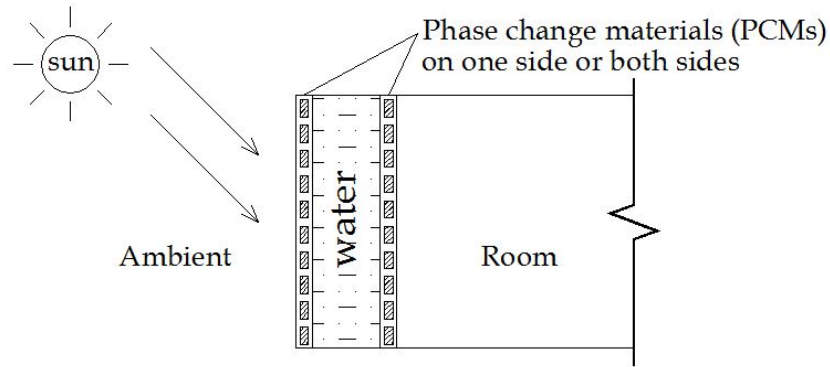
Fig. 1.3 Sketch of a water wall with PCMs.

A novel passive solar heating system using PCMs in heat pipes to collect and transfer solar energy to a short-term TES (refer to Fig. 1.4) was described in [44]. Unlike the conventional PCMs described above, the purpose of the PCMs in the heat pipes is to accelerate heat transfer between the ambient and the interior heat storage medium rather than using its high heat capacity. In this system, solar thermal energy was absorbed by an absorber plate and the absorbed heat was transferred to the PCMs inside the heat pipes by conduction. The liquid form of the PCMs in the evaporator end of the heat pipes thus vaporised due to the heat from solar energy and the PCM vapour rose to the condenser end, where it condensed and released its latent heat to the water wall. The resultant condensate then flowed back to the lower end of the heat pipes by gravity, completing the full thermal cycle.
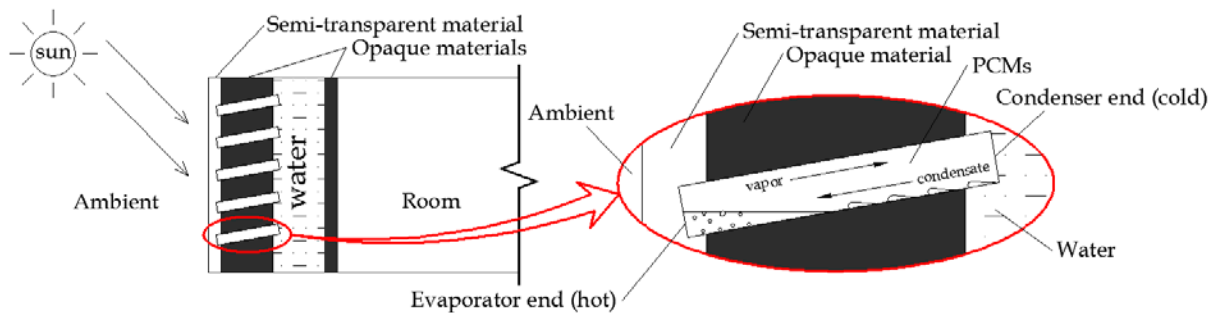
Fig. 1.4 Schematic of a water wall with heat pipes [45].

Susheela & Sharp [45] designed a passive solar heat pipe augmented system using the above-described concept as the system illustrated in Fig. 1.4 in a south-facing water wall of a building. Their experimental and simulation results indicated that the heat loss from water wall to the ambient reduced significantly during night time and in cold cloudy climates. It was also found that such a heat pipe augmented water wall system provided 52.2% to 107% more solar thermal energy than the conventional concrete wall and 16.6% to 59.8% more thermal energy than the water wall in three different locations in the USA.

Recently, Albanese et al. [46] developed a HBM for a passive solar space heating system utilising heat pipes to transfer latent heat to a storage water tank inside the building. A bench-scale experimental model was constructed to verify the HBM. It was found that the solar heat pipe system gave a significantly higher solar heating fraction than the other passive technologies, especially in cold and cloudy climates, and a good agreement was obtained between the HBM and the laboratory experiment. In order to further validate the above-described HBM and the bench-scale experiment, a full-scale prototype of the heat pipe system was designed and tested in [47] in a classroom at the University of Louisville during the spring heating season of 2010. Their field results indicated that the thermal storage water tank was heated to a sufficiently high temperature to supply heat to the classroom even during the coldest days of the season. During a long period (4 consecutive days) of low solar isolation, the average hourly heat delivery to the classroom remained positive and was never less than 16.6 W/m^2. Again, a good agreement between the HBM prediction and field data of full-scale prototype was achieved. An improved design of the passive heat pipe system was tested alongside the previous prototype during January to February of 2013 by Robinson & Sharp [48]. Significant improvement in increasing the heat transfer to the classroom and reducing heat losses was achieved by adding a copper absorber, thicker insulation, a rubber adiabatic section and exposing one condenser directly to the room air.

The above-described passive heat pipe system can also be used to reduce unwanted solar gains during the cooling season. Robinson & Sharp [49] investigated the effectiveness of several control strategies and design modifications for the heat pipe system to reduce unwanted thermal gains by means of the HBM, the bench-scale experiments and the full-scale prototype. Their results revealed that the maximum annual energy savings were achieved by utilising a control strategy based on ambient temperature, for which the mechanism was applied when the forecast ambient temperature for the next hour was higher than 18.3^{o}C. The best design modification was using mechanical valves to stop two-phase change in the heat pipes, which can eliminate unwanted solar gains and produce the lowest total annul energy consumption.

1.2.4 Water Wall in Conjunction with Other Passive Technologies

With a sunspace

Sunspace is a direct gain system, whereas water wall is an indirect gain system. When a water wall and a sunspace are adopted together (refer to Fig. 1.5), the solar gains and the thermal performance of the passive solar heating strategy may be improved significantly.
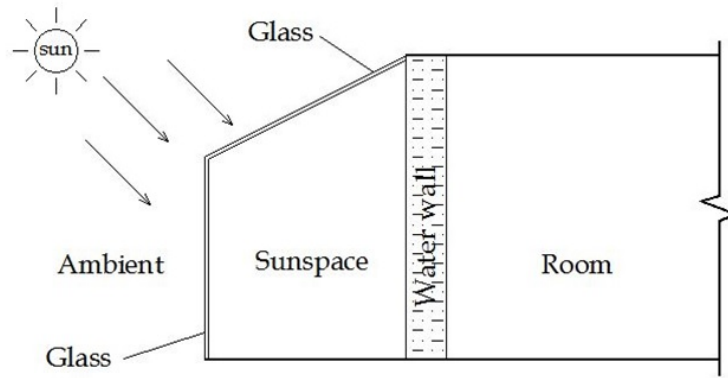
Fig. 1.5 Sketch of a water wall combined with sunspace.

An opaque water wall acting as the link wall between the sunspace and the living space in a single-storey residential house was carried out by Yadav & Tiwari [50]. Their results showed that the water wall combined with the sunspace resulted in significant reduction of the temperature fluctuation in the living space. It was also reported that, for such a system with a 0.05-m thick water wall, a quasi-steady state was achieved in the system within 3-4 days. Further, it was found that the temperatures of both the sunspace and the living space reduced when the thickness of the water wall was increased from 0.05 m to 0.10 m.

The comparison of water wall with sunspace and other passive solar strategies is of great interest for many researchers. Tiwari & Kumar [51] conducted a comparative study of the thermal performance of an opaque water wall, a transwall and an air collector in a sunspace. According to their calculations, the transwall as a link wall produced the highest room air temperature in winter night among the three different configurations considered in their investigation. Another comparative study of various passive heating strategies including a glass wall, a semi-transparent water wall, a sunspace, a wall air heater and a roof air heater was carried out by Tiwari & Singh [52]. They found that the use of a semi-transparent water wall in a sunspace can significantly reduce the fluctuation of the temperature and the peak temperature was shifted towards the night time. The minimum temperature fluctuation was achieved with the configuration of sunspace + water wall + roof air heater.

The experimental prototypes of an attached sunspace with water storage were constructed by Sánchez-Ostiz et al. [53] in order to explore their thermal performance. The results showed that a sunspace with water for TES improved the indoor thermal comfort of the adjacent room during both winter and summer. The experimental data was also used to validate a BES model (TRNSYS). A fair agreement between the experimental data and the numerical simulation performed using the TRNSYS model was reported.

With a solar chimney

Solar chimney is a passive strategy for enhancing stack-driven ventilation by buoyancy [54]. When incorporating a water wall into the solar chimney (refer to Fig. 1.6), the night time ventilation of the solar chimney is expected to be improved.
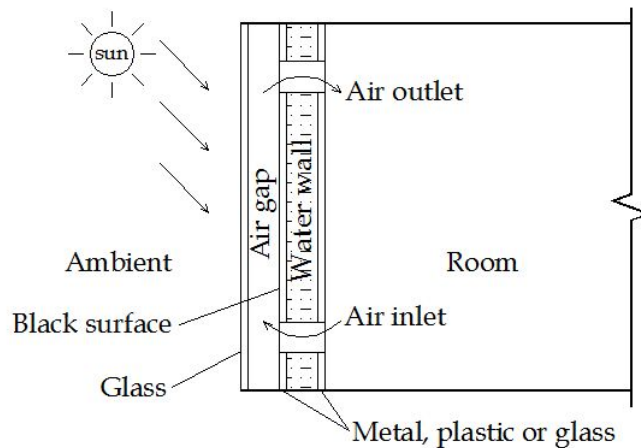
Fig. 1.6 Sketch of a water wall with solar chimney (self-ventilation mode).

A coupled analytical and experimental study of natural ventilation in a passive solar house by solar chimney integrated with a water thermal storage wall was conducted by Wang et al. [55, 56]. A water thermal storage wall with a total of 41 tons of water was retrofitted to the single-storey passive solar house with a floor area of 700 m². The results obtained with TRNSYS software showed that active cooling was not required in summer as the extreme indoor temperature of 35°C was exceeded for only 47 out of 8760 hours. In winter, the measured indoor air temperature remained at 13.7°C under the condition of no space heating when the outside air temperature dropped to -0.4°C. Therefore, the combined water wall with natural ventilation system can significantly reduce the required heating and cooling loads. Compared with massless walls, this passive system may reduce the maximum indoor temperature by up to 4°C in summer and increase the minimum indoor temperature by up to 3°C in winter.

With evaporative cooling

Evaporative cooling works by adding water vapour into air, resulting in the decrease of the air temperature and the increase of its water content. When the evaporative cooling is coupled with the water wall, the thermal comfort in terms of both temperature and humidity may be improved. Moustafa & Aripin [57] evaluated the thermal performance of combined water wall and porous ceramic pipes for evaporative cooling in a hot arid climate using CFD simulation. A three-dimensional (3D) model with inner dimensions of 5m × 5m × 3m (L × W × H) was

established using ANSYS Workbench, and ANSYS Fluent was used for the simulation of heat transfer using a laminar flow model coupled with the Rosseland radiation model. Steady-state simulation was conducted for every hour during the 24 hours of one typical summer day and one typical winter day, representing the extreme weather conditions in Luxor, Egypt. They found that using this type of water wall, the room temperature was 4~10°C cooler than the outdoor temperature in summer and was 4~15°C higher than the outdoor temperature in winter.

1.2.5 Summary

The above review provides important insights into the current status of research and development in water wall systems for both residential and commercial buildings and the relevant research methodologies. It is evident that the water wall has the capacity to moderate large temperature swings between the day and night and has a great potential for maintaining thermal comfort and cutting energy consumption in buildings.

A number of different configurations of water wall systems have been studies previously, and they can be generally grouped into four types: (1) a water wall with an opaque building envelope; (2) a water wall with a semi-transparent building envelope; (3) a water wall with PCMs; and (4) a water wall in conjunction with other passive technologies. The different configurations have different thermal performance, and thus are suitable for different applications, depending on the location and/or the season.

The above literature survey shows three types of approaches have been adopted in the water wall research including analysis using the HBM, experimental modelling and CFD modelling. Fig. 1.7 shows a statistics of the publicly available research papers on water wall systems for TES and thermal comfort purpose. It is seen in this figure that the research on water wall systems did not receive much attention before 1980's, and back then the HBM was the only method applied to this research. However, significant research attention was paid to water wall systems in the 1980's. During that period of time experimental modelling was also adopted in water wall research, though the majority of the studies were still based on the HBM. In the subsequent two decades, the research interest on water wall seemed to decline, and the methods adopted in the water wall research were still limited to the HBM and experimental modelling. It is worth noting that the water wall has attracted significant research interest again over the past few years, and for the first time, the CFD approach has been applied to the water wall research over this period of time although it is for steady state conditions only.
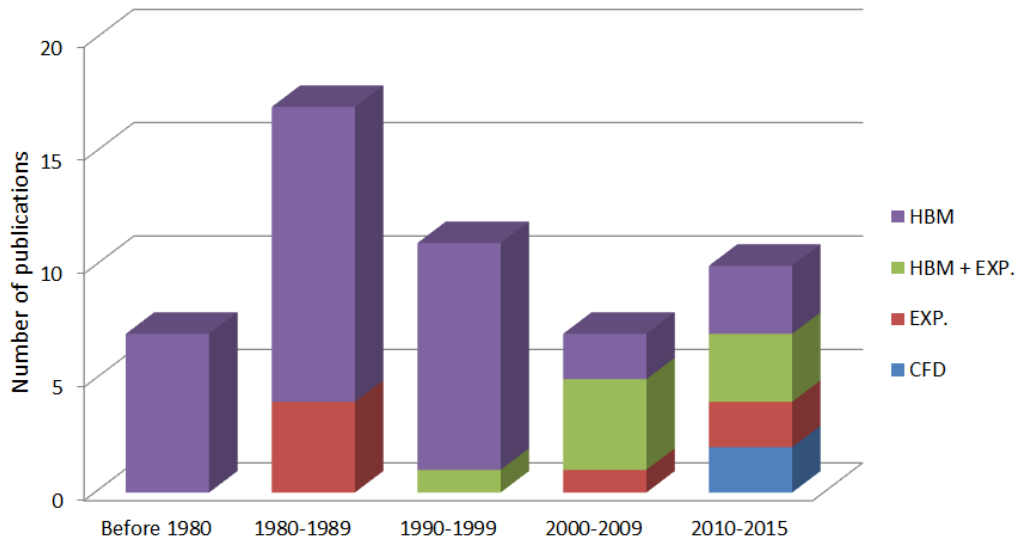
Fig. 1.7 Statistics of the research publications related to water wall for thermal comfort and thermal energy storage.

It is clear that the majority of the previous investigations have adopted the HBM which can produce data for a quick assessment of the system performance. However, the HBM has many limitations as it cannot resolve the details of the complex heat transfer processes occurring both inside the water wall and in the adjacent space. In contrast, the CFD approach can account for the complex heat transfer processes and resolve full details of the convective flows in both water and air. However, the application of the CFD approach to water wall research is still in its infancy, which is in part due to the fact that the CFD modelling of building systems is usually very resource-intensive.

The above literature review has also revealed a number of contradictory claims reported in the literature. For instance, Balcomb et al. [30] concluded that a water wall was better than a double-glass wall in a winter application, whereas Liu & Shen [34] argued that the water wall should be converted into a double-glass wall because water was not a prominent heat insulating material compared with air. Another example of contradicting claims is regarding the heat flux entering a heated space through transwall. Sodha et al. [39] found that the thickness of the water column between the trap and the outside glazing should be smaller than the width of the water column between the trap and the room. However, Upadhya et al. [40] reported that the thickness of the inside water column of the transwall should be minimised. These controversies suggest that, although much attention has been paid to the water wall research, the understanding of the complex flow and heat transfer processes in water wall systems is still incomplete. Moreover, there are still many gaps in the available information about the flow and heat transfer processes

in water wall systems. A particular issue which is important but has been commonly ignored in the existing literature is the temperature stratification in the water column and in the adjacent space. The issue may be resolved by running a CFD model of the physical system. Therefore, further attention should be paid to the water wall research in order to advance our understanding of the water wall systems and to guide the design of such systems.

1.3 Thesis Aims

As reviewed above, the HBM has dominated the water wall research for over three decades. However, the existing HBMs suffer from two major deficiencies. Firstly, the convective heat transfer coefficients embodied in the HBMs have been assumed constant in all the models. And secondly, the radiation exchange between internal surfaces is commonly neglected in the HBMs. Moreover, the CFD approach is only applied to the water wall research under steady state conditions. Therefore, the aims of the thesis are:

1. Identifying a proper turbulence model for the CFD study of the water wall system and examining the effect of radiation transfer on the thermal stratification of the convective flow in an air-filled differentially heated cavity.

2. Developing a transient heat balance model (THBM), accounting for time variations of both internal and external convective heat transfer coefficients and the internal surface-to-surface radiation exchange, for describing the thermal behaviour of a water wall system, and further validating the model by a reduced-scale prototype experiment under the real climate conditions in Sydney, Australia.

3. Modelling an opaque water wall system using a transient CFD model, investigating the effect of the thickness of the water column on the thermal behaviour of the water wall system, and comparing its thermal performance with a conventional concrete wall model under different climate conditions.

1.4 Thesis Outline

The outline of this thesis is as follows:

Chapter 1 presents background of this study along with a comprehensive literature survey of water wall research and development for building applications.

Chapter 2 evaluates the accuracy of five common two-equation RANS models on the numerical solution of turbulent natural convection in an air-filled differentially heated cavity

with reference to published experimental and direct numerical simulation data. The effects of three-dimensionality, radiation transfer and thermal boundary conditions on the predicted convective flow in the cavity are also examined.

Chapter 3 develops a transient conjugate conduction-convection-radiation HBM for the analysis of a semi-transparent water wall system based on the conventional HBM. The THBMs of both the water wall and an alternative concrete wall model are validated against filed measurements under real climate conditions in Sydney, Australia. The validated THBM is then adopted in a sensitivity analysis in order to assess the thermal performance of the semi-transparent water wall system under different configurations.

Chapter 4 numerically investigates the diurnal thermal performance of an opaque water wall system using the above-identified RANS model in Chapter 2. The effect of the thickness of the water column is studied in terms of temperature stratification, temperature fluctuation and the heat flux entering into a temperature-regulated room. A comparison of the water wall and the concrete wall is also carried out under both winter and summer climate conditions.

Chapter 5 summarises the major findings of the present research and makes recommendations for future research and development.

References

[1] Energy Information Administration, International Energy Outlook 2013, U.S. Department of Energy, 2013.

[2] L. Pérez-Lombard, J. Ortiz, C. Pout, A review on buildings energy consumption information, Energy and Buildings, 40 (3) (2008) 394–398.

[3] V. Basecq, G. Michaux, C. Inard, P. Blondeau, Short-term storage systems of thermal energy for buildings: a review, Advances in Building Energy Research, 7 (1) (2013) 66–119.

[4] F. Kuznik, D. David, K. Johannes, J.J. Roux, A review on phase change materials integrated in building walls, Renewable and Sustainable Energy Reviews, 15 (1) (2011) 379-391.

[5] L.F. Cabeza, A. Castell, C. Barreneche, A. De Gracia, A.I. Fernández, Materials used as PCM in thermal energy storage in buildings: A review, Renewable and Sustainable Energy Reviews, 15 (3) (2011) 1675-1695.

[6] A. Pasupathy, R. Velraj, Effect of double layer phase change material in building roof for year round thermal management, Energy and Buildings, 40 (3) (2008) 193–203.

[7] J.D. Balcomb, R.D. McFarland, A simple empirical method for estimating the performance of a passive solar heated building of the thermal storage wall type, in: 2nd National Passive Solar Conference, 1978.

[8] R.D. McFarland, J.D. Balcornb, Effect of design parameter changes on the performance of thermal storage wall passive systems, in: 3rd National Passive Solar Conference, 1979.

[9] D.K. Dutt, S.N. Rai, G.N. Tiwari, Y.P. Yadav, Transient analysis of a winter greenhouse, Energy Conversion and Management, 27 (2) (1987) 141-147.

[10] S.C. Kaushik, S. Kaul, Thermal comfort in buildings through a mixed water-mass thermal storage wall, Building and Environment, 24 (3) (1989) 199-207.

[11] N.K. Bansal, P.C. Thomas, A Simple procedure for selection and sizing of indirect passive solar heating systems, Building and Environment, 26 (4) (1991) 381-387.

[12] M.S. Bhandari, N.K. Bansal, Solar heat gain factors and heat loss coefficients for passive heating concepts, Solar Energy, 53 (2) (1994) 199-208.

[13] C.O. Pedersen, D.E. Fisher, R.J. Liesen, Development of a Heat Balance Procedure for Calculating Cooling Loads, ASHRAE Transactions, 103 (2) (1997) 459-468.

[14] M.S. Sodha, S.C. Kaushik, J.K. Nayak, Performance of trombe walls and roof pond systems, Applied Energy, 8 (3) (1981) 175-191.

[15] M.S. Sodha, S.C. Bhardwaj, S.C. Kaushik, Thermal load leveling of heat flux through an insulated thermal storage water wall, Energy Research, 5 (2) (1981) 155-163.

[16] J.K. Nayak, N.K. Bansal, M.S. Sodha, Analysis of passive heating concepts, Solar Energy, 30 (1) (1983) 51-69.

[17] M.S. Sodha, J. Kaur, R.L. Sawhney, Effect of storage on thermal performance of a building, International Journal of Energy Research, 16 (8) (1992) 697-707.

[18] R.G. Sutton, R.J. McGregor, Solarwall project: two demonstration houses with passive solar heating in Tasmania, Architectural Science Review, 29 (1) (1986) 2-11.

[19] R.H. Turner, G. Liu, Y.A. Cengel, C.P. Harris, Thermal storage in the walls of a solar house, Journal of Solar Energy Engineering, 116 (4) (1994) 183-193.

[20] B. Sørensen, Experiments with energy-storage in a high-latitude greenhouse, Solar Energy, 42 (4) (1989) 293-301.

[21] Govind, Rashmi, N.K. Bansal, I.C. Goyal, An experimental and theoretical study of a plastic film solar greenhouse, Energy Conversion and Management, 27 (4) (1987) 395-400.

[22] A. Gupta, G.N. Tiwari, Computer model and its validation for prediction of storage effect of water mass in a greenhouse: a transient analysis, Energy Conversion and Management, 43 (18) (2002) 2625–2640.

[23] M. Din, G.N. Tiwari, M.K. Ghosal, N.S.L. Srivastava, NSL, M. Imran Khan, M.S. Sodha, Effect of thermal storage on the performance of greenhouse, International Journal of Energy Research, 27 (1) (2003) 79–92.

[24] R. Khanal, C. Lei, Flow reversal effects on buoyancy induced air flow in a solar chimney, Solar Energy, 86 (9) (2012) 2783–2794.

[25] S. Hussain, P.H. Oosthuizen, Numerical investigations of buoyancy-driven natural ventilation in a simple three-storey atrium building and thermal comfort evaluation, Applied Thermal Engineering, 57 (1) (2013) 133-146.

[26] B.K. Koyunbaba, Z. Yilmaz, K. Ulgen, An approach for energy modeling of a building integrated photovoltaic (BIPV) Trombe wall system, Energy and Buildings, 67 (2013) 680–688.

[27] H. Karabay, M. Arıcı, M. Sandık, A numerical investigation of fluid flow and heat transfer inside a room for floor heating and wall heating systems, Energy and Buildings, 67 (2013) 471-478.

[28] A. Fernández-González, Analysis of the thermal performance and comfort conditions produced by five different passive solar heating strategies in the United States midwest, Solar Energy, 81 (5) (2007) 581-593.

[29] S. Adams, M. Becker, D. Krauss, C. Gilman, Not A dry subject: optimizing water trombe walls, in: Proceedings of Solar 2010 ASES conference, 2010.

[30] J.D. Balcomb, J.C. Hedstrom, R.D. Mcfarland, Simulation analysis of passive solar heated buildings - preliminary results, Solar Energy, 19 (3) (1977) 277-282.

[31] Y. Liu, W. Feng, Integrating passive cooling and solar techniques into the existing building in South China, Advanced Materials Research, 368 (2012) 3717-3720.

[32] R. Fuchs, J.F. Mcclelland, Passive solar heating of buildings using a transwall structure, Solar Energy, 23 (2) (1979) 123-128.

[33] X. Liu, T. Shen, Conceptual development of transparent water storage envelopes, Architectural Science Review, 50 (1) (2007) 18-25.

[34] X. Liu, T. Shen, The development of transparent water storage envelopes (TWSE) through theoretical thermal and optical analyses, Architectural Science Review, 51 (2) (2008) 109-123.

[35] J.K. Nayak, Thermal performance of a water wall, Building and Environment, 22 (1) (1987) 83-90.

[36] J.K. Nayak, Transwall Versus Trombe Wall - Relative Performance Studies, Energy Conversion and Management, 27 (4) (1987) 389-393.

[37] G.N. Tiwari, Design of a non-airconditioned passive solar house for the cold climate of Srinagar, Building and Environmnent, 26 (4) (1991) 371-380.

[38] G.N. Tiwari, M. Upadhya, S.N. Rai, Relative thermal performances of south walls in winter, Energy and Buildings, 17 (4) (1991) 313-320.

[39] M.S. Sodha, N.K. Bansal, S. Ram, Periodic analysis of a transwall: a passive heating concept, Applied Energy, 14 (1) (1983) 33-48.

[40] M. Upadhya, G.N. Tiwari, S.N. Rai, Optimum distribution of water-wall thickness in a transwall, Energy and Buildings, 17 (2) (1991) 97-102.

[41] S.K. Nisbet, C.M. Kwan, The application of the transwall to horticultural glasshouses, Solar Energy, 39 (6) (1987) 473-482.

[42] S.K. Nisbet, N.S. Mthembu, Transwall modeling using effective conductivities, Solar Energy, 49 (2) (1992) 127-138.

[43] G.N. Tiwari, Y.P. Yadav, S.A. Lawrence, Performance of a solarium: An analytical study, Building and Environment, 23 (2) (1988) 145-151.

[44] W.J. Rice, Performance of passive and hybrid solar heating systems, International Journal of Ambient Energy, 5 (4) (1984) 171-186.

[45] N. Susheela, M.K. Sharp, Heat pipe augmented passive solar system for heating of buildings, Journal of Energy Engineering, 127 (1) (2001) 18-36.

[46] V. Albanese, S. Robinson, G. Brehob, M.K. Sharp, Simulated and experimental performance of a heat pipe assisted solar wall, Solar Energy, 86 (5) (2012) 1552-1562.

[47] B.S. Robinson, E. Chmielewski, A. Knox-Kelecy, G. Brehob, M.K. Sharp, Heating season performance of a full-scale heat pipe assisted solar wall, Solar Energy, 87 (2013) 76-83.

[48] B.S. Robinson, M.K. Sharp, Heating season performance improvements for a solar heat pipe system, Solar Energy, 110 (2014) 39–49.

[49] B.S. Robinson, M.K. Sharp, Reducing unwanted thermal gains during the cooling season for a solar heat pipe system, Solar Energy, 115 (2015) 16–32.

[50] Y.P. Yadav, G.N. Tiwari, Analytical model of a solarium for cold climate - a new approach, Energy Conversion and Management, 28 (1) (1988) 15-20.

[51] G.N. Tiwari, S. Kumar, Thermal evaluation of solarium-cum-passive solar house, Energy Conversion and Management, 32 (4) (1991) 303-310.

[52] G.N. Tiwari, A.K. Singh, Comparative studies of different heating techniques of a non-air conditioned building, Building and Environment, 31(3) (1996) 215-224.

[53] A. Sánchez-Ostiz, A. Monge-Barrio, S. Domingo-Irigoyen, P. González-Martínez, Design and experimental study of an industrialized sunspace with solar heat storage, Energy and Buildings, 80 (2014) 231–246.

[54] R. Khanal, C. Lei, Solar chimney—A passive strategy for natural ventilation, Energy and Buildings, 43 (8) (2011) 1811–1819.

[55] W. Wang, Z. Tian, X. Niu, X. Xu, Investigation on a passive solar house equipped with water thermal storage wall, Applied Mechanics and Materials, 178 (2012) 193-196.

[56] W. Wang, Z. Tian, Y. Ding, Investigation on the influencing factors of energy consumption and thermal comfort for a passive solar house, Energy and Buildings, 64 (2013) 218–223.

[57] M.A. Moustafa, S. Aripin, CFD evaluation of the pottery water wall in a hot arid climate of Luxor, Egypt, Journal of Green Building, 9 (4) (2014) 175-189.

2. On Numerical Modelling of Conjugate Turbulent Natural Convection and Radiation in a Differentially Heated Cavity

Statement of contribution to co-authored publication

This chapter is based on a co-authored peer-reviewed paper. The bibliographic details of the paper, including all authors, are:

Wu, T. and Lei, C., 2015. On numerical modelling of conjugate turbulent natural convection and radiation in a differentially heated cavity. *International Journal of Heat and Mass Transfer*, 91, 454-466.

My contribution to the paper includes reviewing the pertinent literature, building and implementing the numerical model, collecting and analysing the numerical data, and drafting the paper.

Signed: _____ Date: ___2; 0250⁄4238_____

Ting Wu

Countersigned: _____ Date: ___10/03/2016_____

Co-author: A/Prof. Chengwang Lei (Supervisor, School of Civil Engineering, The University of Sydney)

2.1 Introduction

Conjugate natural convection with radiation transfer in a differentially heated cavity has many applications such as in building HVAC (heating, ventilation and air-conditioning) systems, solar collectors and water walls etc. Therefore, extensive theoretical, experimental and numerical studies on this topic have been reported over the past several decades (see e.g. [1-3]). In most practical applications, the convective flow is turbulent, which contains eddies over a wide range of length and time scales. In general, three types of numerical approaches have been developed for dealing with turbulent flows: Direct Numerical Simulation (DNS), Large Eddy Simulation (LES) and Reynolds Averaged Navier-Stokes (RANS) equation method.

The most accurate numerical approach for resolving turbulent flows is DNS, which is capable of resolving all motions in the flow. Coupled turbulent natural convection, conduction and surface radiation in an air-filled three-dimensional (3D) differentially heated cavity was investigated by Xin et al. [4] using the DNS approach. The purpose of their study was to understand a discrepancy regarding interior stratification observed between numerical [5] and experimental [2] results. They concluded that surface radiation was an important factor that affected natural convection in air-filled cavities and thus should not be neglected. Using the DNS method, Soucasse et al. [6] explored surface and gas radiation effects in weakly turbulent regimes of natural convection in a differentially heated 3D cubic cavity. Air with small amounts of water vapour and carbon dioxide was considered with molar fractions fixed at $X_{H2O} = 0.02$ and $X_{CO2} = 0.001$ respectively. The results showed that both the surface and gas radiation significantly intensified turbulent fluctuations, reduced the thermal stratification in the core of the cavity, and enhanced the global circulation.

Another commonly adopted numerical approach for turbulent convection is LES, which resolves large-scale flow structures and models small-scale motions. Capdevila et al. [7] analysed the effect of surface and gas radiation on turbulent natural convection in a 3D differentially heated tall cavity with an aspect ratio of 5 and a Rayleigh number of 4.5×10^{10} based on the height of the cavity by means of LES. The same authors also investigated the effects of a grey participating gas [8] and a semi-grey participating mixture of air and water vapour [9] in the 3D tall cavity model. The LES results were compared with the experimental data available in the literature and the DNS results. It was found that radiation broke the symmetry of the flow, increased the flow intensity and reduced the level of stratification in the cavity. Ibrahim et al. [10] also used LES to study natural convection coupled with surface and gas radiation in a two-dimensional (2D) differentially heated square cavity. They concluded that

the surface radiation increased the turbulence intensity while the gas radiation had little influence on the flow structure.

Whilst DNS is very powerful in resolving turbulent flows, the computational cost associated with DNS is extremely high and thus DNS is not feasible for practical applications. The LES approach requires significantly less computational resources than DNS. However, it is still computationally too expensive for modelling turbulent flows of practical interests. Both the DNS and LES approaches remain to be research tools that can only deal with turbulent flows with relatively low turbulent Reynolds numbers. In contrast, the RANS models, which have been developed by decomposing flow properties into mean and fluctuation components, are the most computationally economical among the three types of numerical approaches. Since for many engineering applications the mean flows are of more interest than the instantaneous fluctuations, the RANS models have been widely adopted to solve engineering problems.

Among the various RANS models, the standard k-ε model has been adopted by many authors. Using this model, Fusegi & Farouk [1] investigated the interactions of turbulent natural convection and radiation in a 2D differentially heated square cavity filled with carbon dioxide gas. Mesyngier & Farouk [11] further studied the same problem with either a single participating gas (H_2O or CO_2) or a homogeneous mixture of two participating gases along with a non-participating gas (N_2). Velusamy et al. [12] analysed the interaction of surface radiation with turbulent natural convection of a transparent medium in 2D square and tall enclosures with differentially heated vertical walls and adiabatic horizontal walls, covering the Rayleigh numbers of 10^9~10^{12} and the aspect ratios of 1~200. Sharma et al. [13] investigated the same problem in a rectangular enclosure heated from below and cooled from the other three walls with the Rayleigh number varying from 10^8 to 10^{12} and the aspect ratio changing from 0.5 to 2.0. The same problem in an inclined differentially heated square cavity with the inclination angle varying from 0 to 90$^\text{o}$ was also studied by Sharma et al. [14]. Serrano-Arellano and Gijón-Rivera [15] reported conjugated heat (by turbulent natural convection–thermal radiation) and mass transfer in a 2D differentially heated square cavity filled with a mixture of Air–CO_2. The hot wall was kept at a constant temperature of 75$^\text{o}$C with a CO_2 concentration of 3000 ppm, whereas the cold wall is considered to be an isothermal wall at 25$^\text{o}$C with a CO_2 concentration of 500 ppm. They found that the radiative heat transfer depressed the heat transfer by natural convection but enhanced the total heat transfer inside the cavity.

The renormalization group (RNG) k-ε model was adopted by Shati et al. [3] to study the effect of turbulent natural convection with and without the interaction of surface radiation in

2D square and rectangular enclosures. The aspect ratio of the enclosure was varied from 0.0625 to 16 and the cold wall temperature was varied from 283 to 373 K, with the hot to cold temperature ratios changing from 1.02 to 2.61. Four different fluids (Argon, Air, Helium and Hydrogen) with properties varying with temperature were considered in their work.

Using a low Reynolds number k-ε model, Xamán et al. [16] analysed the effect of surface radiation on turbulent natural convection in a 2D differentially heated tall cavity. The Rayleigh number, the aspect ratio and the emissivity were considered over the ranges of 10^9~10^{12}, 20~80 and 0~1, respectively. Six low Reynolds number k-ε turbulent models were tested by Iyi et al. [17] for a 2D air-filled differentially heated square cavity. Three different thermal boundary conditions, namely adiabatic, linear temperature profile and experimental temperature profile, are prescribed on the horizontal surfaces. Iyi et al. [18] used the same method to study coupled low turbulence convection and radiation with humid air inside a rectangular cavity partially filled with solid cylindrical objects. The effect of 2D simplification of an inherently 3D radiation problem was also examined by the same authors [19]. They found that the predicted temperatures at the mid-width of the cavity for surface emissivities of $\varepsilon^* = 0.9$ (3D) and $\varepsilon^* = 0.58$ (2D) had a good agreement. Piña-Ortiz et al. [20] also used a low Reynolds number k-ε model to conduct a numerical study of combined turbulent natural convection and surface thermal radiation in a 3D tall cavity (with an aspect ratio of 20) with two emissivity values for the walls (0.3 and 0.95 respectively). Their simulation results of the average Nusselt numbers and heat transfer coefficient are in a good agreement with experimental data.

It is seen from the above reviewed literature that conjugate natural convection with radiation in a 3D cavity of different aspect ratios has been studied using both the DNS and LES approaches, whereas the RANS models have been adopted mostly for 2D cavities. The only 3D investigation with a RANS model considered a cavity of a very high aspect ratio of 20 [20]. To the best knowledge of the authors, conjugate natural convection with radiation in 3D cavities of low aspect ratios (*e.g.,* ~1) has not been studied using the RANS models. Further, when radiation transfer is unaccounted for, discrepancies have been reported between the 2D and 3D cavity models (see for example [5, 21, 22]) and between the models with different thermal boundary conditions specified on the horizontal surfaces (e.g. [5, 17, 23]). However, when radiation transfer is accounted for, the effects of three-dimensionality and the horizontal boundary conditions have not been reported. Therefore, one of the purposes of the present study is to examine the effects of three-dimensionality, radiation transfer and the horizontal boundary conditions on the numerical solution of the convective

flow in the cavity. In addition, the performance of various RANS turbulence models in resolving the conjugate turbulent natural convection with radiation in a 3D cavity of an aspect ratio of 1 will be evaluated.

2.2 Numerical Model and Tests

2.2.1 Geometry and Boundary Conditions

In the present study, both 2D and 3D cavity models, as shown in Fig. 2.1, are considered. The configuration and dimensions of the cavity models are determined in accordance with the model described in [5]. The cavity is filled with air and its dimensions are fixed at $H = W = 1$m and $D = 0.32$m. The two vertical side-walls are maintained at the temperatures $T_h = 303$K and $T_c = 288$K respectively; the two vertical front and back walls (for the 3D cavity only) are assumed adiabatic, whereas the two horizontal walls are either adiabatic or subject to the experimental temperature distributions reported in [5] (refer to Section 2.3.2 for details). Initially, the fluid temperature in the cavity is T_0, which is equal to $(T_h + T_c)/2 = 295.5$K, and the flow is stationary. The air inside the cavity is considered as an incompressible and Newtonian fluid. The Rayleigh number for the present configuration is 1.5×10^9. Here the Rayleigh number Ra is defined as $Ra = \frac{g\beta\Delta T H^3}{\nu\kappa}$, where g is the acceleration due to gravity, β is the coefficient of thermal expansion, $\Delta T = T_h - T_c$ is the temperature difference between the two vertical side-walls, ν is the kinematic viscosity and κ is the thermal diffusivity.
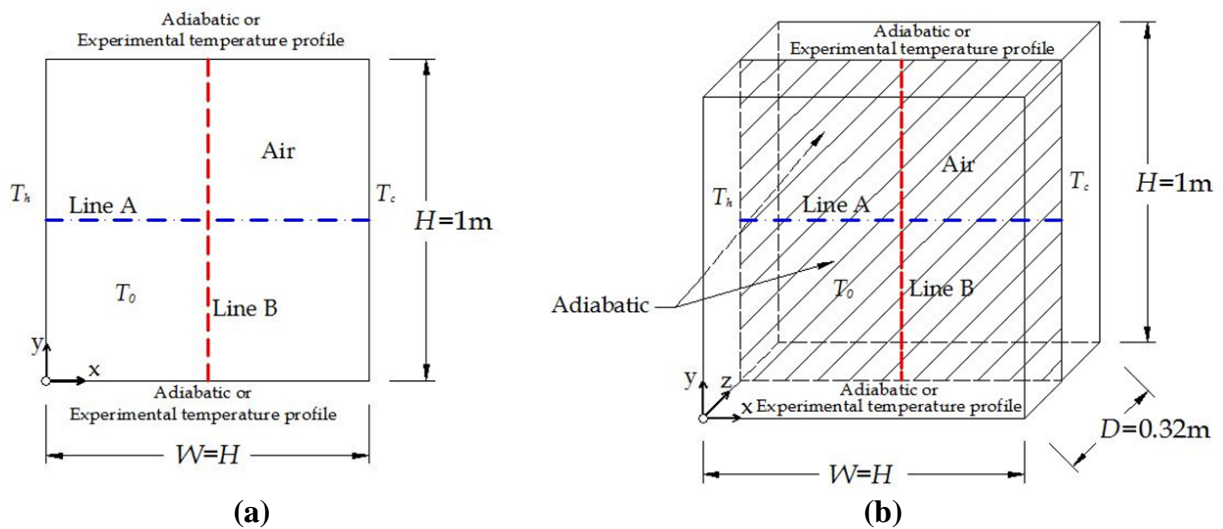
Fig. 2.1 Schematic of the (a) 2D and (b) 3D numerical models. 'Line A' and 'Line B' and the shaded plane in (b), which is at the mid-span (i.e. at $z/H = 0.16$) in the spanwise direction, indicate the locations where temperature and velocity data will be extracted.

36

In this chapter, only surface radiation between the internal surfaces of the cavity is considered. Gas radiation is neglected, which means the working fluid air is a non-participating medium. The inner surfaces of the cavity are assumed to be grey, diffuse and opaque. The emissivities of the vertical side-walls, the horizontal walls and the vertical front and back walls are 0.09, 0.18 and 0.97, respectively according to [4].

2.2.2 Governing Equations

The buoyancy-induced turbulent air flow within the cavity is governed by the following unsteady Reynolds Averaged Navier-Stokes and energy equations with Boussinesq assumption:

$$\frac{\partial u_i}{\partial x_i} = 0 \tag{2.1}$$

$$\frac{\partial u_i}{\partial t} + \frac{\partial (u_i u_j)}{\partial x_j} = -\frac{1}{\rho}\frac{\partial P}{\partial x_i} + \frac{1}{\rho}\frac{\partial}{\partial x_j}\left[\mu\left(\frac{\partial u_i}{\partial x_j} + \frac{\partial u_j}{\partial x_i}\right) - \rho\overline{u_i' u_j'}\right] - g_i\beta(T - T_0) \tag{2.2}$$

$$\frac{\partial T}{\partial t} + \frac{\partial (u_j T)}{\partial x_j} = \frac{1}{\rho}\frac{\partial}{\partial x_j}\left[\frac{\lambda}{C_p}\frac{\partial T}{\partial x_j} - \rho\overline{u_i' T'}\right] \tag{2.3}$$

where x_i and x_j are the Cartesian coordinates in the i and j directions (i, j = 1, 2 and 3 corresponding to the x, y and z directions respectively), t is the time, P is the pressure, T is the mean temperature, T' is the fluctuating temperature, u_i and u_j are the mean velocity components in the i and j directions, u'_i and u'_j are the corresponding fluctuating velocity components in the i and j directions, ρ is the fluid density, λ is the thermal conductivity, C_p is the specific heat capacity, and μ is the dynamic viscosity.

2.2.3 Turbulence Models

In order to close Equations (2.1)-(2.3), the Reynolds stresses ($-\rho\overline{u_i' u_j'}$) and the turbulence heat fluxes ($\overline{u_i' T'}$) must be modelled. Different turbulence models have different treatments of the Reynolds stresses and the turbulence heat fluxes. In this study, five two-equation eddy viscosity turbulence models including the standard k-ε model, the RNG k-ε model, the realisable k-ε model, the standard k-ω model and the shear-stress transport (SST) k-ω model are considered. In these turbulence models, the Reynolds stresses are modelled through the Boussinesq approximation as:

$$-\rho\overline{u_i' u_j'} = \mu_t\left(\frac{\partial u_i}{\partial x_j} + \frac{\partial u_j}{\partial x_i}\right) - \frac{2}{3}\rho k\delta_{ij} \tag{2.4}$$

where μ_t is the turbulent eddy viscosity, k is the turbulent kinetic energy, δ_{ij} is the Kronecker delta ($\delta_{ij} = 0$ if $i{\neq}j$ and $\delta_{ij} = 1$ if $i{=}j$). For the three k-ε models adopted in this study, the turbulent eddy viscosity is obtained by:

$$\mu_t = C_\mu \frac{\rho k^2}{\varepsilon} \tag{2.5}$$

where $C_\mu = 0.09$ in the standard k-ε model [24], $C_\mu = 0.0845$ in the RNG k-ε model [25], and C_μ is computed from an additional equation in the realisable k-ε model [26]; ε is the dissipation rate of the turbulent kinetic energy.

For the standard k-ω model, the turbulent eddy viscosity is computed from:

$$\mu_t = \alpha^* \frac{\rho k}{\omega} \tag{2.6}$$

where ω is the specific dissipation rate, and α^* is a coefficient used to predict transition from laminar to turbulent flow ($\alpha^* = 1$ in fully turbulent flows) [27].

For the SST k-ω model, the turbulent eddy viscosity is computed from:

$$\mu_t = \frac{\rho k}{\omega} \frac{1}{\max\left[\frac{1}{\alpha^*}, \frac{SF_2}{\alpha_1 \omega}\right]} \tag{2.7}$$

where $\alpha_1 = 0.31$, F_2 is a coefficient computed from an additional equation, and S is the modulus of the mean rate-of-strain tensor which is defined as:

$$S = \sqrt{2 S_{ij} S_{ij}} \tag{2.8}$$

where S_{ij} is the mean rate of strain tensor and is given by:

$$S_{ij} = \frac{1}{2}\left(\frac{\partial u_i}{\partial x_j} + \frac{\partial u_j}{\partial x_i}\right) \tag{2.9}$$

More details about the SST k-ω model can be found in [28].

The turbulence heat fluxes are modelled as:

$$\overline{u_i' T'} = -\frac{\mu_t}{\rho \sigma_T} \frac{\partial T}{\partial x_i} \tag{2.10}$$

where σ_T is the turbulent Prandtl number. Here, $\sigma_T = 0.85$ for the selected RANS models except for the RNG k-ε model. In the RNG k-ε model, σ_T is calculated using a formula given in [25].

In the above k-ε and the k-ω models, two additional transport equations (one for the turbulence kinetic energy (k), and the other for either the turbulence dissipation rate (ε) or the specific dissipation rate (ω)) are solved. Further details of these turbulence models can be found in ANSYS FLUENT User's Guide [29].

2.2.4 Radiation Model

Five different radiation models are available in ANSYS FLUENT 14.0 including Discrete Transfer Radiation Model (DTRM), P-1 Radiation Model, Rosseland Radiation Model, Surface to Surface (S2S) Radiation Model and Discrete Ordinates (DO) Radiation Model. Each radiation model has its advantages and limitations. The DO radiation model is the only model that can deal with radiation problems with both participating and non-participating media and problems with semitransparent walls. Moreover, the DO radiation model can also deal with radiative heat transfer problems involving both grey and non-grey surfaces. Therefore, the DO radiation model is adopted in this study due to its superiority over the other radiation models.

In the DO radiation model, the directional variation of the radiative intensity is represented by a discrete number of ordinates, and integrals over solid angles are approximated by numerical quadrature [30]. The radiative transfer equation is solved for a finite number of discrete solid angles for as many transport equations as there are in an associated vector direction at spatial location (*x, y, z*). The equation used in the DO model is written as:

$$\nabla \cdot (I(\vec{r}, \vec{s})\vec{s}) + (a + \sigma_s)I(\vec{r}, \vec{s}) = an^2 \frac{\sigma T^4}{\pi} + \frac{\sigma_s}{4\pi} \int_0^{4\pi} I(\vec{r}, \vec{s}')\Phi(\vec{s} \cdot \vec{s}') \, d\Omega' \qquad (2.11)$$

where $\vec{r}$ is the position vector, $\vec{s}$ is the direction vector, $\vec{s}'$ is the scattering direction vector, a is the absorption coefficient, n is the refractive index, σ_s is the scattering coefficient, σ is the Stefan-Boltzmann constant (5.669×10^{-8} W/m^2-K^4), I is the radiation intensity, which depends on the position ($\vec{r}$) and direction ($\vec{s}$), T is the local temperature, Φ is the phase function, and Ω' is the solid angle.

2.2.5 Numerical Scheme

The governing equations including the two additional transport equations for the turbulence kinetic energy (k) and the turbulence dissipation rate (ε) or the specific dissipation rate (ω) along with the specified boundary and initial conditions are solved using the CFD package ANSYS FLUENT 14.0 which is a finite-volume based solver. The pressure-velocity coupling is carried out using the SIMPLE scheme. The advection terms in the governing equations are discretised by a second-order upwind scheme and the diffusion terms are discretised using a second-order central-differencing scheme. A second-order implicit time-marching scheme is adopted for the unsteady term.

2.2.6 Grid and Time-Step Dependency Tests

Mesh and time-step dependency tests have been conducted for both the 2D and 3D models to ensure the accuracy of the numerical solutions. For this purpose, the flow is initially calculated for 3000s of the flow time, over which period a quasi-steady flow is established in the cavity. The calculation is then extended for another 1000s in order to obtain time-averaged data for the quasi-steady flow. Firstly, four different non-uniform meshes 100×100, 150×150, 200×200 and 300×300 with a fixed time-step 0.01s are calculated for a 2D cavity with adiabatic horizontal walls without the effect of radiation. Fig. 2.2a and 2.2b shows the typical temperature and flow structures in the cavity at the quasi-steady stage obtained with the finest mesh. Here the vertical and horizontal coordinates are normalised by the height of the cavity, the temperature is normalised as $\frac{T-T_0}{T_h-T_c}$, and the stream functions are plotted over the range of 0 to 3.2×10^{-3} kg/s with an even interval of 2.0×10^{-4} kg/s. The stratification of the interior is evident from the isotherms shown in Fig. 2.2a. It is seen in Fig. 2.2b that the primary flow in the cavity is in the clockwise direction with strong flows near the hot and cold walls. The convective flow in the cavity comprises the primary clockwise circulation and secondary circulations near the downstream ends of the hot and cold walls respectively.

The time-averaged horizontal velocity profile extracted along Line B (refer to Fig. 2.1a) is chosen for comparisons and is shown in Fig. 2.2c for the different meshes. Since the velocity profile is symmetric about the centre of the cavity, only the lower half of the profile is shown in Fig. 2.2c. In this figure, the velocity is normalised by the characteristic velocity of the convective flow, which is defined as $U_0 = \frac{\kappa}{H} Ra^{1/2}$ [2]. It is observed in Fig. 2.2c that there is little variation of the velocity profiles obtained with the four different grids. Further quantitative comparison shows that the maximum variation of the results between the coarsest and the finest meshes is only 3.28% of the maximum time-averaged horizontal velocity obtained with the finest mesh, and a clear convergence of the velocity profiles with the refinement of the mesh is obtained. Based on this test, the 150×150 mesh is adopted for the 2D cavity.

Following the above mesh dependence test, three time steps of 0.01s, 0.02s and 0.05s respectively with the 150×150 mesh are tested for the same 2D model. Fig. 2.2d plots the time-averaged horizontal velocity profiles (extracted along Line B) obtained with the different time-steps. It is observed in Fig. 2.2d that the results obtained with the different time-steps are almost identical. In consideration of the numerical accuracy and the computational time (particularly for the subsequent 3D calculations), the 150×150 mesh and the 0.05s time-step are selected for the 2D model.
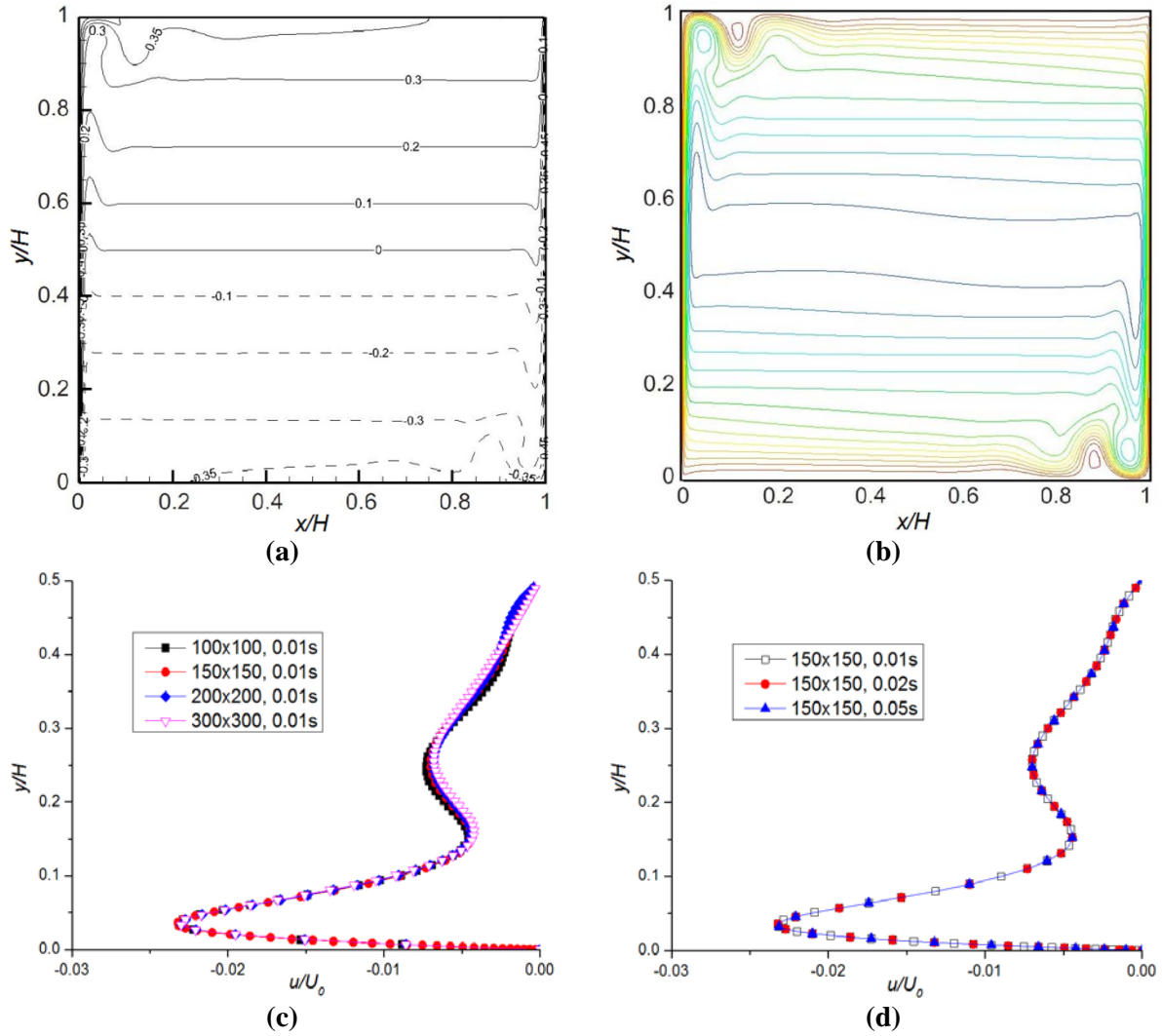
Fig. 2.2 Typical instantaneous (a) temperature (isotherms) and (b) flow structures (contours of stream functions) in the cavity with adiabatic horizontal boundaries at quasi-steady state. Profiles of the time-averaged horizontal velocity along Line B obtained with (c) different meshes and (d) different time-steps.

Further mesh dependence test has been carried out for the 3D cavity model with four non-uniform meshes of $150 \times 150 \times 24$, $150 \times 150 \times 32$, $150 \times 150 \times 48$ and $150 \times 150 \times 96$ respectively. Fig. 2.3 shows the time-averaged vertical velocity profiles in the natural convection boundary layer obtained with the various meshes. All the profiles are taken at the mid-height on the mid-span plane of the cavity, that is, along Line A shown in Fig. 2.1b. It is clear in Fig. 2.3 that the results obtained with the four different grids are almost identical except for the coarsest mesh, which over-predicts the maximum vertical velocity in the natural convection boundary layer compared to the results obtained with the other grids. Further quantitative comparison confirms that all the meshes give very consistent predictions of the time-averaged vertical

velocity profiles with less than 1% variations among them except for the coarsest mesh. Based on the present test, the $150 \times 150 \times 48$ mesh is adopted for the following 3D calculations.
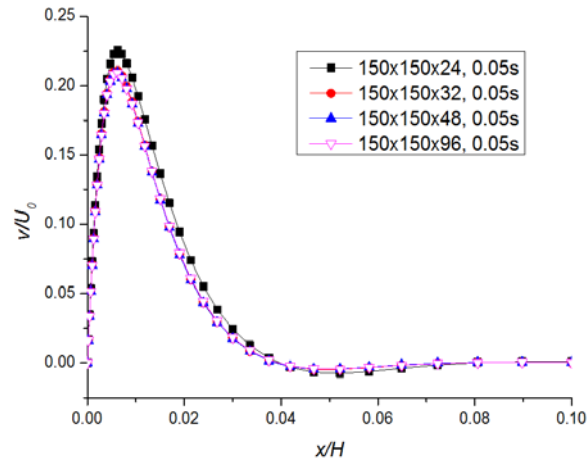
Fig. 2.3 Time-averaged vertical velocity profiles along Line A obtained with different 3D grids.

2.3 Results and Discussions

2.3.1 Comparisons between 2D and 3D Models

The effect of three-dimensionality on the convective flow in a cavity without radiation transfer was previously studied by Soria et al. [21] and Trias et al. [22]. However, the problem with radiation transfer has not been reported in the literature, and thus will be evaluated in this section. Numerical calculations have been carried out in both 2D and 3D cavities with adiabatic horizontal boundaries and with radiation transfer. The simulation results are compared against the experimental data reported in [2]. The experiment was conducted in an air-filled differentially heated cavity, with the left and right polished aluminium walls maintained at 303K and 288K respectively [2]. The horizontal walls were made of polyurethane and aluminium foil in order to have adiabatic conditions with minimal radiative absorption. K-type thermocouples and Laser Doppler Anemometer were used to measure the temperature and velocity at various positions inside the cavity. The RANS model selected for this comparison is the SST k-ω model. Similar comparisons are also made using the other four RANS models, and the results with respect to the three-dimensionality effect with radiation transfer are consistent with that presented below.

Fig. 2.4a and 2.4b shows the typical quasi-steady state temperature and flow structures in the 2D cavity with adiabatic horizontal boundaries and with radiation transfer obtained using the

SST k-ω model. Similar to the temperature structure shown in Fig. 2.2a, the stratification of the interior is evident from the isotherms shown in Fig. 2.4a. However, when radiation transfer is accounted for in the 2D cavity model, the thermal stratification becomes weaker compared to that without radiation transfer (refer to Fig. 2.2a). Further, the contours of stream functions (shown in Fig. 2.4b over the range of 0 to 3.6×10^{-3} kg/s with an even interval of 2.0×10^{-4} kg/s) exhibit distinctly different features from that shown in Fig. 2.2b. It is seen in Fig. 2.4b that the primary flow still comprises a clockwise circulation. However, there are multiple secondary circulations across the cavity. In particular, secondary convective cells are observed near the hot and cold walls, above the bottom boundary and underneath the top boundary. The quasi-steady state temperature and flow structures obtained in the 3D cavity with adiabatic horizontal surfaces and with radiation transfer are generally similar to those obtained in the 2D cavity, as shown in Fig. 2.4a and 2.4b.

(a) **(b)**
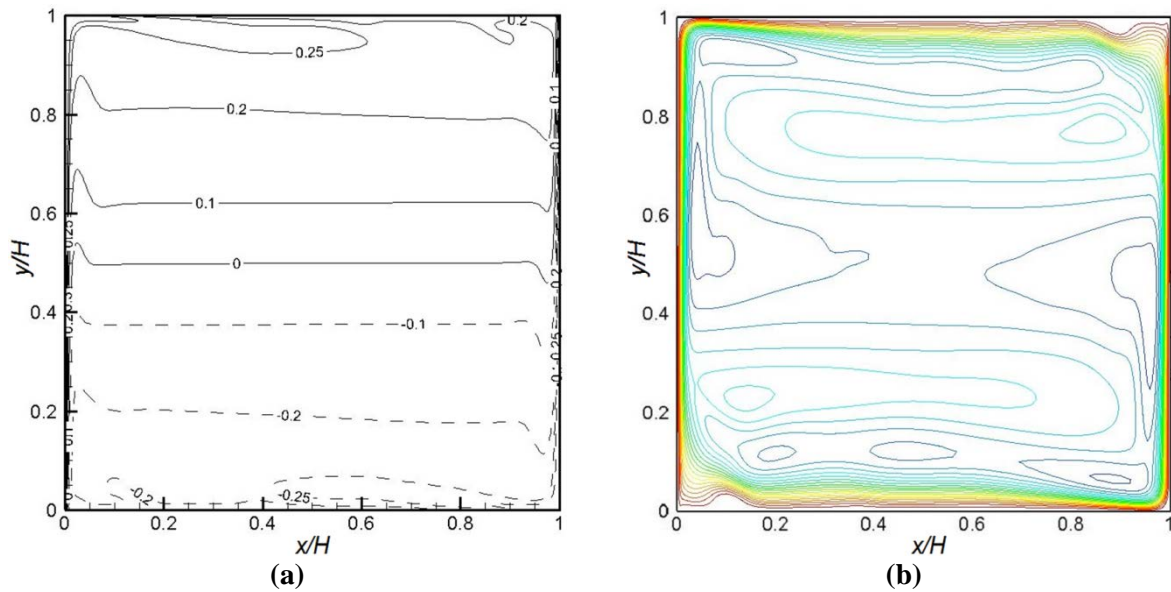
Fig. 2.4 Typical instantaneous (a) temperature (isotherms) and (b) flow structures (contours of stream functions) in the 2D cavity at the quasi-steady state obtained with the adiabatic horizontal boundaries with radiation transfer.

Fig. 2.5a and 2.5b shows the profiles of the time-averaged temperature and vertical velocity along Line A (refer to Fig. 2.1a and 2.1b) obtained in 2D and 3D cavities with the SST k-ω model. Following Lin et al. [31], a three-layer structure of the natural convection boundary layer can be identified in Fig. 2.5a and 2.5b. Here, Δ_{vi}, Δ_T and Δ_v represent the thicknesses of the viscous boundary layer, the thermal boundary layer and the velocity boundary layer, respectively [31]. The dividing positions between the different layers are indicative only. It is seen in Fig. 2.5a and 2.5b that, when compared with the experimental data, a slightly better

prediction of the temperature profile is achieved when the simulation is extended from 2D to 3D (refer to Fig. 2.5a), whereas the variation between the velocity profiles obtained with the 2D and 3D cavity models is insignificant (refer to Fig. 2.5b). These observations indicate that in general, the effect of three-dimensionality on the predicted temperature and velocity profiles at the mid-height of the cavity (i.e. along Line A) is small. They also demonstrate that the SST k-ω model can correctly resolve the temperature and velocity profiles in the natural convection boundary layer, especially when the SST k-ω model is applied to the 3D cavity.

Fig. 2.5 Time-averaged (a) temperature and (b) vertical velocity profiles extracted along Line A and time-averaged (c) temperature and (d) horizontal velocity profiles extracted along Line B obtained in the 2D and 3D cavities with radiation transfer.

The time-averaged temperature and horizontal velocity profiles along Line B (refer to Fig. 2.1a and 2.1b) obtained with the SST k-ω model in 2D and 3D cavities are compared with the experimentally measured profiles in Fig. 2.5c and 2.5d respectively. It is clear in these plots that the 2D cavity model cannot resolve either the temperature or the velocity profile accurately. Fig.

2.5c shows that significant improvement of the predicted thermal stratification is achieved when the simulation is extended from 2D to 3D, resulting in an excellent agreement between the present 3D model and the experimental measurement. Quantitative comparisons of the 2D and 3D predictions of the thermal stratification in the cavity against the experimental measurement [2] are given in Table 2.1. In this table, T_{max} and T_{min} are the normalised maximum and minimum temperatures along Line B respectively.

Table 2.1 Comparisons of the predicted thermal stratification along Line B by the 2D and 3D models with adiabatic horizontal boundaries and with radiation transfer using the SST k-ω model.

Models	$T_{max} - T_{min}$	Error relative to the experimental data (%)
Experiment [2]	0.404	0
2D model	0.508	25.74
3D model	0.402	-0.50

It is also clear in Fig. 2.5d that the improvement of the predicted velocity profiles from the 2D to 3D simulations is limited. The 2D model under-predicts the maximum horizontal velocity, whereas the 3D model over-predicts it. Both 2D and 3D models under-predict the velocity of the secondary flow above the bottom, but the 3D model gives an evidently better prediction than the 2D model.
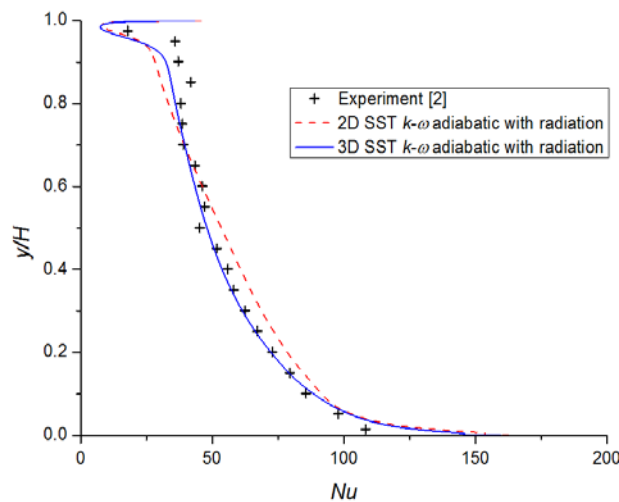
Fig. 2.6 Time-averaged local Nusselt number calculated along the hot wall calculated in the 2D and 3D cavities with radiation transfer.

Fig. 2.6 displays the profiles of the time-averaged local convective Nusselt number calculated along the hot wall in the 2D and 3D cavities (on the mid-span plane in the 3D model). It is seen in this figure that both the 2D and 3D models give consistent predictions of the local Nusselt number along the hot wall, especially near the leading edge and toward the upper end of the hot wall. In general, the numerically obtained profiles of the local Nusselt number are in good agreement with the experimentally measured profile. However, it is also clear in Fig. 2.6 that the 3D model gives an overall better prediction than the 2D model, especially in the region away from the two ends of the hot wall.

Table 2.2 Average Nusselt number calculated on the hot wall in the 2D and 3D cavities with adiabatic horizontal boundaries and with radiation transfer using the SST k-ω model.

Models	$\overline{Nu}_{1D}^{C}$	$\overline{Nu}_{2D}^{C}$	Error relative to the experimental data (%)
Experiment [2]	54	-	0
2D model	56.18	-	4.04
3D model	-	54.36	0.67

Table 2.2 lists the values of the average (in time and space) Nusselt numbers calculated along the hot wall of the 2D and 3D cavities with adiabatic horizontal surfaces and with radiation transfer using the SST k-ω model. Here, the average Nusselt number $\overline{Nu}_{1D}^{C}$ in the 2D cavity is calculated as:

$$\overline{Nu}_{1D}^{C} = \frac{1}{t_2-t_1} \int_{t_1}^{t_2} \int_0^1 \frac{q^C(y,t)}{\lambda \Delta T} dy dt \qquad (2.12)$$

where $q^C(y,t)$ is the instantaneous local convective heat flux evaluated at an arbitrary position y on the hot wall, and t_1 and t_2 are two time instants at the quasi-steady state, over which period the Nusselt number is averaged. The average Nusselt number $\overline{Nu}_{2D}^{C}$ in the 3D cavity is calculated as:

$$\overline{Nu}_{2D}^{C} = \frac{1}{0.32(t_2-t_1)} \int_{t1}^{t_2} \int_0^{0.32} \int_0^1 \frac{q^C(y,z,t)}{\lambda \Delta T} dy dz dt \qquad (2.13)$$

where $q^C(y,z,t)$ is the instantaneous local heat flux due to convection at an arbitrary position of (y, z) on the 2D surface of the hot wall. Note that the normalised depth of the cavity in the spanwise direction is 0.32. The variations of the numerically obtained average Nusselt numbers relative to the experimental measurement are given in Table 2.2. It is seen in this table that the

2D cavity model gives a fairly good prediction of the average Nusselt number. However, significant improvement in the predicted average Nusselt number is observed when the simulation is extended from 2D to 3D, and the 3D result is in an excellent agreement with the experimental data.

2.3.2 Effects of Radiation Transfer and Horizontal Boundary Conditions

The effect of radiation transfer on the convective flow in a differentially heated cavity was previously studied by Velusamy et al. [12]. However, the study was restricted to a 2D cavity. Since it has been demonstrated in Section 2.3.1 above that the 3D model performs better than the 2D model in resolving the temperature and velocity structures in the differentially heated cavity, the effect of radiation transfer is reinvestigated here using the 3D cavity model. In the previous attempt to resolve the discrepancy between the numerical prediction and experimental measurement of interior stratification, two configurations of the differentially heated cavity were examined by Sergent et al. [5]: one with adiabatic horizontal surfaces and the other with experimental temperature profiles (ETP) prescribed on the horizontal surfaces. The experimental temperature profiles, which are given in a normalised form by Equation (2.14) below, are analytical fit of the measured temperature distributions.

$$\begin{cases} \text{Bottom: } T_{bottom}(x,z) = (0.5 - x) + 0.994\frac{x(x-1)(x-0.681)}{x(x-1)-0.0406(x+0.5)} \\ \quad\text{Top: } T_{top}(x,z) = -T_{bottom}(1-x,z) \end{cases} \qquad (2.14)$$

where $T_{top}(x,z)$ and $T_{bottom}(x,z)$ are the normalised temperatures on the top and bottom surfaces respectively, which depend on the position along the surfaces.

Table 2.3 Numerical settings of four 3D test cases for studying the effects of radiation transfer and the thermal boundary conditions on the horizontal surfaces. All the cases are based on the SST k-ω model.

Numerical Cases	Radiation Transfer	Horizontal Boundary Conditions
Case 1	NO	Adiabatic
Case 2	YES	Adiabatic
Case 3	NO	ETP
Case 4	YES	ETP

The above temperature distributions provide a close correlation between the experimental and numerical models and have been found to be effective for resolving the discrepancy with

regard to interior thermal stratification in the differentially heated air-filled cavities. Both of these two configurations are also considered in the present study based on the 3D cavity model with and without radiation transfer. Accordingly, four 3D cases as shown in Table 2.3 are calculated here. All the calculations are carried out using the SST k-ω model.

Fig. 2.7a and 2.7b shows the profiles of the time-averaged temperature along the top and bottom walls obtained with adiabatic horizontal boundaries and with and without radiation transfer (i.e. Cases 1 and 2 in Table 2.3). The experimentally measured temperature profiles [2] and the published DNS data obtained in 3D cavities with and without radiation transfer [4, 5] are also plotted in the same figures for comparison. Significant variations of the temperature profiles between the present results obtained with and without radiation transfer are observed in Fig. 2.7 for both the top and bottom walls. In general, the numerically obtained temperature profiles on the top and bottom walls are in a good agreement with the DNS results, especially in the case without radiation transfer (Case 1). When radiation transfer is accounted for (Case 2), the comparison between the temperature profiles obtained with the SST k-ω model in the present study and those measured experimentally is greatly improved. The small deviation between the present results with radiation transfer and the corresponding DNS data may be attributed to the effect of heat conduction through the top and bottom walls, which was considered in the DNS study [3] but is neglected in the present simulation. The effect of radiation transfer on the thermal stratification in the cavity (calculated along Line B) is shown quantitatively in Table 2.4. It is seen in this table that a significant improvement in the predicted thermal stratification is achieved when the radiative effect is accounted for in the 3D cavity. For the rest of this study, only the results obtained with radiation transfer are presented except for that shown in Fig. 2.9.
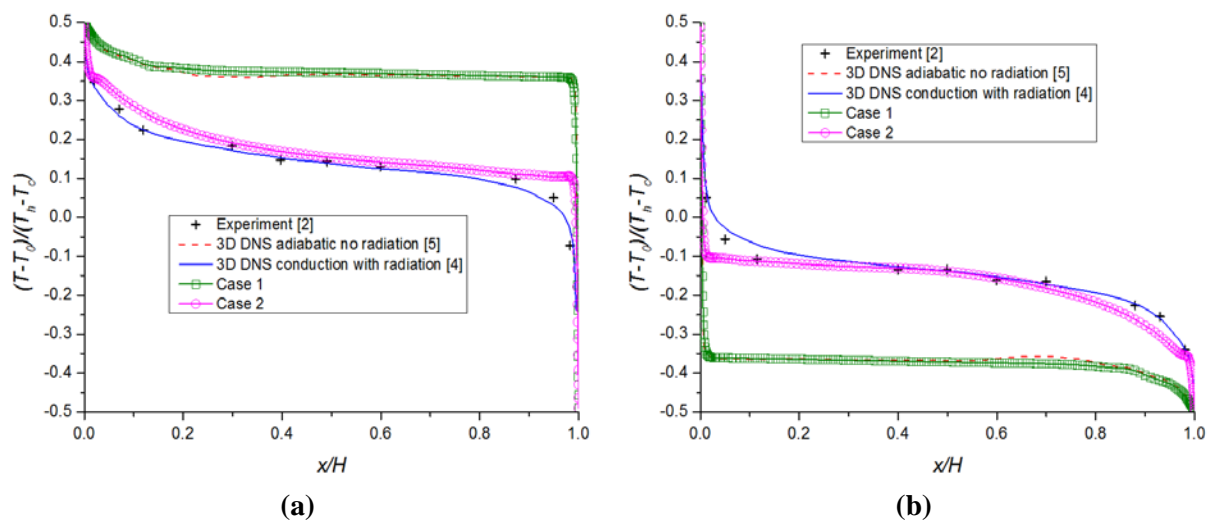
Fig. 2.7 Time-averaged temperature profiles extracted along (a) the top surface and (b) the bottom surface obtained in the 3D cavity with and without radiation transfer. Case 1: adiabatic

horizontal boundaries without radiation transfer obtained with the SST k-ω model; Case 2: adiabatic horizontal boundaries with radiation transfer obtained with the SST k-ω model.

Table 2.4 Comparisons of the predicted thermal stratification along Line B obtained in the 3D cavity with and without radiation transfer using the SST k-ω model.

Models	$T_{max} - T_{min}$	Error relative to the experimental data (%)
Experiment [2]	0.404	0
Case 1	0.744	84.16
Case 2	0.402	-0.50

Fig. 2.8a and 2.8b shows the profiles of the time-averaged temperature and vertical velocity along Line A (refer to Fig. 2.1b) obtained with the two different horizontal boundary conditions and with radiation transfer (i.e. Cases 2 and 4 in Table 2.3). No significant variation between the numerical results obtained with adiabatic horizontal surfaces and those obtained with experimental temperature distributions on the horizontal boundaries is observed in these two plots. Both sets of simulations produce temperature profiles in a good agreement with the experimental data. In terms of the predicted velocity profiles, a slightly better prediction of the maximum vertical velocity in the thermal boundary layer is achieved when the experimental temperature profiles are specified on the horizontal surfaces (Case 4) compared to that obtained with adiabatic horizontal surfaces (Case 2). But overall both sets of the velocity profiles agree well with the experimental data.

Fig. 2.8c and 2.8d plots the profiles of the time-averaged temperature and horizontal velocity along Line B (refer to Fig. 2.1b) obtained with the two different horizontal boundary conditions and with radiation transfer. Again it is clear in Fig. 2.8c and 2.8d that no distinct variation of the predicted temperature and velocity profiles obtained with the two different horizontal boundary conditions is observed. Fig. 2.8c shows that the temperature profiles produced by both sets of simulations are almost identical and are in an excellent agreement with the experimental data. A minor variation between the two sets of the numerically produced velocity profiles can be observed in Fig. 2.8d. Both numerical models over-predict the maximum horizontal velocity of the primary circulation and under-predict the velocity of the secondary flow above the bottom. The discrepancy between the present simulation and the experiment with regard to the horizontal velocity profile along Line B (refer to Fig. 2.8d) may be attributed to the absence of heat conduction through the horizontal walls in the numerical model.

This argument is supported by the recent study of Xin et al. [4], which shows considrable improvement of the predicted near wall distributions of the horizontal velocity by coupling natural convection with conduction through the horizontal walls.
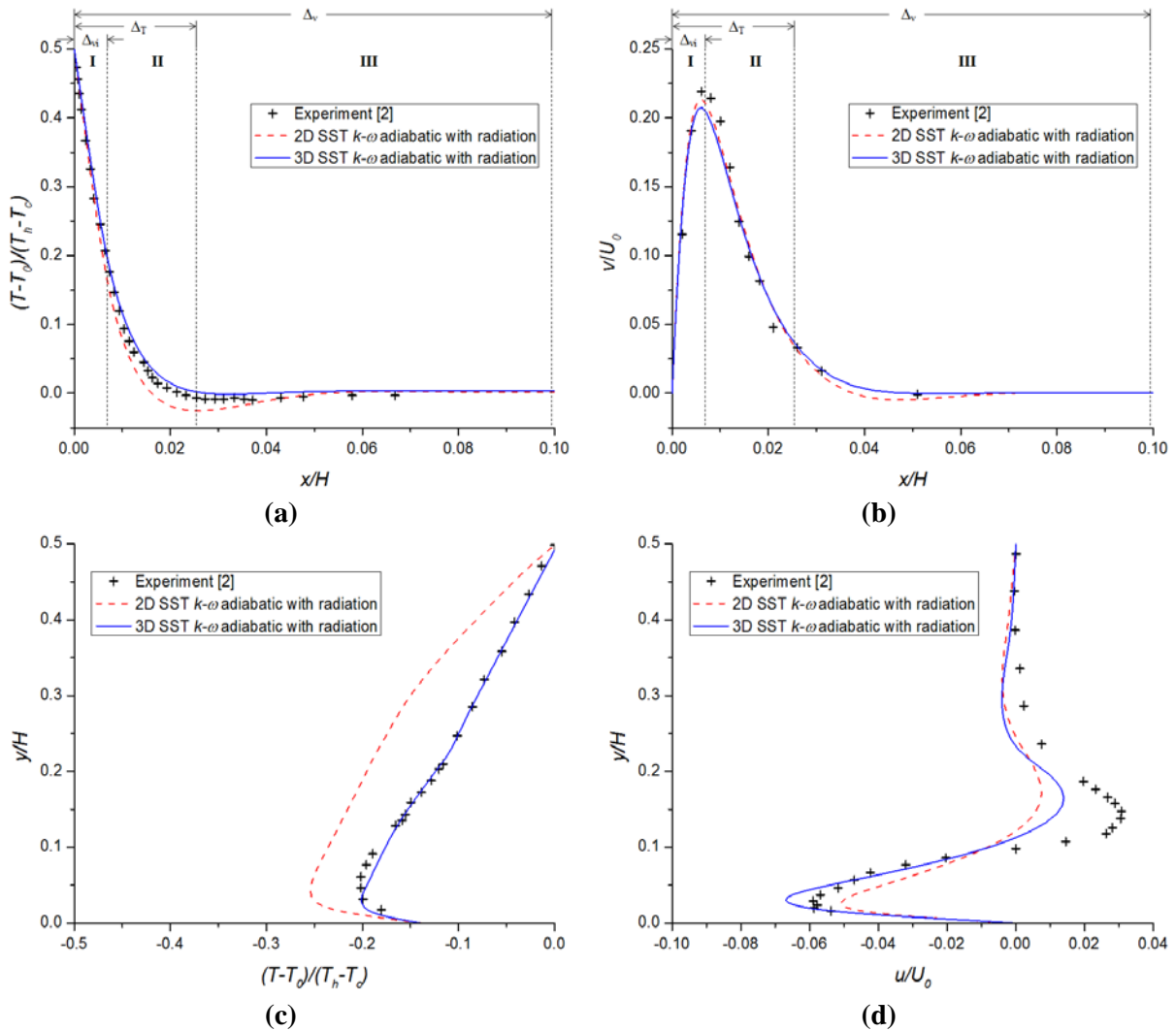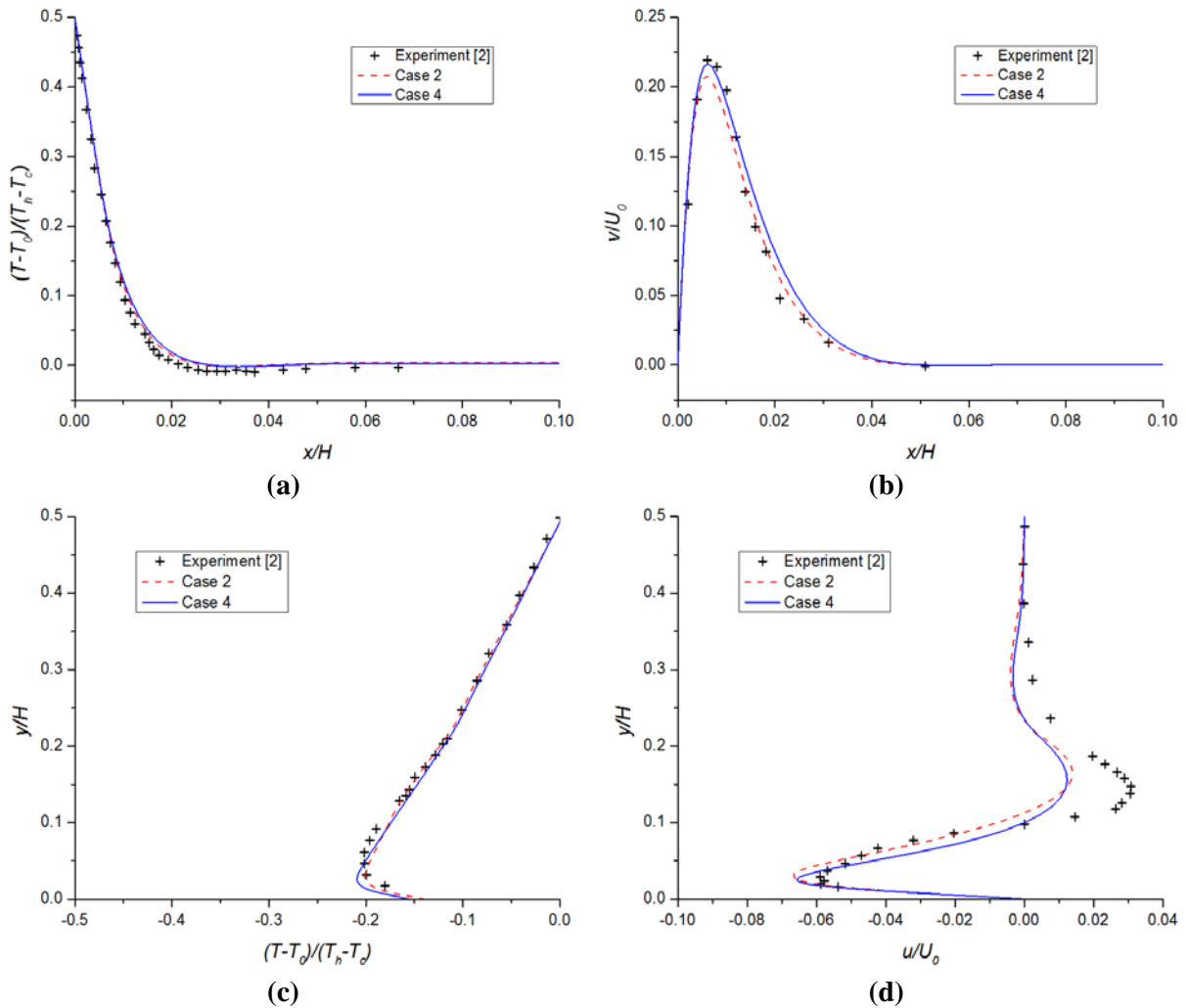

Fig. 2.8 Time-averaged (a) temperature and (b) vertical velocity profiles extracted along Line A and time-averaged (c) temperature and (d) horizontal velocity profiles extracted along Line B obtained in the 3D cavity with different horizontal boundary conditions and with radiation transfer.

Fig. 2.9 illustrates the profiles of the time-averaged local convective Nusselt number obtained along the hot wall of the 3D cavity (on the mid-span plane). It is seen in this figure that, when radiation transfer is accounted for (Cases 2 and 4), the predicted local Nusselt number is lower for the lower part of the hot wall and higher for the upper part of the hot wall than that predicted without radiation transfer (Cases 1 and 3). Overall a significantly better prediction of the local Nusselt number in terms of comparison with the experimental data is achieved when radiation transfer is accounted for. The impact of radiation transfer on the numerical results is

less significant when the experimental temperature profiles are specified on the horizontal surfaces (Cases 3 and 4) compared to its impact when adiabatic horizontal surfaces are assumed (Cases 1 and 2). The results in Fig. 2.9 also show that the different horizontal boundary conditions have a significant impact on the predicted local Nusselt number when radiation transfer is neglected (Cases 1 and 3), but the effect of the horizontal boundary conditions is insignificant (and negligibly small in the core region of the cavity) when radiation transfer is included (Cases 2 and 4).
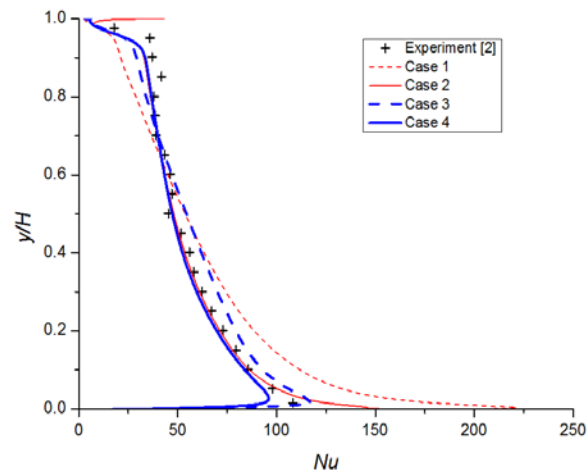
Fig. 2.9 Time-averaged local Nusselt number calculated along the hot wall in the 3D cavity with different horizontal boundary conditions and with and without radiation transfer.

2.3.3 Comparisons of Different RANS Models

The results presented above are all based on the SST k-ω model. It has been demonstrated that the numerical results obtained with the SST k-ω model are in a good agreement with the experimental data if radiation transfer is accounted for in the 3D cavity model. In this section, the performance of the other four popular RANS models, including the standard k-ε model, the RNG k-ε model, the realisable k-ε model and the standard k-ω model, are evaluated based on the 3D cavity model. Since it has been demonstrated in Section 2.3.2 that better predictions of the temperature and flow structures and the heat transfer rate are achieved when radiation transfer is accounted for, the evaluation of the turbulence models below will be based on the 3D model with radiation transfer only. It has also been demonstrated above that, when radiation transfer is included in the model, the numerical results obtained with adiabatic horizontal surfaces and those obtained with the experimental temperature profiles prescribed on the horizontal surfaces are very similar. Therefore, only the numerical results obtained with the experimental temperature profiles specified on the horizontal surfaces are presented below. The

simulation results are evaluated against the experimental measurement of Salat et al. [2] and the 3D DNS results of Xin et al. [4], in which radiation transfer is also accounted for.

Fig. 2.10a and 2.10b shows the profiles of the time-averaged temperature and vertical velocity along Line A (refer to Fig. 2.1b) obtained with the different RANS models along with the above-mentioned experimental and DNS data. It is seen in Fig. 2.10a that the temperature profiles obtained with all the RANS models and the DNS almost overlap with each other, which are also in an excellent agreement with the experimental data. For the velocity profile prediction (refer to Fig. 2.10b), the SST k-ω model precisely captures the maximum vertical velocity in the thermal boundary layer, whereas all the other RANS models under-estimate the maximum velocity. The SST k-ω model also gives an overall better prediction of the velocity profile across all regions of the boundary layer than the other RANS models.
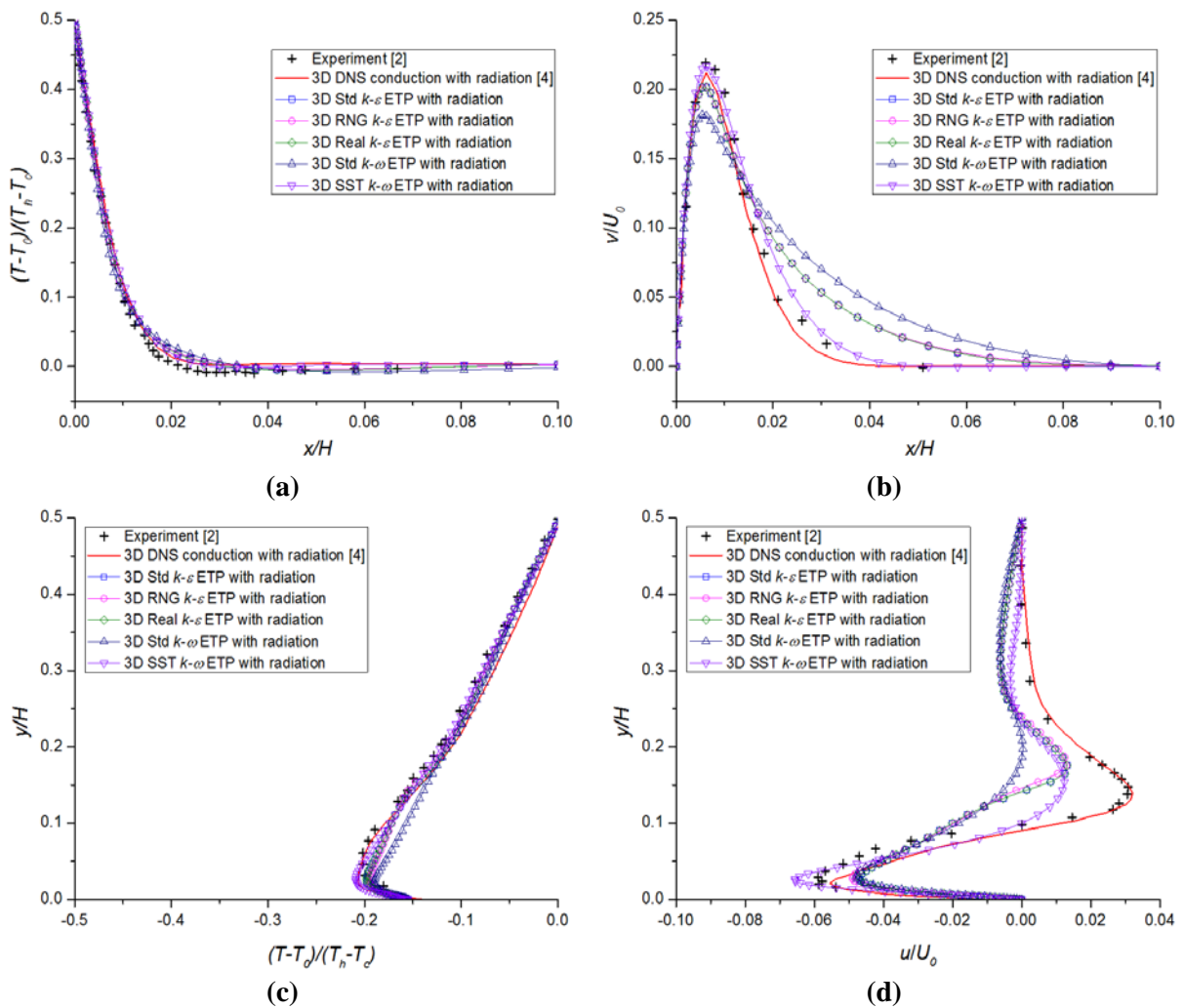
Fig. 2.10 Time-averaged (a) temperature and (b) vertical velocity profiles extracted along Line A and time-averaged (c) temperature and (d) horizontal velocity profiles extracted along Line B obtained in the 3D cavity with radiation transfer.

52

The time-averaged temperature and horizontal velocity profiles along Line B (refer to Fig. 2.1b) obtained with the different RANS models are shown in Fig. 2.10c and 2.10d respectively. It is clear in Fig. 2.10c that all the RANS models precisely predict the thermal stratification in the cavity. Among the five RANS models considered here, the SST k-ω model has the best performance and the standard k-ω model has the worst performance in predicting the temperature structure. For the velocity profile prediction, the SST k-ω model over-estimates the maximum horizontal velocity of the primary flow (in the horizontal layer above the bottom), whereas all the other RANS models under-estimate this velocity. All the RANS models also under-estimate the velocity of the secondary flow above the bottom, but the SST k-ω model has the smallest variation from the DNS result and the experimental measurement. The standard k-ω model fails to predict the secondary circulation above the bottom (since no positive horizontal velocity is observed there) and has the worst overall performance in predicting the velocity profile.

The average (in time and space) Nusselt numbers calculated on the hot wall of the cavity with the different RANS models are gathered in Table 2.5. Here $\overline{Nu}_{1D}^{C}$ is the average Nusselt number calculated along the edge of the hot wall on the mid-span plane (Equation 2.12), corresponding to the experimental measurement, and $\overline{Nu}_{2D}^{C}$ is the average Nusselt number calculated across the entire surface of the hot wall (Equation 2.13). It is found that all the RANS models under-estimate the average Nusselt number calculated on the mid-span plane (i.e. $\overline{Nu}_{1D}^{C}$) compared to the experimentally measured data, and the standard k-ω model gives the best prediction among them. However, the average Nusselt number calculated on the mid-span plane does not necessarily represent the overall heat transfer through the entire hot wall. As such, the average Nusselt numbers calculated across the surface of the hot wall (i.e. $\overline{Nu}_{2D}^{C}$) are also compared against the corresponding DNS data in Table 2.5. It is seen in this table that the standard k-ε model, the realisable k-ε model and the SST k-ω model under-predict $\overline{Nu}_{2D}^{C}$, but the variations relative to the DNS data are much less significant when compared to the variations of the Nusselt numbers calculated on the mid-span plane (i.e. $\overline{Nu}_{1D}^{C}$). The closest prediction of $\overline{Nu}_{2D}^{C}$ to the DNS result is obtained with the RNG k-ε model. The standard k-ω model has the worst performance which over-estimates the average Nusselt number by over 3%.

Table 2.6 lists the values of the average radiative Nusselt number calculated on the 2D surface of the hot wall of the cavity. Here, the average radiative Nusselt number $\overline{Nu}_{2D}^{R}$ is calculated as:

$$\overline{Nu}_{2D}^{R} = \frac{1}{0.32(t_2 - t_1)} \int_{t_1}^{t_2} \int_0^{0.32} \int_0^1 \frac{q^R(y,z,t)}{\lambda \Delta T} dy \, dz \, dt \qquad (2.15)$$

53

where $q^R(y, z, t)$ is the instantaneous local radiative flux at an arbitrary position of (y, z) on the 2D surface of the hot wall. It is clear in Table 2.6 that all the RANS models produce identical results. This is because all the RANS models are coupled with the same radiation model – the Discrete Ordinates Radiation Model. The difference between the results obtained with the RANS models and that of the DNS is relatively small. Therefore, it is confirmed that the DO radiation model is appropriate for the present study.

Table 2.5 Average Nusselt number calculated on the hot wall in the 3D cavity with radiation transfer.

Models	$\overline{Nu}_{1D}^C$	Error relative to the experimental data (%)	$\overline{Nu}_{2D}^C$	Error relative to the DNS data (%)
Experiment [2]	54	0	-	-
DNS [4]	53.43	1.06	54.04	0
Standard k-ε	48.01	11.09	53.53	2.79
RNG k-ε	48.51	10.17	54.23	0.35
Realisable k-ε	48.01	11.09	53.53	0.94
Standard k-ω	50.91	5.72	55.80	3.26
SST k-ω	47.97	11.17	52.91	2.09

Table 2.6 Average radiative Nusselt number calculated on the hot wall in the 3D cavity with radiation transfer.

Models	$\overline{Nu}_{2D}^R$	Error relative to the DNS data (%)
DNS [4]	10.42	0
Standard k-ε	10.11	2.98
RNG k-ε	10.11	2.98
Realisable k-ε	10.11	2.98
Standard k-ω	10.11	2.98
SST k-ω	10.11	2.98

Table 2.7 summarises the detailed results quantifying the performance of the various RANS models in the 3D cavity with radiation transfer. In this table, $\Delta T'$ represents the standard deviation of the variation of the time-averaged temperature profiles between a selected RANS model and the experimental data [2]. $\Delta v'$ and $\Delta u'$ are the standard deviations of the variations of the time-averaged vertical velocity profiles extracted along Line A and horizontal velocity profiles extracted along Line B, respectively, with reference to the experimentally measured

velocity profiles. $|v|_{max}$ and $|u|_{max}$ are the maximum absolute values of the vertical and horizontal velocities respectively obtained in the experiment [2]. It is clear in this table that, in general, all the RANS models perform well compared with the experimental data in terms of the temperature profile along Line A. However, significantly larger discrepancies are found in predicting the vertical velocity profile along Line A using the different RANS models, and the SST k-ω model performs the best among them. It is also seen in Table 2.7 that in general, the performance of the RANS models in predicting the temperature profile along Line B is also consistently good. However, for predicting the horizontal velocity profile along Line B, the performance of the RANS models is much worse than that in predicting the vertical velocity profile along Line A, which is also evident by comparing Fig. 2.10b and 2.10d. The numerical errors of the RANS models with reference to the experimental data are in the order of 20%, except for the SST k-ω model, for which the error is reduced to around 15%. It is worth noting that the relatively larger numerical errors associated with the predicted horizontal velocity profiles along Line B compared to the numerical errors associated with the predicted vertical velocity profile along Line A are in part attributed to the relatively smaller maximum velocity $|u|_{max}$ (compared to $|v|_{max}$) used for the normalisation (refer to Fig. 2.10). The relatively large errors in the predicted horizontal velocity profiles along Line B may also be caused by the absence of heat conduction through the horizontal walls in the numerical model, as discussed in Section 2.3.2 above.

Table 2.7 The performance of the various RANS models in the 3D cavity with radiation transfer.

Compared items		Std k-ε (%)	RNG k-ε (%)	Real k-ε (%)	Std k-ω (%)	SST k-ω (%)
Line A	$\Delta T'/(T_h - T_c)$	0.69	0.83	0.69	1.54	0.42
	$\Delta v'/|v|_{max}$	7.52	7.50	7.52	12.79	3.64
Line B	$\Delta T'/(T_h - T_c)$	0.72	0.86	0.72	1.05	0.49
	$\Delta u'/|u|_{max}$	23.48	23.38	23.48	26.38	15.29

It has been demonstrated above that in the 3D cavity with radiation transfer, the SST k-ω model has the best performance in all aspects except for the prediction of the average Nusselt number on the hot wall. The worst overall performance is found with the standard k-ω model. All the k-ε models produce very similar results, which are between the predictions of the SST k-ω model and the standard k-ω model in terms of performance.

2.4 Conclusions

The purpose of this study is to examine the effects of three-dimensionality, radiation transfer and thermal boundary conditions on the numerical solution of turbulent natural convection in an air-filled differentially heated cavity and evaluate the accuracy of five common two-equation RANS models. Two- and three-dimensional simulations with and without radiation transfer have been described at a Rayleigh number of 1.5×10^9. Two sets of simulations, one with adiabatic top and bottom surfaces and the other with the experimentally measured temperature distributions [5] prescribed on the top and bottom surfaces, are presented. The performance of the numerical models is evaluated against the experimental data [2] and the direct numerical simulations results [4, 5]. In all the numerical models, the working fluid air is assumed to be a non-participating medium and the inner surfaces of the cavity are assumed to be grey, diffuse and opaque. For the 3D models, the front and rear vertical walls are assumed adiabatic. The following conclusions can be drawn from the present investigations:

(1) The present results show that both the 2D and 3D models with radiation transfer can accurately resolve the temperature and velocity structures in the boundary layer. However, the 2D model fails to resolve the interior stratification, whereas the 3D model predicts the interior stratification in an excellent agreement with the experimental data. Therefore, the 3D model is recommended for resolving the conjugate turbulent natural convection and radiation in the differentially heated cavity.

(2) It is found that the variation between the time-averaged quantities obtained with and without the effect of radiation transfer in the 3D cavity is very significant. The predicted temperature profiles on the adiabatic top and bottom surfaces agree very well with the experimental measurement when radiation transfer is accounted for. It is therefore concluded that radiation transfer plays an important role in the convective flow in the 3D cavity.

(3) It is also demonstrated in the present study that the thermal boundary conditions on the horizontal surfaces have a significant effect on the numerical solution when radiation transfer is not accounted for. However, the effect is much less significant when radiation transfer is accounted for.

(4) It has been argued in the previous studies that the discrepancy with respect to the interior stratification between the experiment and numerical simulation is due to the fact that the horizontal walls are not perfectly insulated [2]. However, the present investigation has demonstrated that the predicted thermal stratification with adiabatic top and bottom

boundaries is very close to the experimental measurement when radiation transfer is accounted for. It is further suggested that the discrepancy between the experiment and numerical simulation with regard to the interior stratification is mainly caused by the negligence of radiation transfer in the numerical model. However, the absence of heat conduction through the horizontal walls in the numerical model may have contributed to the relatively large errors in the predicted horizontal velocity profiles along the centreline of the cavity.

(5) All the RANS models are capable of capturing the main features of the flow and the overall performance of these turbulence models in terms of predicting the time-averaged quantities is acceptable, although not all of these models can resolve the flow details accurately. It is found that the variation between the three k-ε models is very small, whereas the discrepancy between the two k-ω models is significant. The SST k-ω model has the best performance in terms of predicting the time-averaged quantities except for the average Nusselt number along the hot wall. The standard k-ω model has the worst overall performance.

References

[1] Fusegi, T., and Farouk, B., 1989. Laminar and turbulent natural convection–radiation interactions in a square enclosure filled with a nongray gas. Numerical Heat Transfer, Part A: Applications: An International Journal of Computation and Methodology. 15, 303-322.

[2] Salat, J., Xin, S., Joubert, P., Sergent, A., Penot, F., and Le Quéré, P., 2004. Experimental and numerical investigation of turbulent natural convection in a large air-filled cavity. International Journal of Heat and Fluid Flow. 25, 824-832.

[3] Shati, A.K.A., Blakey, S.G., and Beck, S.B.M., 2012. A dimensionless solution to radiation and turbulent natural convection in square and rectangular enclosures. Journal of Engineering Science and Technology. 7(2), 257-279.

[4] Xin, S., Salat, J., Joubert, P., Sergent, A., Penot, F., and Le Quéré, P., 2013. Resolving the stratification discrepancy of turbulent natural convection in differentially heated air-filled cavities. Part III: A full convection–conduction–surface radiation coupling. International Journal of Heat and Fluid Flow. 42, 33-48.

[5] Sergent, A., Xin, S., Joubert, P., Le Quéré, P., Salat, J., and Penot, F., 2013. Resolving the stratification discrepancy of turbulent natural convection in differentially heated air-filled cavities – Part I: Reference solutions using Chebyshev spectral methods. International Journal of Heat and Fluid Flow. 39, 1-14.

[6] Soucasse, L., Riviere, P., Soufiani, A., Xin, S., and Le Quéré, P., 2014. Transitional regimes of natural convection in a differentially heated cubical cavity under the effects of wall and molecular gas radiation. Physics of Fluids. 26, 024105-1-23.

[7] Capdevila, R., Lehmkuhl, O., Colomer, G., and Perez-Segarra, C.D., 2012. Study of turbulent natural convection in a tall differentially heated cavity filled with either non-participating, participating grey and participating semigrey media. Journal of Physics: Conference Series. 395, 012155.

[8] Capdevila, R., Lehmkuhl, O., Trias, F.X., Pérez-Segarra, C.D., and Colomer, G., 2011. Turbulent natural convection in a differentially heated cavity of aspect ratio 5 filled with non-participating and participating grey media. Journal of Physics: Conference Series. 318, 042048.

[9] Capdevila, R., Pérez-Segarra, C.D., Lehmkuhl, O., and Colomer, G., 2010. Numerical Simulation of Turbulent Natural Convection and Gas Radiation in Differentially Heated Cavities Using FVM, DOM and LES. 6th International Symposium on Radiative Transfer, Antalya, Turkey.

[10] Ibrahim, A., Saury, D., and Lemonnier, D., 2013. Coupling of turbulent natural convection with radiation in an air-filled differentially-heated cavity at Ra = 1.5 x 10^9. Computers & Fluids. 88, 115-125.

[11] Mesyngier, C., and Farouk, B., 1996. Turbulent natural convection-nongray gas radiation analysis in a square enclosure. Numerical Heat Transfer, Part A: Applications: An International Journal of Computation and Methodology. 29(7), 671-687.

[12] Velusamy, K., Sundararajan, T., and Seetharamu, K.N., 2001. Interaction effects between surface radiation and turbulent natural convection in square and rectangular enclosures. Journal of heat transfer. 123(6), 1062-1070.

[13] Sharma, A.K., Velusamy, K., and Balaji, C., 2008. Interaction of turbulent natural convection and surface thermal radiation in inclined square enclosures. Heat Mass Transfer. 44, 1153–1170.

[14] Sharma, A.K., Velusamy, K., Balaji, C., and Venkateshan, S.P., 2007. Conjugate turbulent natural convection with surface radiation in air filled rectangular enclosures. International Journal of Heat and Mass Transfer. 50, 625–639.

[15] Serrano-Arellano, J., and Gijón-Rivera, M., 2014. Conjugate heat and mass transfer by natural convection in a square cavity filled with a mixture of Air–CO_2. International Journal of Heat and Mass Transfer. 70, 103–113.

[16] Xamán, J.P., Hinojosa, J.F., Flores, J.J., and Cabanillas, R.E., 2008. Effect of the surface thermal radiation on turbulent natural convection in tall cavities of façade elements. Heat Mass Transfer. 45, 177–185.

[17] Iyi, D.A., Hasan, R. & Penlington, R., 2011. Numerical analysis of the influence of thermal boundary condition and surface emissivity on the flow and heat transfer in turbulent buoyancy driven flow. 3rd Asian Symposium of Computational Heat Transfer and Fluid Flow. 22-26 September, Kyoto, Japan, 2011.

[18] Iyi, D., Hasan, R., and Penlington, R., 2012. Interaction effects between surface radiation and double-diffusive turbulent natural convection in an enclosed cavity filled with solid obstacles. International Symposium on Advances in Computational Heat Transfer. Bath, England.

[19] Iyi, D., Hasan, R., and Penlington, R., 2013. Numerical Simulation of 2D Turbulent Natural Convection of Humid Air in a Cavity Filled with Solid Objects. Procedia Engineering. 56, 538-543.

[20] Piña-Ortiz, A., Hinojosa-Palafox, J.F., and Pérez-Valenzuela, J.B., 2013. Numerical and experimental study of heat transfer in a tall vertical closed cavity. Heat and Mass Transfer. 49(7), 933-945.

[21] Soria, M., Trias, F.X., Pérez-Segarra, C.D., and Oliva, A., 2004. Direct numerical simulation of a three-dimensional natural-convection flow in a differentially heated cavity of aspect ratio 4. Numerical Heat Transfer, Part A: Applications: An International Journal of Computation and Methodology. 45(7), 649-673.

[22] Trias, F.X., Soria, M., Oliva, A., and Perez-Segarra, C.D., 2007. Direct numerical simulation of two- and three-dimensional natural convection flows in a differentially heated cavity of aspect ratio 4. Journal of Fluid Mechanics. 586, 259–293.

[23] Peng, S., and Davidson, L., 2001. Large eddy simulation for turbulent buoyant flow in a contained cavity. International Journal of Heat and Fluid Flow. 22, 323–331.

[24] Launder, B.E., and Spalding, D.B., 1972. Lectures in Mathematical Models of Turbulence. Academic Press, London.

[25] Orszag, S.A., Yakhot, V., Flannery, W.S., Boysan, F., Choudhury, D., Maruzewski, J., and Patel, B., 1993. Renormalization Group Modeling and Turbulence Simulations. International Conference on Near-Wall Turbulent Flows. Tempe, Arizona.

[26] Shih, T.H., Liou, W.W., Shabbir, A., Yang, Z., and Zhu, J., 1995. A New k-ε Eddy-Viscosity Model for High Reynolds Number Turbulent Flows - Model Development and Validation. Computers & Fluids. 24(3), 227–238.

[27] Wilcox, D.C., 1998. Turbulence Modeling for CFD. DCW Industries, Inc. La Canada, California.

[28] Menter, F.R., 1994. Two-Equation Eddy-Viscosity Turbulence Models for Engineering Applications. AIAA Journal. 32, 1598-1605.

[29] Fluent Inc., 2011. ANSYS FLUENT User's Guide. USA.

[30] Modest, M.F., 2013. Radiative Heat Transfer, 3rd edn. Academic Press, New York.

[31] Lin, W., Armfield, S.W., Patterson, J.C., and Lei, C., 2009. Prandtl number scaling of unsteady natural convection boundary layers for Pr>1 fluids under isothermal heating. Physical Review E. 79(6), 066313.

3. Thermal Modelling and Experimental Validation of a Semi-Transparent Water Wall System

Statement of contribution to co-authored manuscript

This chapter is based on a co-authored manuscript. The details of the manuscript, including all authors, are:

Wu, T. & Lei, C. Thermal modelling and experimental validation of a semi-transparent water wall system. To be submitted.

My contribution to the paper included reviewing the relevant literature, formulating the transient heat balance model, developing a finite difference method for solving the THBM, collecting and analysing the simulated and filed data, and drafting the paper.

Signed: _____ Date: 09.03.2016

Ting Wu

Countersigned: _____ Date: 10/03/2016

Co-author: A/Prof. Chengwang Lei (Supervisor, School of Civil Engineering, The University of Sydney)

3.1 Introduction

Energy consumption by residential and commercial buildings accounts for nearly one quarter of the total worldwide consumption of delivered energy (Energy Information Administration, 2013), and it is predicted that the building energy consumption will increase by approximately 1.6% per year from 2010 to 2040. Therefore, saving energy in buildings is critical for the combat against global energy crisis and climate change. For this purpose, a number of passive solar technologies have been developed for buildings and have attracted a growing research interest.

Among the various passive solar strategies, water wall is an excellent solution which can maintain thermal comfort in buildings while reducing energy consumption. The water wall system has unique advantages over other passive strategies as it allows part of the solar radiation to enter the buildings, and thus reduce the need for lighting during the daytime. The semi-transparent nature of the water wall system also gives the system aesthetic advantages over opaque walls. In addition, the cost of the water wall system is significantly lower than that of thermal storage walls using phase change materials (PCMs). Further, the heat stored in water may be redistributed by convection, and thus a water wall provides quicker heat exchange than a concrete or brick wall.

A large body of literature exists on analytical investigations of the thermal performance of water walls. Sodha et al. (1981) compared the thermal performance of a Trombe wall with a water wall plus concrete, a water wall plus insulation panels and a simple water column by calculating the heat transfer through these walls in an air-conditioned room using a heat balance model (HBM). The HBM is based on the energy conservation concept to establish energy balance associated with conductive, convective and radiative heat transfer in order to obtain surface and fluid (i.e. water and air) temperatures. Their results illustrated that a water wall plus concrete system was more desirable than the other configurations for the winter climate in New Delhi, and the more water contained in the water wall plus concrete system, the better performance was achieved. Sodha et al. (1992) also compared the effects of two types of thermal storage materials (i.e. water and concrete) on the thermal performance of a non-air-conditioned room using the HBM. It was found that the concrete storage was less effective than the water storage in reducing the swing of the room air temperature for the same storage mass because of the lower heat capacity of the concrete.

Nayak (1987) conducted a comparison of the thermal performance of two types of south-facing water walls including a water wall with concrete and a transwall (a semi-

transparent water wall which allows part of the sunlight to penetrate from outside into the room via the water wall) for a heated space using the HBM. The results showed that the transwall was more effective than the concrete water wall in meeting the daytime heating load. However, a concrete water wall was better from the viewpoints of reducing temperature swings and the overall day-and-night performance because it caused a significant phase shift. Tiwari (1991) also carried out a comparison of the performance of a transwall, a water wall and an isothermal mass for heating in a non-air-conditioned passive solar house for the harsh cold climate of Srinagar, India. A transient analysis based on the HBM was carried out and steady state conditions were achieved after 3 days. They found that the performance of the transwall was better than the isothermal mass and the water wall in terms of both improving night room air temperature and minimising temperature fluctuation.

Experimental studies of water wall have attracted much less attention than analytical investigations. Among the existing experimental studies, Govind et al. (1987) investigated the effect of thermal energy storage (TES) in a winter greenhouse. A greenhouse with a floor area of 15.4-m^2 and a water drum capacity of 3.02-m^3 was constructed for the purpose of growing early summer vegetables. The results indicated that the thermal energy storage by water offered a much higher air temperature than the ambient and minimised the fluctuations of the air temperature in the greenhouse, and a good agreement was obtained between a theoretical model based on the HBM and the experimental measurements. Gupta & Tiwari (2002) developed a transient analysis model based on the HBM to investigate the TES effect of a water mass in a passive greenhouse. They concluded that the temperature fluctuation inside the room decreased with an increase of the water mass and was large in winter and small in summer. An experiment was carried out to validate their model and a fair agreement between the predicted and experimental results was reported. Robinson et al. (2013) designed a full-scale passive solar system utilising heat pipes to transfer latent heat to a storage water tank inside a classroom at the University of Louisville during the spring heating season of 2010. Their field measurements indicated that the thermal storage water tank was heated to a sufficiently high temperature to supply heat to the classroom even during the coldest days of the season. During a long period (4 consecutive days) of low solar isolation, the average hourly heat delivery to the classroom remained positive and was always above 16.6 W/m^2. A computer model based on the HBM was developed and a fair agreement between the predicted and experimental results was reported.

It is seen from the above reviewed literature that the HBM has dominated the water wall research for over three decades. The existing HBMs suffer from two major deficiencies. Firstly,

the convective heat transfer coefficients embodied in the HBMs have been assumed constant in all the models. However, it is understood that the convective heat transfer coefficient depends on the flow and thermal conditions, which may change with time in real-life applications. Therefore, it is necessary to account for the time variation of the convective heat transfer coefficients in the HBMs. And secondly, the radiation exchange between internal surfaces is commonly neglected in the HBMs although some models have considered the radiation emitted by external surfaces (e.g. Sodha et al., 1981, Kaushik & Kaul, 1989). The study of Wu & Lei (2015) has showed that the internal surface-to-surface radiation exchange has a significant impact on the flow structure in a cavity, and thus the internal radiation exchange should be accounted for in the HBM. The purpose of this investigation is to develop a transient heat balance model (THBM), accounting for time variations of both internal and external convective heat transfer coefficients and the internal surface-to-surface radiation exchange, for describing the thermal behaviour of a water wall system. A reduced-scale prototype experiment under the real climate conditions in Sydney has been conducted for validating the model.

3.2 Experimental Setup and Procedures

Fig. 3.1a shows a schematic of the experimental models including a semi-transparent water wall system and a concrete wall system, which are placed side by side. Data collected from both the water wall and concrete wall models are used for validating the THBMs and for performance comparison (the latter is not covered by the present investigation, but direct comparison of the performance of water wall and concrete wall will be carried out in Chapter 4). The two test cells have the same dimensions of 2.4 m in depth (D), 1.2 m in width (W) and 1.2 m in height (H), and are placed on the roof of the Electrical Engineering Building of The University of Sydney. Both the water wall and concrete wall models are oriented to face north in order to receive maximum solar gain. The two models are made of aluminium composite panels, except for the north-facing walls, in order to resemble the essential features of a lightweight residential construction in Australia. The thickness of the aluminium composite panels is 50-mm, which consists of 1-mm thick aluminium sheet on each side and 48-mm thick foam sandwiched by the aluminium sheets for thermal insulation. The north-facing concrete wall comprises a 40-mm thick concrete slab, whereas the north-facing water wall comprises a Perspex cavity filled with water. The Perspex cavity is made of six pieces of 25-mm thick semi-transparent Perspex sheets. The thickness of the water column in the water wall is 100 mm. Special attention has been paid to the water tightness of the Perspex cavity by using a number of 6 mm screws and silicone to

prevent water leakage. The two models are placed on 150-mm height footings (refer to the photograph of the experimental systems shown in Fig. 3.1b) to isolate the test cells from the thermal mass of the roof of the building.

(a)

(b)
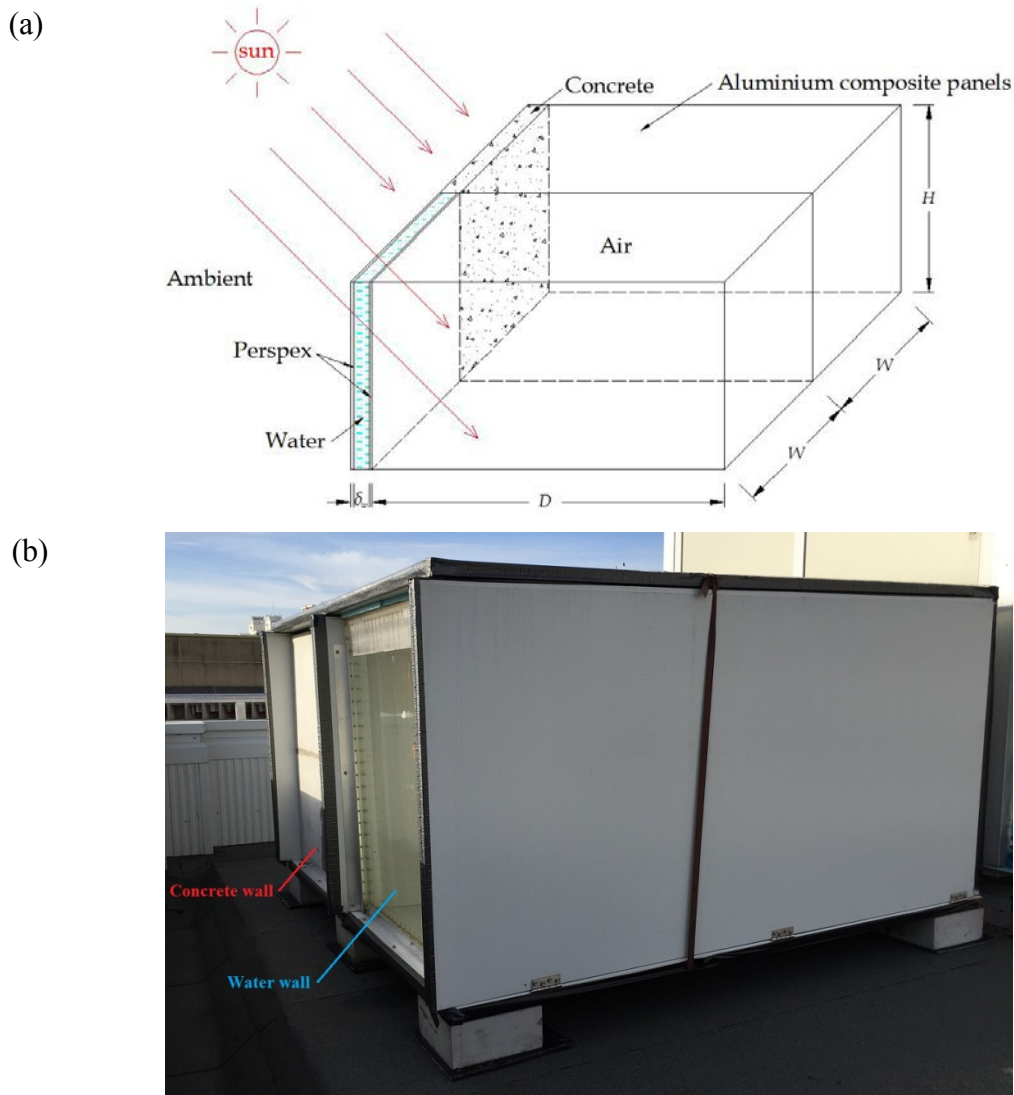
Fig. 3.1 (a) Schematic and (b) a photograph of semi-transparent water wall and concrete wall models.

The experimental water wall model is instrumented to measure the water temperatures inside the Perspex cavity and the air temperatures in the attached test room using seven K-type thermocouples. Fig. 3.2 sketches the arrangement of the thermocouples in the model. Since thermal stratification is expected to occur in both the water and the room air, three thermocouples (#1, #2 and #3) are placed along the centreline of the attached test room at different heights above the floor level (1.0m, 0.6m, 0.2m, respectively, refer to Fig. 3.2b). The remaining four thermocouples are placed in the Perspex cavity for measuring the water

temperatures, with three of these thermocouples (#4, #5 and #6) mounted vertically along the centreline of the water wall and the other one (#7) positioned at the mid-height of the water wall but 380mm offset from thermocouple #5 (refer to Fig. 3.2a). An additional K-type thermocouple is placed outside but near the water wall model to monitor the ambient temperature. Radiation shields are used for the thermocouples installed in the attached test room and the one outside the model to protect them from direct solar radiation. Similarly, the air temperatures in the concrete wall model are measured by three K-type thermocouples, which are placed at the same locations as those in the water wall model. Another four K-type thermocouples are embedded in the concrete slab for measuring the concrete temperatures. These four thermocouples are evenly distributed on the plane of half thickness of the concrete slab.
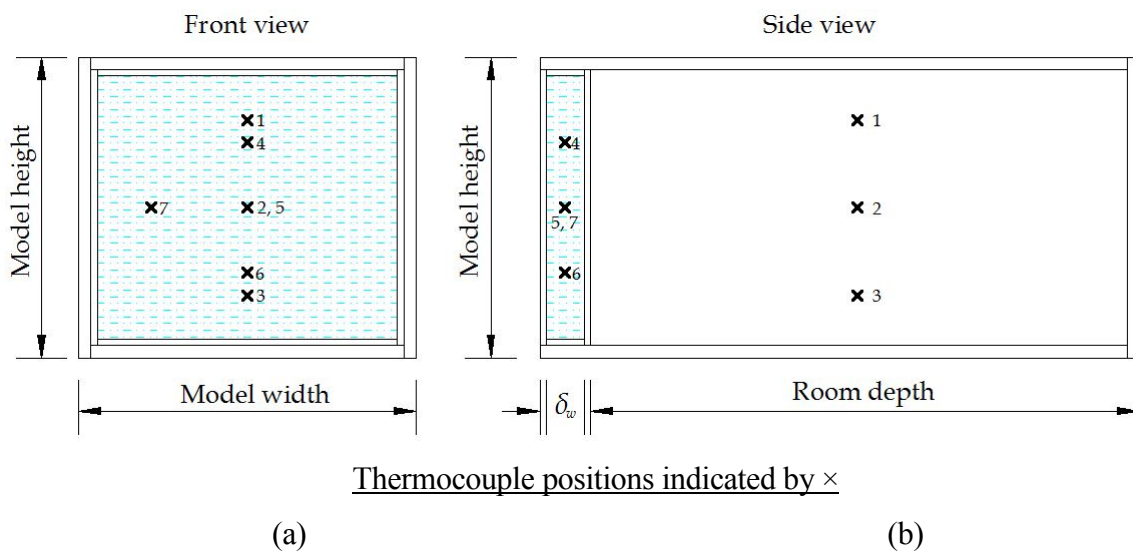
Fig. 3.2 Thermocouple locations in the water wall model (a) front view, and (b) side view.

All the thermocouples are pre-calibrated over the temperature range of 5~50°C using a water bath maintained at constant temperatures by a refrigerated/heating circulator (JULABO, Model FP45), which stabilises temperature to an accuracy of 0.01^{o}C. Fig. 3.3 shows a sample calibration curve for one of the thermocouples. It is clear that the response of the thermocouple is linear over the range of the calibration temperatures. Similar behavior is found with all the other thermocouples.

The calibrated thermocouples are connected to an 8-channel DaqPRO 5300 data logger. The solar radiation and wind speed data is recorded by a personal weather station located near the testing site. The temperature data are recorded at an interval of 10 minutes. The measurements have been carried out for concrete wall from 26 Sept to 15 Oct 2014 and for water wall from 4 May to 31 May 2015.
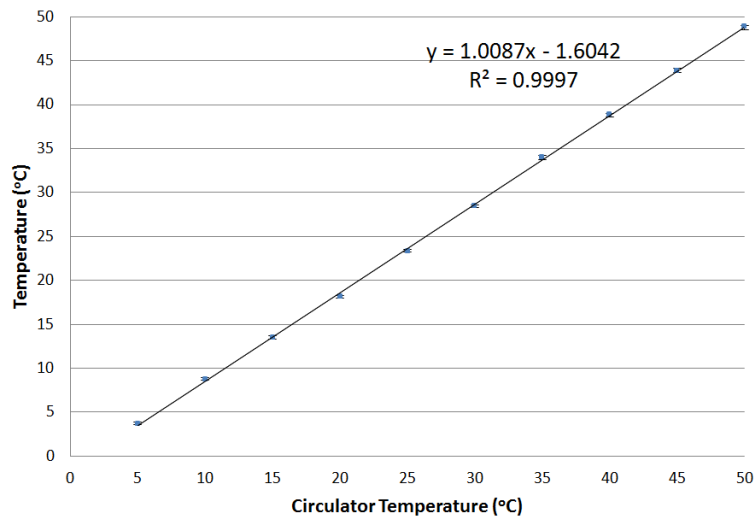
Fig. 3.3 Sample calibration of thermocouples.

3.3 Thermal Modelling

In this section, comprehensive conjugate conduction-convection-radiation models for transient analysis of both the semi-transparent water wall and the concrete wall systems are developed based on the conventional HBM. The transient heat balance models (THBMs) account for time variations of both internal and external convective heat transfer coefficients, the radiation emitted by external surfaces and the internal surface radiation exchanges. The governing equations of the THBMs comprise energy balance equations for individual components of each system. These equations along with initial and climate conditions are solved explicitly using a finite difference method. Grid and time-step dependency tests are carried out to ensure the accuracy of the numerical solution.

3.3.1 Heat Transfer Processes in the Water Wall and Concrete Wall Systems

Fig. 3.4a illustrates various heat transfer processes involved in the semi-transparent water wall model. Conduction takes place in all the solid zones (i.e. Perspex and insulation panels), whereas convection is considered for heat transfer between solid and fluid (i.e. water and air). The radiation emitted by the external surfaces is considered for the outside Perspex and the insulation panels, whereas the internal radiation exchanges are considered between the inside and outside Perspex panels, and between the inside Perspex and the insulation panels. Solar radiation is assumed to be normal to the outside Perspex surface. Most of the solar radiation penetrates through the outside Perspex panel into the water, and some of the solar radiation is absorbed by the water column. The remaining unabsorbed solar radiation then passes through the inside

Perspex panel and reaches the room. Both the outside and inside Perspex panels absorb a small fraction of solar radiation, and the residual solar radiation reaching the room is assumed to be absorbed by the interior surface of the insulation panel. An additional process is included to account for the heat exchange between the room air and the ambient associated with air leakage (infiltration) of the model. The room is filled with air which is considered as a non-participating medium, while the water in the Perspex cavity is a participating medium. The Perspex panels are semi-transparent, whereas the insulation panel is opaque.
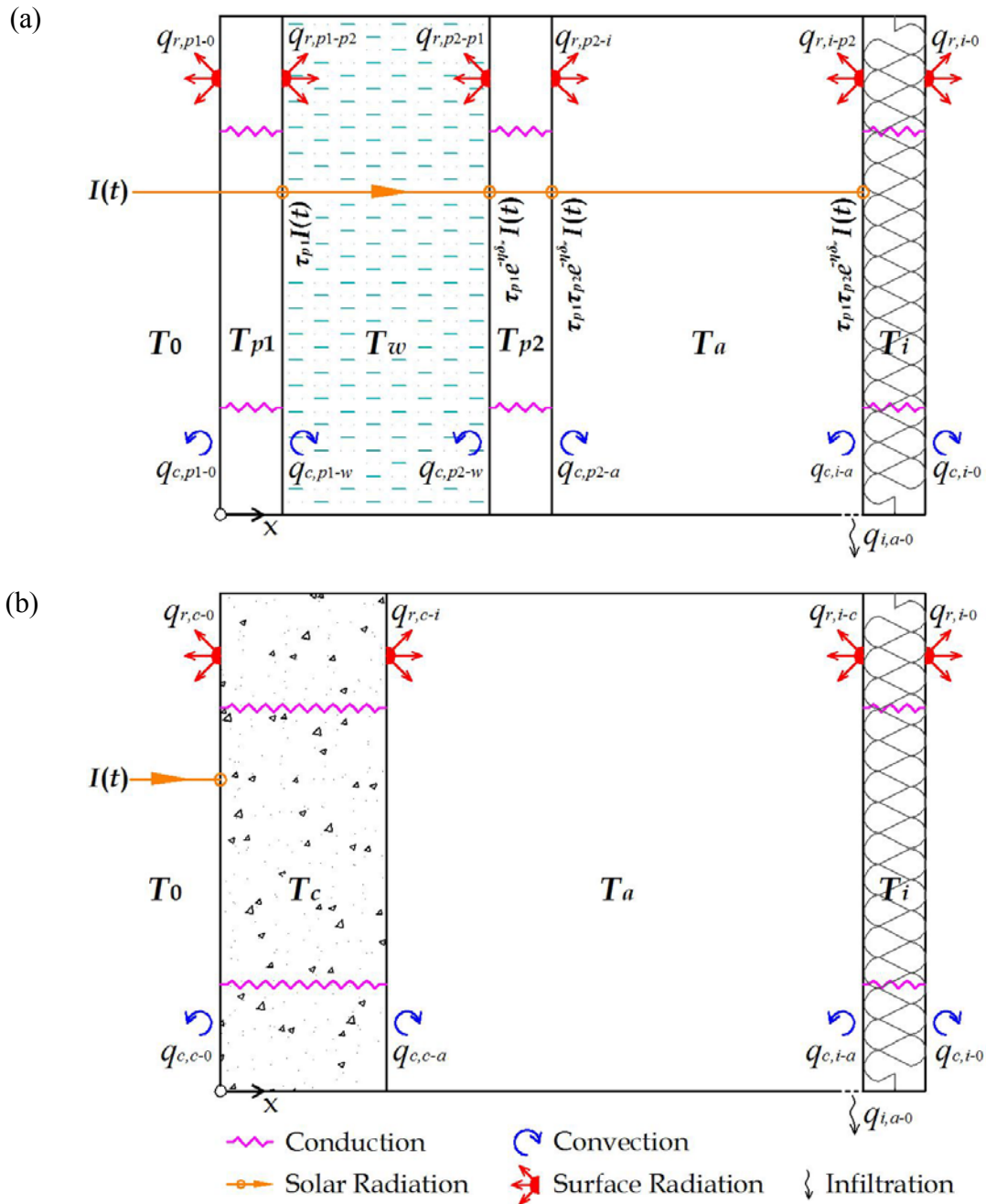
Fig. 3.4 Schematic of heat transfer processes in (a) the semi-transparent water wall system, and (b) the concrete wall system.

Fig. 3.4b depicts various heat transfer processes involved in the concrete wall system, which are similar to those in the water wall system except for that the semi-transparent water wall is replaced by an opaque concrete wall. As a consequence, the solar radiation cannot penetrate into the room, and is partially absorbed at the external surface of the concrete wall. The concrete slab is then heated via conduction and heat is also transferred into the room air by convection. Radiation transfer occurs from the external surfaces of the concrete wall and the insulation panel to the sky, and the radiation exchange takes place between the internal surface of the concrete wall and insulation panel. The infiltration of the concrete wall system is assumed to be the same as that of the water wall system.

3.3.2 Initial and Climate Conditions

In the present THBMs, all the solids and fluids are initially assumed to be at the ambient temperature T_0. Real weather data is used in the THBMs in order to validate the models against in-situ measurements. The intensity of solar radiation, the ambient temperature and the wind speed are the required climate conditions for the present models. The solar radiation and wind speed data are obtained from a weather station located near the testing site, whereas the ambient temperature T_0 is measured by the thermocouple placed outside the experimental model, as described above. Fig. 3.5 shows typical climate data over seven consecutive days (recorded every 10 minutes).

(a)   (b)
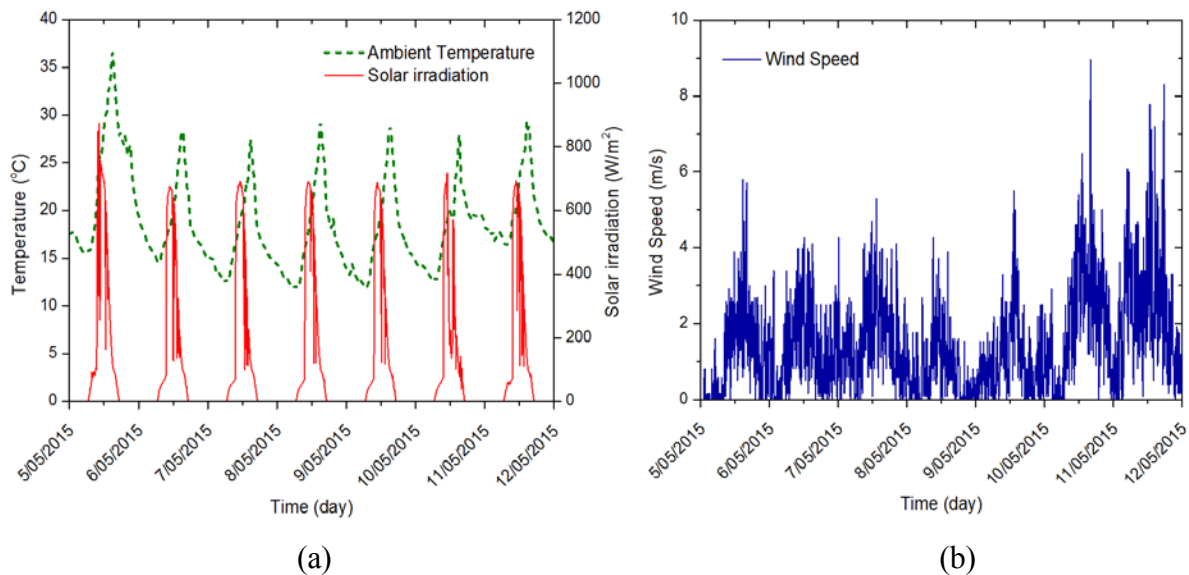
Fig. 3.5 Samples of climate data. (a) solar radiation and ambient temperature; (b) wind speed.

68

3.3.3 Transient Energy Balance Equations for the Water Wall System

In order to simplify the thermal modelling of the semi-transparent water wall and concrete wall systems, the following assumptions are made:

(1) The temperature stratifications inside the water column and the room air are negligible;

(2) The thermo-physical properties of the solids and fluids are constant;

(3) A bulk value is assumed for the attenuation coefficient of solar radiation in water;

(4) Heat conduction through solids is one-dimensional;

(5) The reflection of radiation by the Perspex and insulation panels is negligible.

With the above assumptions, the energy balance equations for each of the components of the semi-transparent water wall system are presented below.

3.3.3.1 Outside Perspex panel

The conduction of heat through the outside Perspex panel is governed by the one-dimensional heat conduction equation:

$$\lambda_p \frac{\partial^2 T_{p1}}{\partial x^2} = \rho_p C_p \frac{\partial T_{p1}}{\partial t} \tag{3.1}$$

where λ_p, ρ_p and C_p are the thermal conductivity, density and specific heat of Perspex, respectively. T_{p1} is the temperature of the outside Perspex panel, x is the horizontal coordinate along which heat is transferred, and t is the time.

The boundary conditions at the external surface ($x = x0$) and the internal surface ($x = x1$, refer to Fig. 3.6) of the outside Perspex panel are written as:

$$-\lambda_p \frac{dT_{p1}}{dx}\bigg|_{x=0} = \alpha_{p1} I(t) + q_{c,p1-0} + q_{r,p1-0} \tag{3.2}$$

$$-\lambda_p \frac{dT_{p1}}{dx}\bigg|_{x=x1} = q_{c,p1-w} + q_{r,p1-p2} \tag{3.3}$$

where α_{p1} is the absorptivity of the outside Perspex panel, and $I(t)$ is the incident solar radiation. $q_{c,p1-0}$ is the convective heat flux between the external surface of the outside Perspex panel and the ambient; $q_{r,p1-0}$ is the radiative flux from the external surface of the outside Perspex panel to the sky; $q_{c,p1-w}$ is the convective heat flux between the internal surface of the outside Perspex panel and the water column; and $q_{r,p1-p2}$ is the radiative heat exchange flux between the outside and inside Perspex panels. Readers may refer to Fig. 3.4a for representations of these convective and radiative heat fluxes, which are evaluated as follows:

$$q_{c,p1-0} = h_0 \left(T_{p1}\big|_{x=x0} - T_0 \right) \tag{3.4}$$

$$q_{r,p1-0} = h_{r,p1-0} \left(T_{p1}\big|_{x=x0} - T_{sky} \right) \tag{3.5}$$

$$q_{c,p1-w} = h_{c,p-w} \left(T_{p1}\big|_{x=x1} - T_w \right) \tag{3.6}$$

$$q_{r,p1-p2} = h_{r,p1-p2} \left(T_{p1}\big|_{x=x1} - T_{p2}\big|_{x=x2} \right) \tag{3.7}$$

where $T_{p1}\big|_{x=x0}$ and $T_{p1}\big|_{x=x1}$ are the external and internal surface temperatures of the outside Perspex panel. $T_{p2}\big|_{x=x2}$ is the external surface temperature of the inside Perspex panel. T_0 and T_w are the ambient temperature and water temperature respectively. h_0 and $h_{r,p1-0}$ are the convective and radiative heat transfer coefficients between the outside Perspex panel and the ambient or the sky; $h_{c,p-w}$ is the convective heat transfer coefficient between the Perspex panel and the water column; and $h_{r,p1-p2}$ is the radiative heat transfer coefficient between the outside and inside Perspex panels.

The convective heat transfer coefficient h_0 between the outside Perspex panel and the ambient is obtained from the following expression (Mirsadeghi et al., 2013), which is implemented in the building energy simulation software ESP-r:

$$h_0 = 3V_{\mathrm{loc}} + 2.8 \ \mathrm{W/m^2 K} \tag{3.8}$$

where V_{loc} is given by

$$V_{\mathrm{loc}} = \begin{cases} 0.5V_{10} & \text{for } V_{10} \leq 1\mathrm{m/s} \\ 0.5 \ \mathrm{m/s} & \text{for } 1\mathrm{m/s} < V_{10} \leq 2\mathrm{m/s} \\ 0.25V_{10} & \text{else} \end{cases} \tag{3.9}$$

Here V_{10} is the wind speed measured at a weather station 10 m above the ground (m/s).

For the natural convection heat transfer between the Perspex panel and the water column, the convective heat transfer coefficient $h_{c,p-w}$ is determined by the following equation:

$$h_{c,p-w} = \frac{Nu\lambda_w}{H} \tag{3.10}$$

where

$$Nu = 0.825 + \frac{0.387Ra_w^{1/6}}{[1+\left(\frac{0.492}{Pr_w}\right)^{9/16}]^{8/27}} \tag{3.11}$$

and the Rayleigh number (Ra_w) and the Prandtl number (Pr_w) are defined as:

$$Ra_w = \frac{g\beta_w \Delta T_{p1-p2} H^3}{\nu_w \kappa_w} \tag{3.12}$$

$$Pr_w = \frac{\nu_w}{\kappa_w} \tag{3.13}$$

where g is the acceleration due to gravity; $\Delta T_{p1-p2} = \left| T_{p1} \right|_{x=x1} - T_{p2} \left|_{x=x2} \right|$ is the temperature difference across the water column; H is the height of the model; β_w, λ_w, v_w and κ_w are the coefficient of thermal expansion, the thermal conductivity, the kinematic viscosity and the thermal diffusivity of water, respectively.

The radiative heat transfer coefficient $h_{r,p1\text{-}0}$ from the outside Perspex panel to the sky is determined by the following equation (Duffie & Beckman, 2013):

$$h_{r,p1-0} = \varepsilon_p \sigma (T_{p1} \big|_{x=x0}^{\;4} - T_{sky}^4)/(T_{p1} \big|_{x=x0} - T_{sky}) \tag{3.14}$$

where ε_p is the emissivity of Perspex, σ is the Stefan-Boltzmann constant (5.669×10^{-8} W/m^2-K^4). T_{sky} is the sky temperature and is determined by the following equation (Li et al., 2015):

$$T_{sky} = 0.0552(T_0)^{1.5} \tag{3.15}$$

The radiative heat transfer coefficient $h_{r,p1\text{-}p2}$ between the outside and inside Perspex panels is determined as follows (Hottel & Sarofim, 1967):

$$h_{r,p1-p2} = \sigma (T_{p1} \big|_{x=x1}^{\;2} + T_{p2} \big|_{x=x2}^{\;2})(T_{p1} \big|_{x=x1} + T_{p2} \big|_{x=x2})/(\frac{1}{\varepsilon_{p1}} + \frac{1}{\varepsilon_{p2}} - 1) \tag{3.16}$$

3.3.3.2 Water column

The energy balance equation of the water column can be written as:

$$\delta_w \rho_w C_w \frac{dT_w}{dt} = \left(1 - e^{-\eta \delta_w}\right)\tau_{p1}I(t) + q_{c,p1-w} + q_{c,p2-w} \tag{3.17}$$

where ρ_w and C_w are the density and specific heat of water; δ_w is the thickness of the water column; η is the attenuation coefficient of solar radiation in water; and τ_{p1} is the transmissivity of the outside Perspex panel. $q_{c,p2\text{-}w}$ is the convective heat flux between the inside Perspex panel and the water column which can be evaluated from the following equation:

$$q_{c,p2-w} = h_{c,p-w}\left(T_{p2} \big|_{x=x2} - T_w\right) \tag{3.18}$$

3.3.3.3 Inside Perspex panel

The conduction of heat through the inside Perspex panel is also governed by the one-dimensional heat conduction equation (3.1) except for that T_{p1} is replaced by T_{p2}, which is the temperature of the inside Perspex panel. The thermal boundary conditions at the external surface ($x = x2$, refer to Fig. 3.6) in contact with water and the internal surface ($x = x3$) in contact with the room air can be written as:

$$-\lambda_p \frac{dT_{p2}}{dx}\bigg|_{x=x2} = \alpha_{p2}e^{-\eta \delta_w}\tau_{p1}I(t) + q_{c,p2-w} + q_{r,p2-p1} \tag{3.19}$$

$$-\lambda_p \left. \frac{dT_{p2}}{dx} \right|_{x=x3} = q_{c,p2-a} + q_{r,p2-i} \tag{3.20}$$

where α_{p2} is the absorptivity of the inside Perspex panel. $q_{c,p2-a}$ is the convective heat flux between the inside Perspex panel and the room air; $q_{r,p2-i}$ is the radiative heat flux between the inside Perspex panel and the insulation panel; and $q_{r,p2-p1}$ is the radiative heat exchange flux between the inside and outside Perspex panels. The above convective and radiative heat fluxes are evaluated as follows:

$$q_{c,p2-a} = h_{c,p-a} \left(\left. T_{p2} \right|_{x=x3} - T_a \right) \tag{3.21}$$

$$q_{r,p2-i} = h_{r,p2-i} \left(\left. T_{p2} \right|_{x=x3} - \left. T_i \right|_{x=x4} \right) \tag{3.22}$$

$$q_{r,p2-p1} = -q_{r,p1-p2} \tag{3.23}$$

where $\left. T_{p2} \right|_{x=x3}$ is the internal surface temperature of the inside Perspex panel (at $x = x3$), and $\left. T_i \right|_{x=x4}$ is the internal surface temperature of the insulation panel (at $x = x4$). $h_{c,p-a}$ is the convective heat transfer coefficient between the inside Perspex panel and the room air; and $h_{r,p2-i}$ is the radiative heat transfer coefficient between the inside Perspex panel and the insulation panel.

The convective heat transfer coefficient $h_{c,p-a}$ can be determined by equations (3.10) and (3.11) with λ_w, Ra_w and Pr_w replaced by λ_a, Ra_a and Pr_a respectively. The Rayleigh number (Ra_a) and the Prandtl number (Pr_a) are defined as:

$$Ra_a = \frac{g\beta_a \Delta T_{p2-i} H^3}{\nu_a \kappa_a} \tag{3.24}$$

$$Pr_a = \frac{\nu_a}{\kappa_a} \tag{3.25}$$

where $\Delta T_{p2-i} = \left| \left. T_{p2} \right|_{x=x3} - \left. T_i \right|_{x=x4} \right|$ is the temperature difference across the room air; β_a, λ_a, ν_a and κ_a are the coefficient of thermal expansion, the thermal conductivity, the kinematic viscosity and the thermal diffusivity of air, respectively.

The radiative heat transfer coefficient $h_{r,p2-i}$ between the inside Perspex panel and the insulation panel is determined by the following equation:

$$h_{r,p2-i} = \sigma \left(\left. T_{p2} \right|_{x=x3}^2 + \left. T_i \right|_{x=x4}^2 \right) \left(\left. T_{p2} \right|_{x=x3} + \left. T_i \right|_{x=x4} \right) / (\frac{1}{\varepsilon_{p2}} + \frac{1}{\varepsilon_i} - 1) \tag{3.26}$$

where ε_i is the emissivity of the insulation panel.

3.3.3.4 Room air

The energy balance equation of the room air can be written as:

$$D\rho_a C_a \frac{dT_a}{dt} = q_{c,p2-a} + q_{c,i-a} - H_i \tag{3.27}$$

where ρ_a and C_a are the density and the specific heat of air; D is the depth of the room; and T_a is the temperature of room air. $q_{c,i-a}$ is the convective heat flux between the insulation panel and the room air; and H_i is the heat loss due to infiltration of the room. These quantities are evaluated from the following equations:

$$q_{c,i-a} = h_{c,i-a}(T_i|_{x=x4} - T_a) \tag{3.28}$$

$$H_i = ACH\rho_a C_a V(T_a - T_0) \tag{3.29}$$

where $h_{c,i-a}$ is the convective heat transfer coefficient between the insulation panel and the room air, which is assumed to be the same as $h_{c,p2-a}$ in this model; V is the volume of the room and *ACH* is the number of air changes per hour due to infiltration, which is equal to 0.5 in this model due to good airtightness.

3.3.3.5 Insulation panel

The conduction of heat through the insulation panel is again governed by the Fourier heat conduction equation:

$$\lambda_i \frac{d^2 T_i}{dx^2} = \rho_i C_i \frac{dT_i}{dt} \tag{3.30}$$

where λ_i, ρ_i and C_i are the thermal conductivity, the density and the specific heat of the insulation panel; and T_i is the temperature of the insulation panel.

The thermal boundary conditions at the internal surface ($x = x4$) and at the external surface ($x = x5$) can be written as:

$$-\lambda_i \frac{dT_i}{dx}\bigg|_{x=x4} = e^{-\eta\delta_w}\tau_{p1}\tau_{p2}I(t) + q_{c,i-a} + q_{r,i-p2} \tag{3.31}$$

$$-\lambda_i \frac{dT_i}{dx}\bigg|_{x=x5} = q_{c,i-0} + q_{r,i-0} \tag{3.32}$$

where τ_{p2} is the transmissivity of the inside Perspex panel. $q_{c,i-0}$ and $q_{r,i-0}$ are the convective heat flux and radiative heat flux between the insulation panel and the ambient or the sky; and $q_{r,i-p2}$ is the radiative heat flux between the insulation panel and the inside Perspex panel, which can be evaluated from the following equations:

$$q_{c,i-0} = h_0(T_i|_{x=x5} - T_0) \tag{3.33}$$

$$q_{r,i-0} = h_{r,i-0}\left(T_i|_{x=x5} - T_{sky}\right) \tag{3.34}$$

$$q_{r,i-p2} = -q_{r,p2-i} \tag{3.35}$$

where $T_i|_{x=x5}$ is the external surface temperature of the insulation panel (at $x = x5$). $h_{r,i-0}$ is the radiative heat transfer coefficient between the insulation panel and the sky, which can be determined by the following equation:

$$h_{r,i-0} = \varepsilon_i \sigma(T_i|_{x=x5}{}^4 - T_{sky}^4)/(T_i|_{x=x5} - T_{sky}) \tag{3.36}$$

3.3.4 Transient Energy Balance Equations for the Concrete Wall System

The energy balance equations for each of the components of the concrete wall system can be developed in the same way as those for the water wall system.

3.3.4.1 Concrete panel

The conduction of heat through the concrete panel is governed by the one-dimensional heat conduction equation:

$$\lambda_c \frac{\partial^2 T_c}{\partial x^2} = \rho_c C_c \frac{\partial T_c}{\partial t} \tag{3.37}$$

where λ_c, ρ_c and C_c are the thermal conductivity, the density and the specific heat of the concrete. T_c is the temperature of the concrete panel.

The boundary conditions at the outside surface ($x = 0$) and at the inside surface ($x = \delta_c$) in contact with the room air can be written as:

$$-\lambda_c \frac{dT_c}{dx}\bigg|_{x=0} = \alpha_c I(t) + q_{c,c-0} + q_{r,c-0} \tag{3.38}$$

$$-\lambda_c \frac{dT_c}{dx}\bigg|_{x=\delta_c} = q_{c,c-a} + q_{r,c-i} \tag{3.39}$$

where α_c is the absorptivity of the concrete panel; and δ_c is the thickness of the concrete panel. $q_{c,c-0}$ and $q_{r,c-0}$ are the convective heat flux and radiative heat flux between the concrete panel and the ambient/sky; $q_{c,c-a}$ is the convective heat flux between the concrete panel and the room air; and $q_{r,c-i}$ is the radiative heat flux between the concrete panel and the insulation panel. The above convective and radiative heat fluxes are evaluated in a similar way to those in the water wall system. In doing so, all the properties of the Perspex panel are replaced by the properties of the concrete panel. For brevity, these equations are not presented here.

3.3.4.2 Room air

The energy balance equation of the room air is the same as equation (3.27) except for that $q_{c,p2-a}$ is replaced by $q_{c,c-a}$.

3.3.4.3 Insulation panel

The conduction of heat through the insulation panel is governed by equation (3.30). The thermal boundary conditions at the internal surface ($x = \delta_c + D$) and at the external surface ($x = \delta_c + \delta_i + D$) can be written as:

$$-\lambda_i \frac{dT_i}{dx}\bigg|_{x=\delta_c+D} = q_{c,i-a} + q_{r,i-c} \tag{3.40}$$

$$-\lambda_i \frac{dT_i}{dx}\bigg|_{x=\delta_c+\delta_i+D} = q_{c,i-0} + q_{r,i-0} \tag{3.41}$$

where δ_i is the thickness of the insulation panel. $q_{c,i-a}$ is the convective heat flux between the insulation panel and the room air; $q_{r,i-c}$ is the radiative heat flux between the insulation panel and the concrete panel; and $q_{c,i-0}$ and $q_{r,i-0}$ are the convective heat flux and radiative heat flux between the insulation panel and the ambient/sky. Similarly, all the heat fluxes can be evaluated in the same way as those described above.

3.3.5 Finite Difference Method

The above heat balance equations along with the initial and climate conditions are solved explicitly by a finite difference method. For doing so, the composite solids and fluids of the semi-transparent water wall system are discretised into a number of nodes as shown in Fig. 3.6. General forms of finite difference equations for boundary nodes of the solids and the interior nodes of the solids and fluids, respectively are given below.

3.3.5.1 For boundary nodes of the solids

The differential term for the boundary nodes of the solids is discretised using a backward-space or forward-space finite difference approximation:

$$\frac{dT_s}{dx} \approx \frac{T_{s,j}^n - T_{s,j-1}^n}{\Delta x_s} \text{ (for } j=P1,\ P2,\ J) \tag{3.42}$$

$$\frac{dT_s}{dx} \approx \frac{T_{s,j+1}^n - T_{s,j}^n}{\Delta x_s} \text{ (for } j=1) \tag{3.43}$$
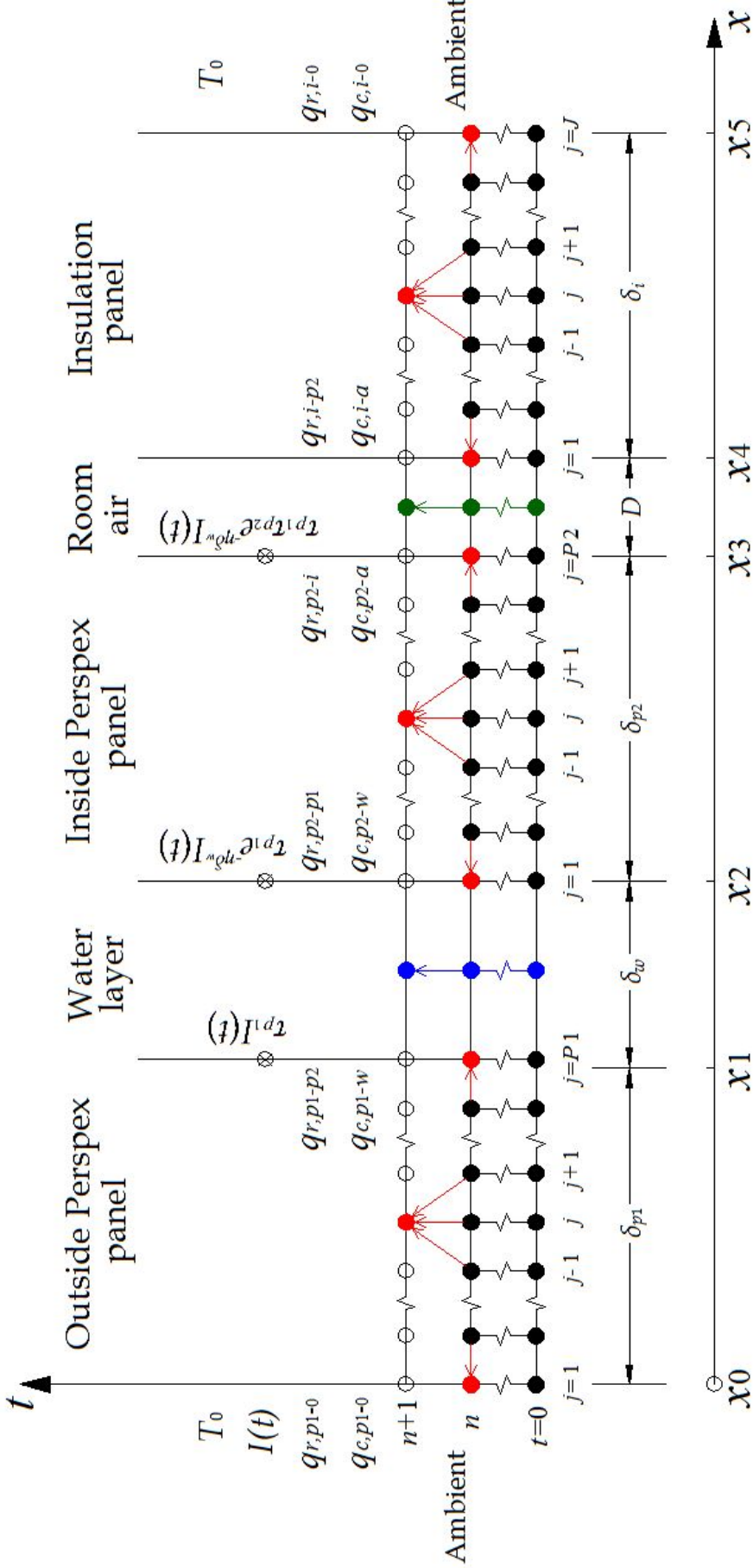
Fig. 3.6 Grid nodes and boundary conditions of the semi-transparent water wall system. n and j represent the time step and the node, $P1$, $P2$ and J are the number of grid node for the outside Perspex panel, inside Perspex panel and insulation panel, respectively. The solid nodes are the solved nodes, and the hollow nodes are the unknown nodes.

where the subscript s denotes solid (i.e. Perspex or insulation panels); the subscripts j-1, j and j+1 denote the node points; the superscript n represents the time-step; and $P1$, $P2$ and J are the number of grid nodes in the Perspex and insulation panels, respectively.

3.3.5.2 For interior nodes of the solids

For the interior nodes of a solid, the heat conduction equation is discretised using a FTCS (Forward Time, Centred Space) finite difference scheme as follows:

$$\frac{T_{s,j}^{n+1}-T_{s,j}^{n}}{\Delta t} = \alpha_s \frac{T_{s,j-1}^{n}-2T_{s,j}^{n}+T_{s,j+1}^{n}}{\Delta x_s^2} \tag{3.44}$$

where α_s is the thermal diffusivity of the solid, which is defined as $\alpha_s = \frac{\lambda_s}{\rho_s C_s}$. λ_s, ρ_s and C_s are the thermal conductivity, density and specific heat of the solid, respectively. The FTCS scheme is easy to implement. However, it can yield unstable solutions that oscillate if Δt is not chosen properly. Stable solutions with the FTCS scheme are obtained when:

$$r = \frac{\alpha \Delta t}{\Delta x^2} < \frac{1}{2} \tag{3.45}$$

3.3.5.3 For fluid nodes

It is worth noting that both the water column and the room air are assumed to be of uniform temperatures, and thus no spatial discretisation in the fluids is needed. The time derivative of the fluid temperature is discretised using a forward in time finite difference approximation as follows:

$$\frac{dT_f}{dt} \approx \frac{T_f^{n+1}-T_f^{n}}{\Delta t} \tag{3.46}$$

where the subscript f represents fluid (i.e. water or air).

3.3.6 Grid and Time-step Dependency Tests

Mesh and time-step dependency tests have been conducted to ensure the accuracy of the numerical solutions. Two different meshes with two corresponding time-steps (21 + 21 + 21 mesh with a time-step of 5s and 11 + 11 + 11 mesh with a time-step of 20s) are tested for the water wall system. Since the fluid (water and air) temperatures are assumed uniform, the mesh dependency tests are only conducted for the solid zones (Perspex and insulation panels, i.e. $P1 = P2 = J = 21$ and 11 respectively). The size of the mesh and the corresponding time-step are chosen so that the value of r given by equation (3.45) remains constant.
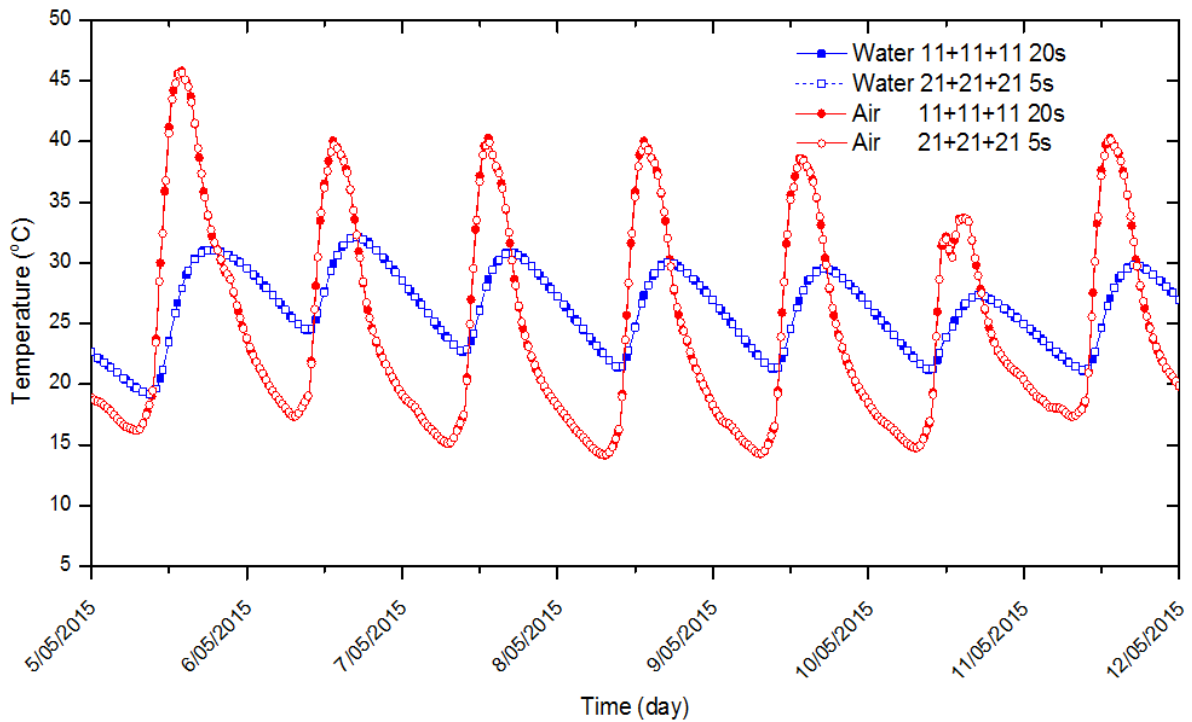
Fig. 3.7 Predicted water and air temperatures over seven consecutive days for the semi-transparent water wall model with the different meshes and time-steps.

Fig. 3.7 presents typical predicted water and air temperatures over seven consecutive days obtained with the different meshes and time-steps. It is clear that both the predicted water and air temperatures obtained with the different meshes and time-steps overlap with each other. Accordingly, the 11 + 11 + 11 mesh and the 20s time-step are selected for the current water wall model. Similarly, a mesh and time-step dependency test for the concrete wall model shows that an 11 + 11 mesh and a 20s time-step provide sufficient spatial and temporal resolutions for the concrete wall system, and thus are adopted in this study.

3.3.7   Spin-up of the THBMs

In order to minimise the start-up effect, a spin-up test is carried out to determine the number of thermal cycles required to achieve a quasi-steady stage for both the water wall and concrete wall models. For this purpose, the intensity of solar radiation, the ambient temperature and the wind speed are assumed to vary with time according to sinusoidal functions over diurnal cycles (the solar radiation is only available for half of the cycle corresponding to the daytime period).

Table 3.1 Variations of the maximum and minimum fluid temperatures in the water wall system.

Thermal cycle no.	$\|T_d^{max} - T_{d-1}^{max}\|/\Delta T_a$ (%)		$\|T_d^{min} - T_{d-1}^{min}\|/\Delta T_a$ (%)	
	Water	Air	Water	Air
2	56.03	20.92	85.54	27.58
3	23.86	8.78	35.05	11.83
4	9.89	3.65	14.39	4.99
5	4.06	1.51	5.89	2.06
6	1.66	0.62	2.41	0.85
7	0.68	0.25	0.98	0.35

The test is carried out for a case with the maximum solar radiation of 800 W/m², maximum wind speed of 6 m/s, and a diurnal temperature swing of 20°C. The maximum and minimum water and air temperatures over each diurnal cycle are compared with those in the previous cycle, and the results are given in Table 3.1. Here, T_{d-1}^{max} and T_d^{max} are the maximum temperature over the thermal cycle $d-1$ and d, T_{d-1}^{min} and T_d^{min} are the minimum temperature over the thermal cycle $d-1$ and d, and ΔT_a is the diurnal temperature swing. It is clear in Table 3.1 that the variations of the maximum and minimum temperatures between consecutive cycles reduce quickly as the number of cycle increases. After 7 full cycles, the variations of both the water and air temperatures become less than 1%. It is therefore assumed that a quasi-steady state has been established in the water wall system after 7 diurnal cycles. Similarly, a spin-up test conducted for the concrete wall system shows that a quasi-steady stage is achieved after 2 full diurnal cycles. In the following section, the results from the THBMs are presented only after the quasi-steady state has been achieved.

3.4   Results and Discussions

3.4.1   Validation of the THBM for the Concrete Wall System

The THBM for the concrete wall system described in Section 3.3.4 is validated here. Due to the simplicity of the concrete wall system compared to the water wall system, it can be easily modelled using the commercial code DesignBuilder (DesignBuilder Software, 2009). Therefore, the present THBM is validated against both the field data and the DesignBuilder model.

3.4.1.1 DesignBuilder model

DesignBuilder is one of the most comprehensive user interfaces for EnergyPlus, a dynamic thermal simulation engine, which is the U.S. DOE (Department of Energy) building energy simulation program for modelling and calculation of heating, cooling, lighting, ventilating, and other energy flows in buildings. The versions of the programs used for the present investigation are DesignBuilder 4.2.0.054 and EnergyPlus v.8.1. In order to validate the THBM for the concrete wall system, a three-dimensional building model with the same dimensions, orientation and materials as the experimental concrete wall system is established in DesignBuilder to simulate the transient air temperature in the room. Hourly weather data from a weather station near the testing site is adopted in the DesignBuilder simulation. The simulation has been conducted with a time-step of 10 mins over the time period from 26 Sept to 15 Oct 2014, during which field measurements of temperatures were carried out.

3.4.1.2 Results for the concrete wall system

The THBM is also run over the same time period using the real climate data. The thermal properties of various materials involved in the model are listed in Table 3.2.

Table 3.2 Material properties (adopted from The Engineering Toolbox)

Material	ρ (kg/m^3)	C (J/kg K)	λ (W/m K)	α	ε
Perspex	1180	1260	0.2	0.1	0.97
Aluminium composite panel	146.4	1284.4	0.1	1	0.9
Concrete	2400	880	0.8	0.6	0.88
Water	997	4180	0.6	-	-
Air	1.22	1000	0.0259	-	-

Fig. 3.8 displays the predicted air temperatures in the concrete wall system using the current THBM and DesignBuilder. The simulated results are also compared against the experimental data in this figure. Here, the experimental air temperature represents the arithmetic mean temperature of the readings of the three thermocouples placed inside the air space. In general, the predicted air temperature by the THBM and DesignBuilder are in good agreements with the field measurements.
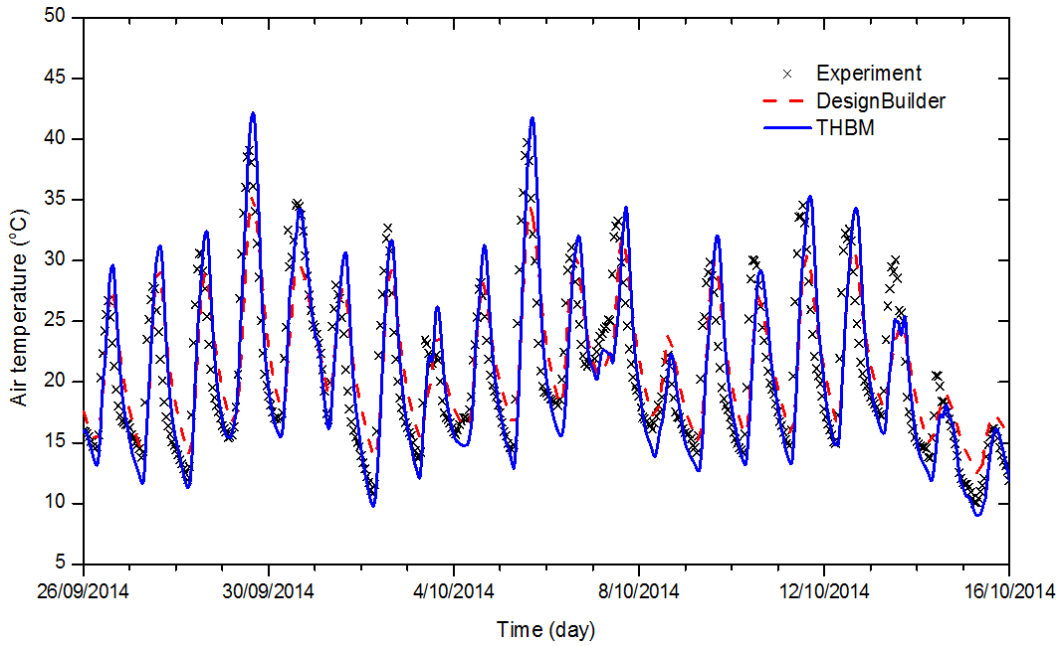
Fig. 3.8 Predicted and measured air temperatures in the concrete wall system.

Further quantitative comparisons of the results obtained with the THBM and DesignBuilder are shown in Table 3.3. In this table, T_A is the difference between the measured maximum and minimum air temperatures over the testing period (20 days); $\overline{|T - T_{EXP}|}$ represents the average absolute value of the temperature difference between the predicted temperature (by either DesignBuilder or the THBM) and the experimental temperature; $(T_{max} - T_{max}^{EXP})'$ is the standard deviation of the variations between the daily maximum temperature predictions and measurements; and $(T_{min} - T_{min}^{EXP})'$ is the standard deviation of the variations between the daily minimum temperature predictions and measurements. It is clear in Fig. 3.8 and Table 3.3 that the THBM gives an overall better prediction of the mean, maximum and minimum temperatures than DesignBuilder. In particular, the maximum temperature during the day predicted by the THBM is better than that predicted by DesignBuilder by approximately 2%. These comparisons confirm that the present THBM can be used to predict the air temperature in the concrete wall system with confidence.

Table 3.3 Performance of the THBM and DesignBuilder in the concrete wall system.

Quantities	DesignBuilder vs EXP (%)	THBM vs EXP (%)
$\overline{|T - T_{EXP}|} / T_A$	10.45	9.72
$(T_{max} - T_{max}^{EXP})' / T_A$	9.31	7.38
$(T_{min} - T_{min}^{EXP})' / T_A$	3.63	2.82

81

3.4.2   Validation of the THBM for the Semi-transparent Water Wall System

Simulation of the semi-transparent water wall system using the above described THBM has been conducted using real climate data from 4 May to 31 May 2015. Since the above spin-up test has demonstrated that a quasi-steady stage is achieved after the seventh thermal forcing cycle for the water wall system, only the data obtained after Day 7 (e.g. from 11 May to 31 May 2015) are presented here.
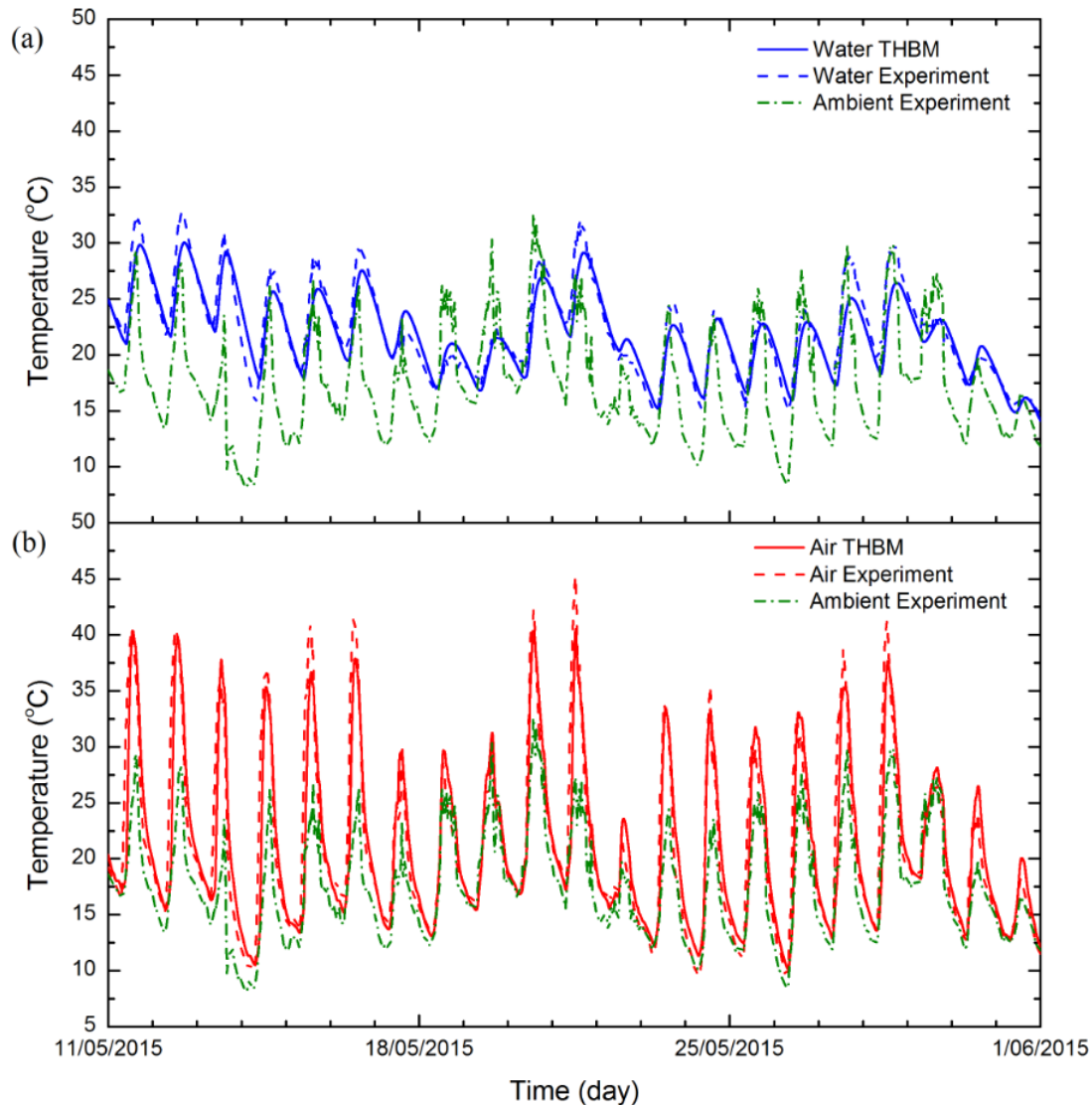
Fig. 3.9 Predicted and measured (a) water and (b) air temperatures in the semi-transparent water wall system.

Fig. 3.9 shows the predicted and measured water and air temperatures in the semi-transparent water wall system, assuming a water attenuation coefficient of $\eta = 2$ m^{-1} in the theoretical model (Mao et al., 2007). It will be demonstrated in Section 3.4.3 below that the

predicted water and air temperatures are insensitive to the attenuation coefficient of the solar radiation. Similar to what is described in Section 3.4.1 for the concrete wall system, the experimental air and water temperatures shown in Fig. 3.9 represent the arithmetic mean temperatures of the readings from all the thermocouples placed inside the air space and water column, respectively. It is clear in this figure that, in general, the predicted water and air temperatures by the THBM are in good agreements with the experimental measurements. It is interesting to note that in the present water wall system, the fluctuation of the water temperature is much less than that of the air temperature. In most of the days, both the predicted and measured air temperatures are much higher than the ambient temperature during the daytime and are slightly higher than the ambient temperature during the night.

Quantitative comparison of the results obtained with the THBM against the field measurements is tabulated in Table 3.4. In this table, $T_{A,water}$ is the difference between the measured maximum and minimum water temperatures over the testing period (21 days); and $T_{A,air}$ is the difference between the measured maximum and minimum air temperatures over the same testing period. It is seen in this table that the THBM produces an overall good prediction for both the water and air temperatures, with less than 8% variations from the experimental measurements. It is also found that the prediction of the air temperature is more accurate than the prediction of the water temperature, and the prediction of the daily minimum water and air temperatures is better than the prediction of the daily maximum water and air temperatures. The above comparisons confirm that the present THBM is capable of predicting the water and air temperatures in the semi-transparent water wall system to a reasonable level of accuracy, and thus will be adopted to explore the thermal performance of the semi-transparent water wall system over a range of parameters. The reason why the THBM with the simplified assumption could still provide reasonable predictions of temperatures may be because the percentage of the diffuse solar incident radiation is small compared with its direct counterpart. And also because most of the sun light penetrates into the room, only little solar energy is absorbed by water. The water temperature is also affected by the Perspex panels through heat conduction. Therefore a bulk value of the attenuation coefficient of solar radiation in water results in a prediction that is close to the prediction that would be obtained if a spectrally dependent attenuation coefficient is adopted.

Table 3.4 Performance of the THBM in the semi-transparent water wall system.

Water	%	Air	%
$\overline{\lvert T - T_{EXP} \rvert}/ T_{A,water}$	6.17	$\overline{\lvert T - T_{EXP} \rvert}/ T_{A,air}$	5.24
$(T_{max} - T_{max}^{EXP})'/T_{A,water}$	7.45	$(T_{max} - T_{max}^{EXP})'/T_{A,air}$	6.16
$(T_{min} - T_{min}^{EXP})'/ T_{A,water}$	4.92	$(T_{min} - T_{min}^{EXP})'/ T_{A,air}$	2.25

3.4.3 Sensitivity Analysis

In this section, the above-described and validated THBM is used to assess the thermal performance of the semi-transparent water wall system under different configurations. The control parameters considered here include the transmissivity of the Perspex panel, the thickness of the water column and the attenuation coefficient of solar radiation in water. The simulated results are described below.

3.4.3.1 Effect of the transmissivity of the Perspex panel

In reality, the transmissivity of the Perspex or glass panel can be easily altered by tinting the panel. A range of solar window films are available in the market, which have different transmissivities. Fig. 3.10 exhibits three different tinting arrangements of the semi-transparent water wall system that are analysed in this study. Case A has tints adhered to both the inside and outside Perspex panels, whereas Cases B and C have tint sticked to either the outside or inside Perspex panel only.
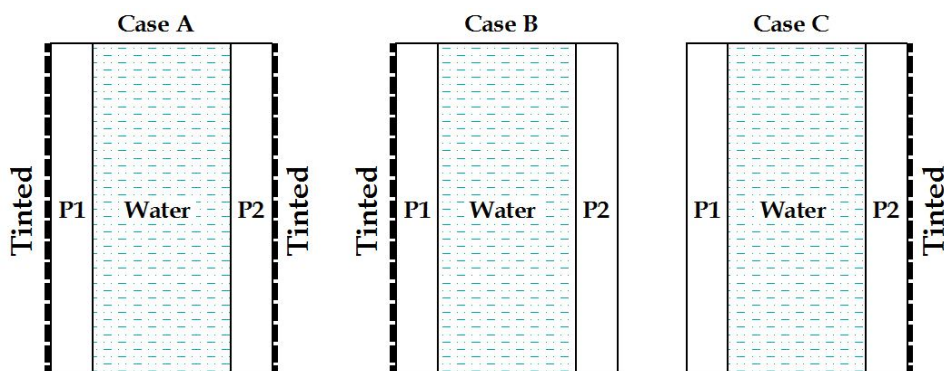
Fig. 3.10 Different tinting arrangements of the semi-transparent water wall system.

Fig. 3.11 depicts the predicted water and air temperatures in the semi-transparent water wall system obtained with three different transmissivities of the Perspex panels for Case A. The transmissivities are chosen based on two different window tints which allow 75% and 50% of

the light through, respectively. Accordingly, the corresponding total transmissivities of tinted Perspex panels are 0.675 (i.e. 0.75 × 0.9) and 0.45 (i.e. 0. 5 × 0.9), respectively. It is seen in Fig. 3.11a that the predicted water temperature decreases significantly when the Perspex transmissivity is reduced from 0.9 to 0.45. However, the pattern of the water temperature fluctuation remains unchanged. In terms of the predicted air temperature (refer to Fig. 3.11b), significant reduction is observed for the daily maximum air temperature with the reduction of the Perspex transmissivity, whereas the daily minimum temperature does not change much.
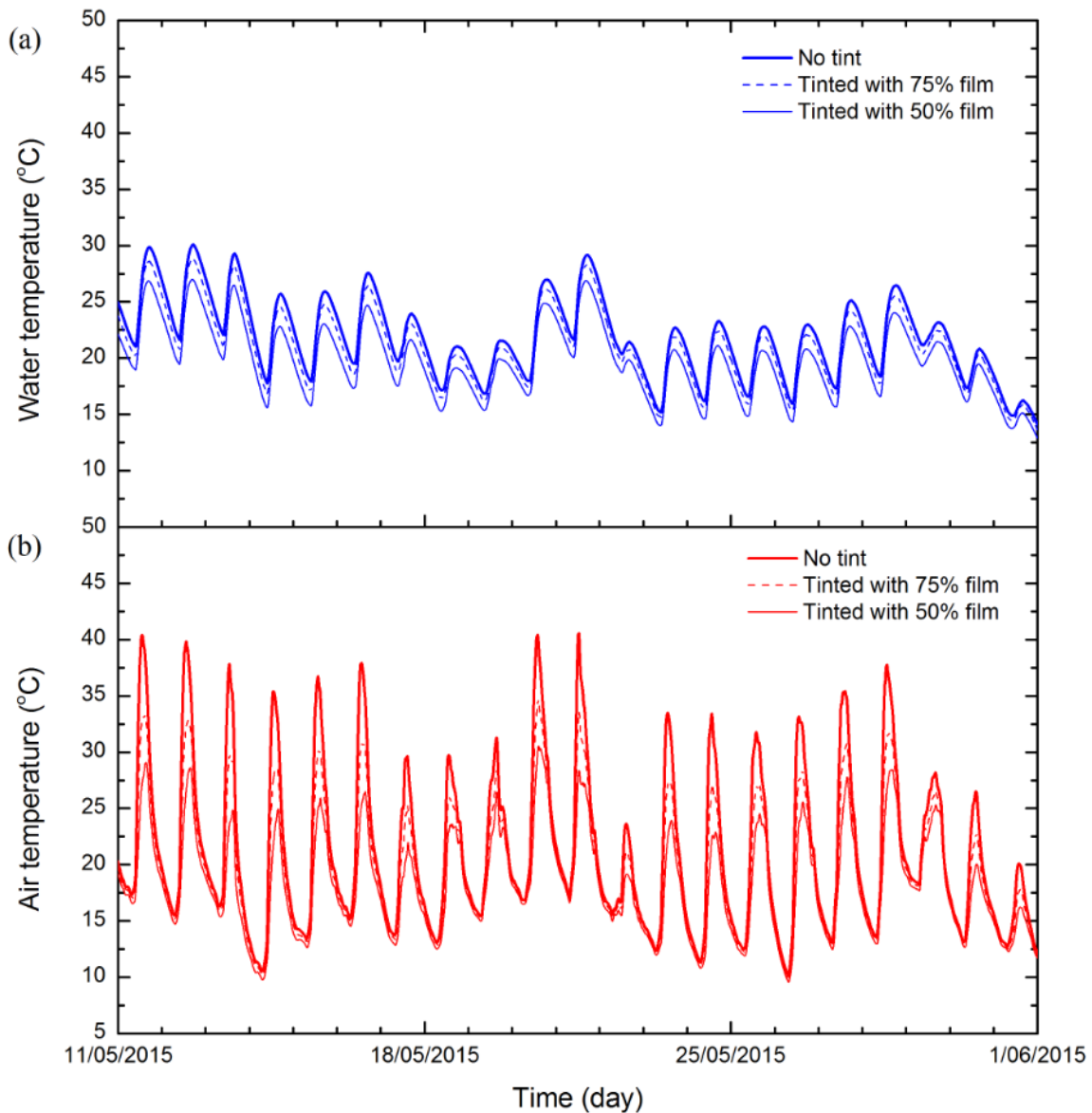
Fig. 3.11 Predicted (a) water and (b) air temperatures with different transmissivities of the Perspex panels (Case A).

Table 3.5 Performance of the semi-transparent water wall system with different tinting arrangements.

Case	τ_{p1}	τ_{p2}	$\dfrac{(T_{max}-T_{max}^{ref})'}{T_{ref}}$ (%)	$\dfrac{(T_{min}-T_{min}^{ref})'}{T_{ref}}$ (%)
A-1	0.75×0.9	0.75×0.9	6.17	0.34
A-2	0.75×0.9	0.5×0.9	7.78	0.31
A-3	0.5×0.9	0.75×0.9	8.82	0.71
A-4	0.5×0.9	0.5×0.9	9.65	0.69
B-1	0.75×0.9	0.9	4.16	0.38
B-2	0.5×0.9	0.9	7.88	0.74
C-1	0.9	0.75×0.9	2.89	0.10
C-2	0.9	0.5×0.9	5.61	0.20

Detailed comparisons of the performance of the semi-transparent water wall system with different tinting arrangements are shown in Table 3.5. In this table, T_{ref} represents the difference between the predicted maximum and minimum air temperatures over the testing period (21 days) without tint; $(T_{max} - T_{max}^{ref})'$ is the standard deviation of the variations of the daily maximum temperatures between the cases with and without tint; and $(T_{min} - T_{min}^{ref})'$ is the standard deviation of the variations of the daily minimum air temperatures between the cases with and without tint. It is seen in this table that the difference of the predicted daily maximum air temperatures between the cases with and without tint increases (due to the reduction of the maximum room air temperature) with the decrease of the transmissivity of the tint. Among all the cases considered here, Case A-4 has the best performance in reducing the daily maximum air temperature. The comparison of Cases B-1, B-2, C-1 and C-2 indicates that the reduction of the daily maximum air temperature is larger when the tint is attached on the outside Perspex panel. It is also found that the difference among Cases B-2, A-2, A-3 and A-4 is relatively small, suggesting that tinting the outside Perspex panel alone can provide sufficient reduction of the daily maximum air temperature, and thus is more economical compared to tinting both the outside and inside Perspex panels. It is interesting to note that the effect of the transmissivity of the Perspex panel on the predicted diurnal minimum air temperature is much less significant than that on the predicted diurnal maximum air temperature. The difference between the predicted minimum air temperatures for the tinted and untinted models is in the order of 1% or less. Therefore, reducing the Perspex transmissivity can prevent over-heating of the indoor environment during the day while still maintaining the essential comfort level at the night.

3.4.3.2 Effect of the thickness of the water column

Fig. 3.12 displays the predicted water and air temperatures in the semi-transparent water wall system obtained with three different thicknesses of the water column. Clearly, increasing the thickness of the water column results in smaller water temperature fluctuation (refer to Fig. 3.12a). It is also clear in Fig. 3.12b that the daily peak air temperature decreases significantly with the increase of the water column thickness. Therefore, increasing the water column thickness is another way to prevent over-heating of the indoor environment during the day. In reality, however, it is technically difficult to change the thickness of the water column after the completion of construction, and thus the thickness of the water column should be carefully designed before construction begins.
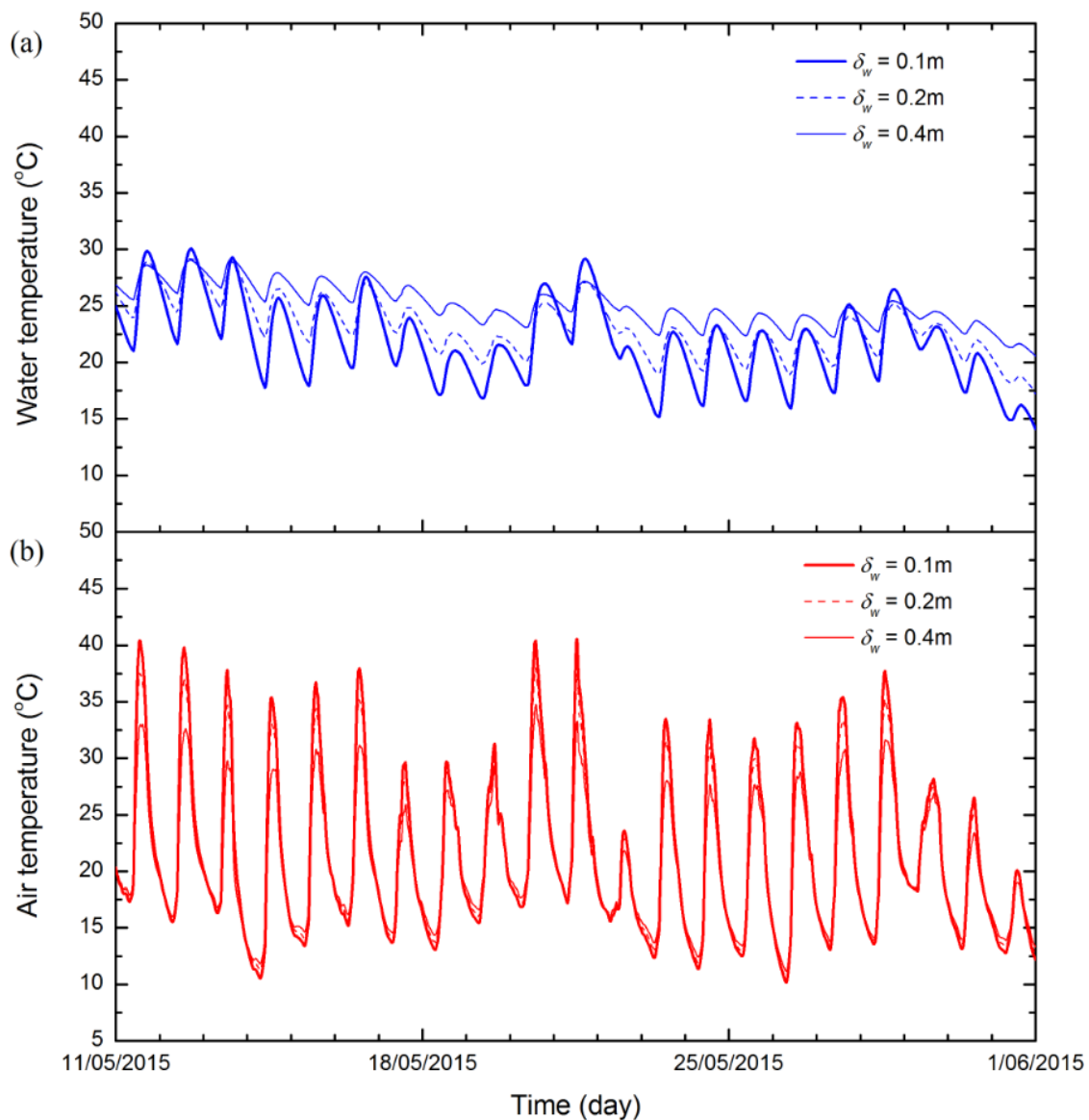
Fig. 3.12 Predicted (a) water and (b) air temperatures with different thicknesses of the water column.

3.4.3.3 Effect of the attenuation coefficient of solar radiation in water

In practice, higher attenuation coefficients of solar radiation in water can be obtained by adding different colour dyes into water. In order to quantify the attenuation coefficient of solar radiation in water with different colour dyes, a lab experiment is carried out using an artificial light (a halogen lamp with a colour temperature of 3200K). Here a bulk attenuation coefficient is assumed for the artificial light. The measurement is taken in a transparent Perspex box filled with water to different depths and illuminated from the top by the artificial light generated by the halogen lamp. The intensities of the light entering the water surface and leaving the bottom of the tank are measured for different water depths, and the attenuation coefficient of water is calculated from the measured light intensities. Subsequently, different dyes (QUEEN Food Colouring, Pillar Box Red, Green and Blue) are added into clear water to form dye solutions with different concentrations, and the above measurement is repeated to determine the attenuation coefficients of different dye solutions. Fig. 3.13 illustrates the attenuation coefficient of the artificial light in water with different colour dyes and at different concentrations with reference to pure tap water ($\eta_{water} = 8.7$ m^{-1}, which is measured in the lab experiment). The thickness of water column is fixed at 100 mm which is the same as the water column thickness in the semi-transparent water wall system. It is seen in this figure that adding colour dye into water increases the attenuation coefficient of the artificial light in water by a factor of 1.1 to 1.8. Significant increase of the bulk attenuation coefficient of the artificial light is observed in water with blue dye, whereas the red dye has the smallest influence on the bulk attenuation coefficient of the artificial light in water.
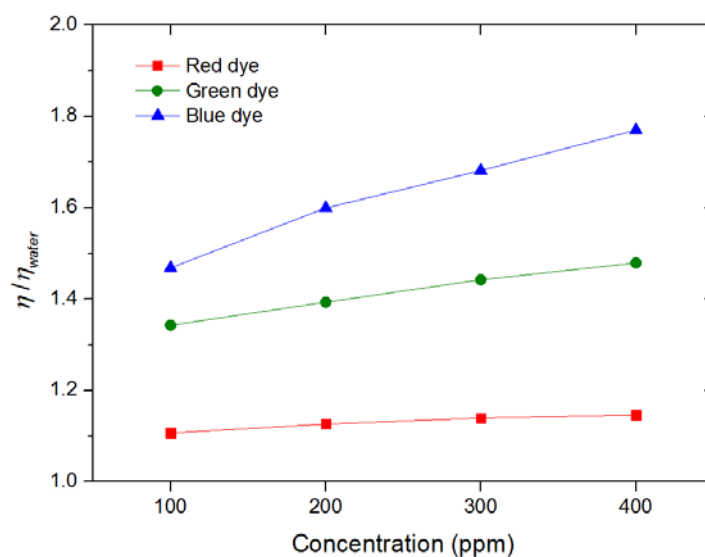
Fig. 3.13 Measured bulk attenuation coefficients of an artificial light in water with different colour dyes and concentrations.

Fig. 3.14 demonstrates the predicted water and air temperatures in the semi-transparent water wall system obtained with three different colour dyes at a fixed concentration of 200 ppm according to the above-described lab experiment. In order to simplify the model, it is assumed that the dependence of the light attenuation coefficient in water on the dye colour and concentration is the same for both the artificial light and solar radiation across the entire wavelength. In Fig. 3.14, the 'Original' case adopts the same attenuation coefficient of $\eta = 2 \text{ m}^{-1}$ as that adopted above. Accordingly, the attenuation coefficients of solar radiation in water with red, green and blue dyes are determined to be 2.25 m^{-1}, 2.79 m^{-1} and 3.20 m^{-1} respectively based on the dependence curves shown in Fig. 3.13. As can be seen in Fig. 3.14, the predicted daily maximum water and air temperatures decrease only slightly with the addition of the colour dyes, which indicates that adding the colour dyes into water has a very limited influence on the reduction of both the water and air temperatures.
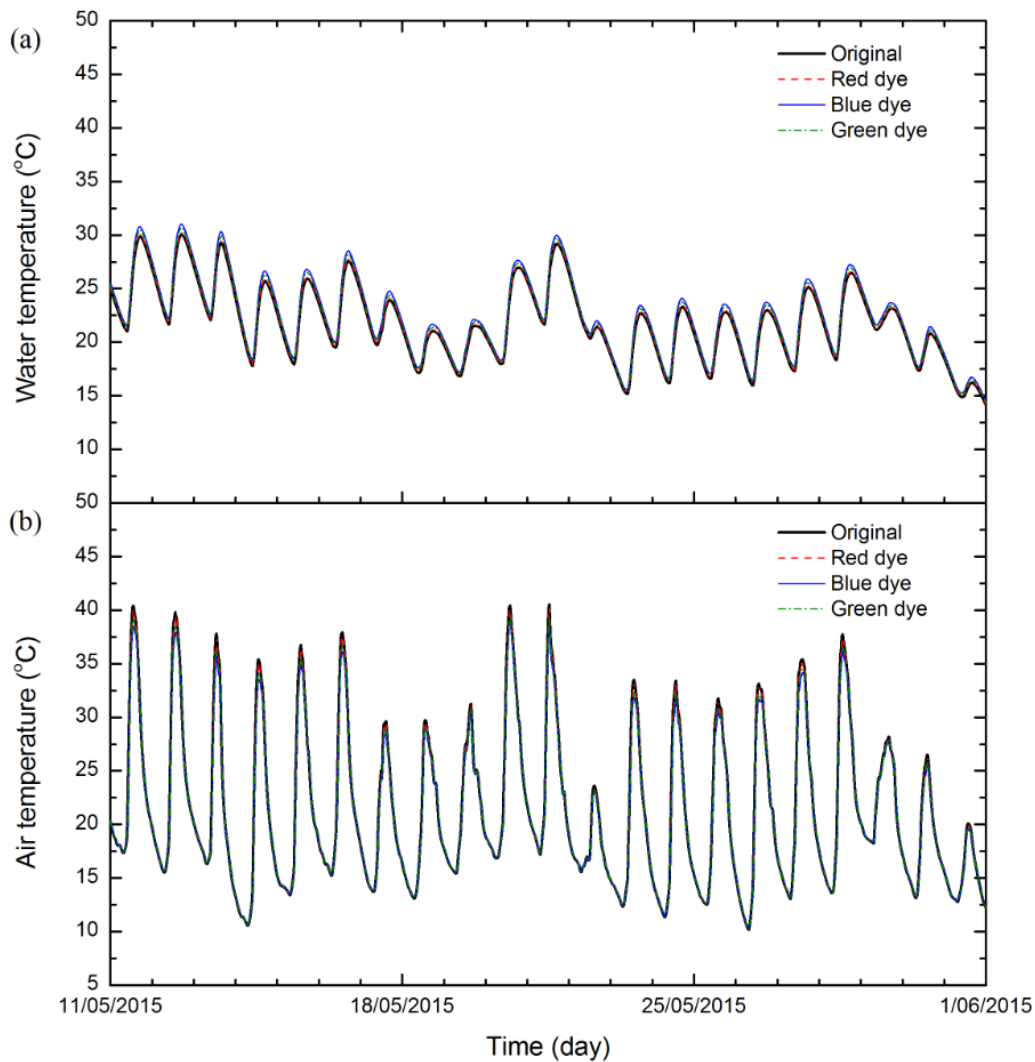
Fig. 3.14 Predicted (a) water and (b) air temperature with different attenuation coefficients of solar radiation in water.

3.4.4 Discussions

It is noted in Fig. 3.9 that an issue of over-heating may occur in the room of the semi-transparent water wall system. In this study, we focus on the thermal comfort condition in terms of the interior temperature only. Consideration of other thermal comfort parameters (e.g. humidity, air velocity) is beyond the scope of this study. For approximately 112 hours out of the 504-hours of the testing period, the room air temperature exceeds 26.84$^\mathrm{o}$C, which is the threshold for an uncomfortable indoor environment according to the adaptive comfort model provided by ASHRAE Standard 55 (ASHRAE, 2010). The over-heating occurs because the semi-transparent water wall system allows a significant portion of the sunlight to penetrate from the outside through the water column and reach the room. Meanwhile, the model room is well insulated with the aluminium composite panels, and thus the heat from the solar radiation is trapped inside the room.

In order to prevent over-heating of the room air and provide a comfortable environment in the room, various strategies can be taken. Among these strategies, some of the strategies discussed in the above-described sensitivity analysis can be easily implemented with minimum change to the semi-transparent water wall system. The only exception is for changing the thickness of the water column, which may be complicated and costly in practice. It is revealed in Section 3.4.3 above that the peak room air temperature can be reduced by decreasing the transmissivity of the Perspex panel and increasing the thickness of the water column and the attenuation coefficient of solar radiation in water. Fig. 3.15 presents the effects of the various strategies on the reduction of the number of over-heating hours in the room. It is clear that the number of over-heating hours is reduced significantly when the Perspex transmissivity is reduced from 0.9 to 0.45 for all three tinting arrangements on the Perspex panel(s). The thickness of the water column and the attenuation coefficient of solar radiation in water have insignificant effects on preventing over-heating. In consideration of the effectiveness, practicality and cost of the different strategies for preventing over-heating, it is clear that reducing the Perspex transmissivity offers the best choice as it can be achieved by simply attaching solar window films to the Perspex panels. Among the three tinting arrangements, tinting the external surface of the Perspex panel (Case B) offers the most cost effective means for reducing over-heating hours as it only requires tinting on one side of the Perspex panel.
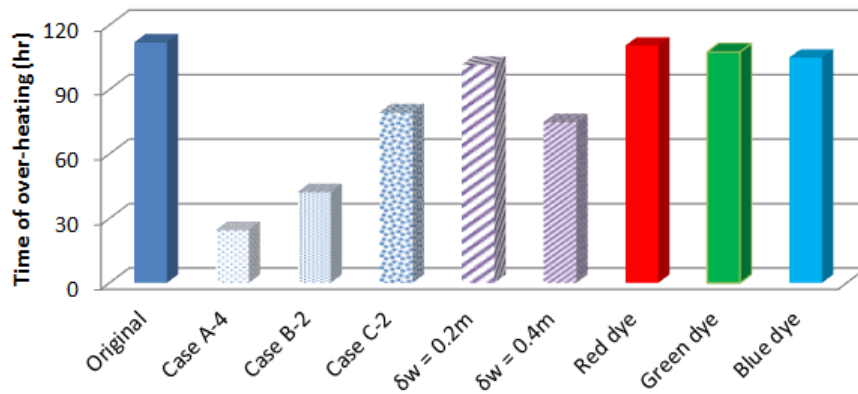
Fig. 3.15 The effects of various strategies on the reduction of the over-heating hours in the room.

3.5 Conclusions

In this study, a transient heat balance model (THBM) based on the energy conservation concept for predicting the thermal behaviour of a semi-transparent water wall system is developed. Time variations of both internal and external convective heat transfer coefficients, the radiation emitted by external surfaces and the internal surface-to-surface radiation exchange are all accounted for in this transient model. Real climate data is used to run the THBM, and the model's results are compared with field measurements. The comparison shows a generally good agreement between the prediction and field data. As a further validation of the THBM, a concrete wall system is considered using the THBM and DesignBuilder. Again, a good agreement between the THBM prediction and field data is achieved, and to a certain extent, the present THBM performs slightly better than DesignBuilder.

The validated THBM is then applied to examine the effects of various parameters on the thermal performance of the semi-transparent water wall system. It is found that the reduction of the Perspex transmissivity results in a significantly lower water and air temperatures, especially for the diurnal maximum air temperatures. The results also indicate that adding different colour dyes into water has an insignificant impact on the water and air temperatures, whereas the increase of the thicknesses of the water column can reduce the fluctuation of the water temperature and the daily peak temperature of the room air. Among the three strategies considered in this study, reducing the Perspex transmissivity is the most effective, practical and economical way to mitigate over-heating in the semi-transparent water wall system, which can be achieved by attaching solar window films to the Perspex panels. Among the three tinting

arrangements on the Perspex panel(s), tinting the outside Perspex panel offers the most cost effective way to prevent over-heating.

References

ASHRAE Standard 55–2010, 2010. Thermal Environmental Conditions for Human Occupancy. Atlanta, GA: American Society of Heating Refrigerating and Air-Conditioning Engineers.

DesignBuilder Software, 2009. DesignBuilder 2.1 User's Manual. UK.

Duffie, J.A. & Beckman, W.A., 2013. Solar Engineering of Thermal Processes. 4th ed. New York: Wiley.

Energy Information Administration, 2013. International Energy Outlook 2013. U.S. Department of Energy.

Govind, Rashmi, Bansal, N.K. & Goyal, I.C., 1987. An experimental and theoretical study of a plastic film solar greenhouse. Energy Conversion and Management, 27(4), 395-400.

Gupta, A. & Tiwari, G.N., 2002. Computer model and its validation for prediction of storage effect of water mass in a greenhouse: a transient analysis. Energy Conversion and Management, 43, 2625–2640.

Hottel, H.C. & Sarofim A .F., 1967. Radiative transfer. McGraw-Hill.

Kaushik, S.C. & Kaul, S., 1989. Thermal comfort in buildings through a mixed water-mass thermal storage wall. Building and Environment, 24, 199-207.

Li, R., Dai, Y.J. & Wang, R.Z., 2015. Experimental and theoretical analysis on thermal performance of solar thermal curtain wall in building envelope. Energy and Buildings, 87, 324–334.

Mao, Y., Lei, C. & Patterson, J., 2007. Natural convection in a triangular enclosure induced by solar radiation. In 16th Australasian Fluid Mechanics Conference. Gold Coast, Australia, 2007.

Mirsadeghi, M., Cóstola, D., Blocken, B. & Hensen, J.L.M., 2013. Review of external convective heat transfer coefficient models in building energy simulation programs: Implementation and uncertainty. Applied Thermal Engineering, 56, 134-151.

Nayak, J.K., 1987. Thermal performance of a water wall. Building and Environment, 22, 83-90.

Robinson, B. S., Chmielewski, N. E., Knox-Kelecy, A., Brehob, E. G., & Sharp, M. K., 2013. Heating season performance of a full-scale heat pipe assisted solar wall. Solar Energy, 87, 76-83.

Sodha, M.S., Bhardwaj, S.C. & Kaushik, S.C., 1981b. Thermal load leveling of heat flux through an insulated thermal storage water wall. Energy Research, 5, 155-163.

Sodha, M.S., Kaur, J. & Sawhney, R.L., 1992. Effect of storage on thermal performance of a building. International Journal of Energy Research, 16(8), 697-707.

The Engineering Toolbox. [Online] Available at: http://www.engineeringtoolbox.com/ [Accessed 25 June 2015].

Tiwari, G.N., 1991. Design of a non-airconditioned passive solar house for the cold climate of Srinagar. Building and Environment, 26, 371-380.

Tiwari, G.N., Singh, A.K., 1996. Comparative studies of different heating techniques of a non-air conditioned building. Building and Environment, 31, 215-224.

Wu, T. & Lei, C., 2015. On numerical modelling of conjugate turbulent natural convection and radiation in a differentially heated cavity. International Journal of Heat and Mass Transfer, 91, 454-466.

4. CFD Simulation of the Thermal Performance of an Opaque Water Wall System for Australian Climate

Statement of contribution to co-authored manuscript

This chapter is based on a co-authored manuscript. The details of the manuscript, including all authors, are:

Wu, T. & Lei, C. CFD Simulation of the thermal performance of an opaque water wall system for Australian climate. *Solar Energy*, revision under review.

My contribution to the paper included conducting the literature survey, building and implementing the CFD model, collecting and analysing the simulated data, and drafting the paper.

Signed: _____ Date: _09.03.2016_____

Ting Wu

Countersigned: _____ Date: _10/03/2016_____

Co-author: A/Prof. Chengwang Lei (Supervisor, School of Civil Engineering, The University of Sydney)

4.1 Introduction

Over the last several decades, passive solar technologies have attracted growing research interests due to increasing energy consumption by residential and commercial buildings. In this regard, water wall offers an excellent solution which can maintain thermal comfort in buildings while reducing energy consumption in low to medium latitude countries. Based on the transmission of solar radiation in the system, water walls can be generally classified into two categories, i.e. opaque water walls and semi-transparent water walls. Both types of water wall systems have unique advantages over other passive strategies as they have relatively large heat capacities and cost significantly less than thermal energy storage walls using phase change materials (PCMs). Further, heat stored in water may be redistributed by convection, and thus a water wall provides much quicker heat exchange than a concrete or brick wall.

A large body of literature exists on analytical investigations of the thermal performance of opaque water walls. Balcomb & McFarland (1978) applied a simple empirical method called Solar Load Ratio Method to estimate the thermal performance of a Trombe wall and a water wall with or without night-time insulation and with or without a reflector. Their results showed that the water wall achieved a higher monthly solar heating fraction (i.e. the percentage of the space heating load supplied by the passive solar system) than that of the Trombe wall. They further carried out a parametric analysis of the annual energy savings using the above-described Trombe wall and water wall (McFarland & Balcomb, 1979). The parameters considered in their analysis included the R-value of the night-time insulation, the wall absorptivity and emissivity, the thermal storage capacity, and the additional building mass etc. They found that the performance of the water wall was enhanced by decreasing the R-value of the night-time insulation and the wall absorptivity and by increasing the wall emissivity, the thermal storage capacity and the additional building mass.

Nayak et al. (1983) compared the thermal performance of four typical passive heating concepts, namely a Trombe wall, a water wall and a solarium under two different configurations, one with the glazing uncovered and the other with the glazing covered by a moveable insulation during off sunshine hours. They developed a heat balance model (HBM), which is based on the energy conservation concept, to establish an energy balance associated with conductive, convective and radiative heat transfer in order to obtain surface and fluid (i.e. water and air) temperatures. Their calculations illustrated that the water wall system resulted in less temperature fluctuation and a higher average heat flux than the Trombe wall when night-time insulation was used, and a phase shift of almost 12 hour was observed for a 0.22-m thick

concrete wall next to a 0.10-m thick water wall. The HBM has been widely adopted over the past three decades, for example, by Dutt et al. (1987), Kaushik & Kaul (1989), Sodha et al. (1992) and Gupta & Tiwari (2002).

Recently, the HBM has also been applied to investigate the thermal performance of water wall with PCMs. Albanese et al. (2012) carried out a bench-scale experiment in order to verify the HBM for a passive solar space heating system utilising heat pipes to transfer latent heat to a storage water tank inside a building. It was found that the solar heat pipe system gave a significantly higher solar heating fraction than other passive technologies, especially in cold and cloudy climates, and a good agreement was obtained between the HBM and the laboratory experiment. In order to further validate the above-described HBM and the bench-scale experiment, a full-scale prototype of the heat pipe system was designed by Robinson et al. (2013) in a classroom at the University of Louisville during the spring heating season of 2010. During that season, the maximum hourly average heat gain was only 163 W/m^2. Their field results indicated that the thermal storage water tank was heated to a sufficiently high temperature to supply heat to the classroom even during the coldest days of the season. It was reported that, over a long period (4 consecutive days) of low solar isolation, the average hourly heat delivery to the classroom remained positive and was never less than 16.6 W/m^2. Again, a good agreement between the HBM prediction and field data of full-scale prototype was achieved. During January to February of 2013, an improved design of the passive heat pipe system was tested alongside the previous HBM and full-scale prototype by Robinson & Sharp (2014). Significant improvement in increasing heat transfer to the classroom and reducing heat losses was achieved by adding a copper absorber, a thicker insulation, a rubber adiabatic section and exposing one condenser directly to the room air.

Whilst the thermal performance of water wall systems has been investigated extensively using the HBM approach, computational fluid dynamics (CFD) modelling of water wall systems has attracted little attention due to the high cost involved in CFD. Among the existing CFD studies, Karabay et al. (2013) studied the thermal performance of a concrete wall with embedded water pipes filled with constant-temperature water. The model was two-dimensional (2D) and the flow was assumed to be turbulent. The simulations were performed for steady state conditions only. Moustafa & Aripin (2014) evaluated the thermal performance of a combined water wall and porous ceramic pipes system for evaporative cooling in a three-dimensional (3D) model. In their numerical model, the flow was assumed to be laminar, and the simulations were again performed for steady state conditions only.

It is seen from the above literature survey that the HBM has dominated the water wall research for over three decades, whereas the application of the CFD approach to water wall research is very limited. Although CFD is a powerful numerical approach, which can resolve complex fluid flow and heat and mass transfer processes and has been widely adopted to solve various scientific and engineering problems, its application to water wall research has been limited to steady state conditions only. The purpose of the present investigation is to develop a transient CFD model, accounting for time variations of solar radiation and ambient temperature, to evaluate the thermal performance of an opaque water wall system for typical climate conditions in Sydney, Australia, which are relevant to similar climate conditions in other low to medium latitude countries. The performance of the water wall system will also be compared with that of a conventional concrete wall model under different climate conditions.

4.2 Numerical Method and Tests

4.2.1 Model Formulation

Under consideration are a 2D opaque water wall and a 2D concrete wall, both being directly attached to an uncontrolled room and a controlled room (see Fig. 4.1). The water wall consists of two Perspex panels and a water column (refer to Fig. 4.1a), whereas the concrete wall comprises a pure concrete slab (refer to Fig. 4.1b). The outside Perspex panel of the water wall system is painted black to absorb solar radiation. The uncontrolled rooms are filled with air and the dimensions of the uncontrolled rooms are fixed at $D = H = 3$m, which resemble a typical residential space. The controlled rooms are kept at a constant temperature to resemble a heated space in winter or an air-conditioned room in summer. The surface between the controlled and uncontrolled rooms is referred to as Controlled Surface CS (refer to Fig. 4.1), where the heat flux will be evaluated. Since Surface CS is an ideal surface for numerical simulation, its thermal mass is neglected. The thickness of the Perspex panel (δ_p) is kept constant, whereas the thickness of the water column (δ_w) is varied in this study in order to investigate its effect on the thermal performance of the water wall system. The thickness of the concrete slab (δ_c) is the same as that of the water column. In this study, the computational domain covers the water wall or concrete wall and the uncontrolled room only.
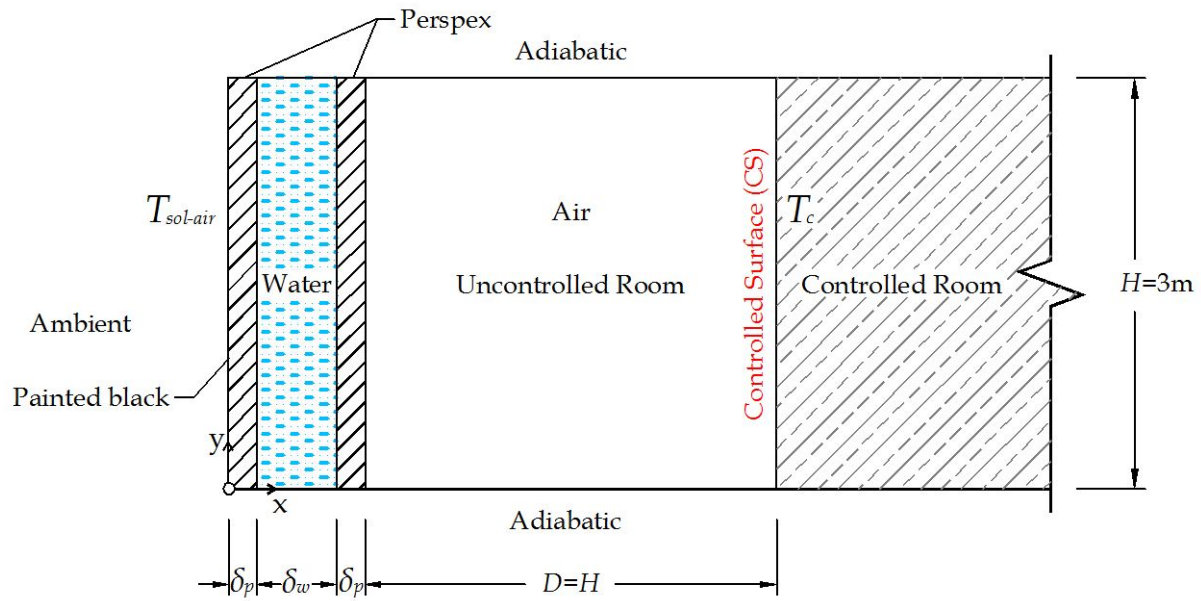
(a) Water wall model
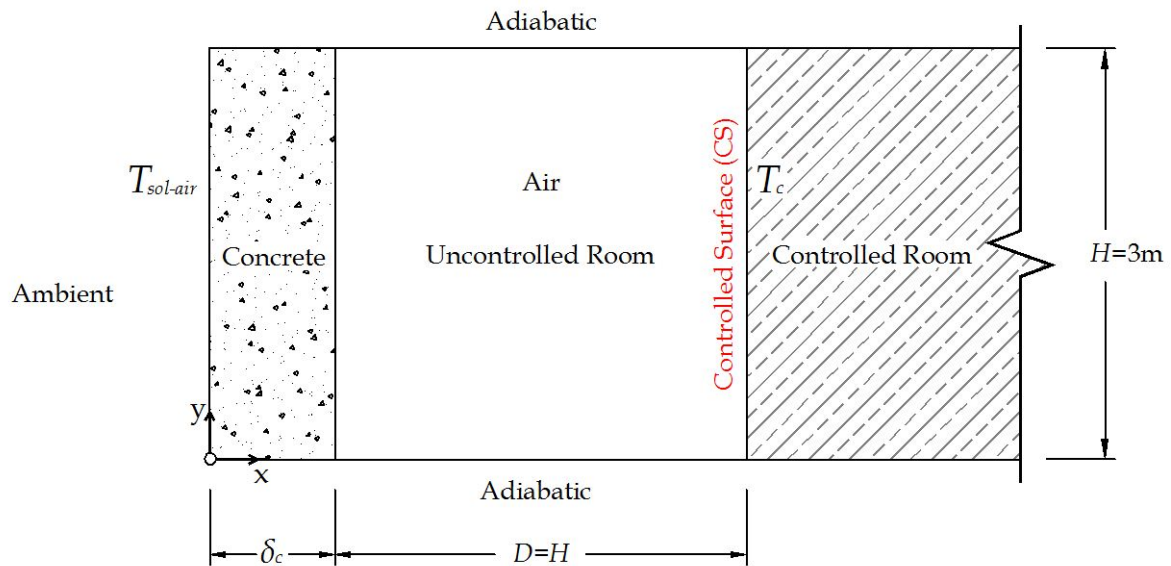
(b) Concrete wall model

Fig. 4.1 Schematic of two-dimensional (a) opaque water wall and (b) concrete wall models.

4.2.2 Boundary Conditions

In order to account for the effect of solar radiation on the outside Perspex panel or concrete panel, sol-air temperature (refer to O'Callaghan and Probert, 1977) is specified on the external surface of the outside Perspex panel or concrete panel in the present study. The calculation of the sol-air temperature, which is the same as that applied in Yumrutaş et al. (2007) and Ruivo et al. (2013), is as follows:

$$T_{sol-air}(t) = T_a(t) + \frac{\alpha I(t) - \varepsilon \Delta R}{h_0} \qquad (4.1)$$

where $T_{sol-air}(t)$ and $T_a(t)$ are instantaneous sol-air temperature and ambient temperature respectively at the time instant t; $I(t)$ is the incident total solar radiation on the external surface of the outside Perspex panel or concrete panel; α and ε are the absorptivity and emissivity of the external surface; h_0 is the heat transfer coefficient between the external surface and the ambient; and ΔR is the difference between the long-wave radiation from the sky incident on the external surface and the radiation emitted by the external surface. In practice, $\Delta R = 0$ for vertical surfaces (Yumrutaş et al. 2007). Here, the external heat transfer coefficient h_0 is evaluated using the following expression (ASHRAE, 1975):

$$h_0 = 18.6 V_{loc}^{0.605} \qquad (4.2)$$

where V_{loc} is given by:

$$V_{loc} = \begin{cases} 0.5 \text{ m/s} & \text{for } V_{10} < 2\text{m/s} \\ 0.25 V_{10} & \text{else} \end{cases} \qquad (4.3)$$

Here V_{10} is the wind speed measured at a weather station 10 m above the ground (m/s).

In order to simulate the effect of the diurnal temperature variation for typical Sydney climate, a sinusoidal function of the ambient temperature is defined as:

$$T_a(t) = T_0 + \frac{\Delta T}{2} \sin[2\pi(t - t_{lag})/P] \qquad (4.4)$$

where P is the period of the thermal cycle, which is 24 hours in this study; T_0 is the mean ambient temperature over one thermal cycle; ΔT is the difference between the maximum and minimum temperatures over one thermal cycle; and t_{lag} is the time lag of the ambient temperature change relative to the change of solar radiation, which is set to 2 hours in this study, indicating that the daily maximum ambient temperature appears 2 hours after the incident solar radiation peaks. In real life situations, the daily minimum ambient temperature usually occurs at approximately one hour before sunrise, which does vary slightly throughout the year. In order to simplify the numerical model, a fixed time lag between the ambient temperature variation and the solar radiation is assumed. It is anticipated that the relatively small variation of the occurring time of the daily minimum ambient temperature relative to solar radiation will not significantly affect the numerical results presented here and the major conclusions drawn upon them.

The incident total solar radiation on the external surface is calculated as follows:

$$I(t) = \begin{cases} I_{max} \sin(2\pi t/P) & \text{for } (m-1)P < t \le \left(m - \frac{1}{2}\right)P \\ 0 & \text{for } \left(m - \frac{1}{2}\right)P < t \le mP \end{cases} \qquad (4.5)$$

where I_{max} is the maximum solar radiation over one thermal cycle; and m is the number of the thermal cycle.

Apart from the external surface, Surface CS is kept at a constant temperature, whereas the top and bottom surfaces are assumed adiabatic. All the other internal surfaces are coupled between solid and fluid.

Under the above boundary conditions, the temperature of the outside Perspex panel in the water wall system rises during the day and heat is transferred to the adjacent water column due to heat conduction through the Perspex panel. A convective flow is then induced by buoyancy in the water column, and heat is quickly transferred to the inside Perspex panel in addition to that stored in the water column. Subsequently, heat is further transferred from the inside Perspex panel to the adjacent air. As a consequence, the uncontrolled room air is heated up. At night, the heat transfer process may be reversed due to the absence of solar radiation, and the temperatures of the outside Perspex panel, the water column and the room air may decrease dramatically due to the drop of the outside temperature. When the sun rises in the next day, the outside Perspex panel is being heated again, and a new thermal cycle starts. The heat transfer processes involved in the concrete wall system are similar to those in the water wall system except for that the water wall is replaced by an opaque concrete wall. Clearly convection takes place in both the water column and the air space (the uncontrolled room) in the water wall system, but occurs only in the air space in the concrete wall system.

The convective flows inside the present 2D water wall model and concrete wall model can be characterized by the Rayleigh number, the Prandtl number and the aspect ratio, which are defined as follows:

$$Ra_f = \frac{g\beta_f \Delta T H^3}{\nu_f \kappa_f}, \; Pr_f = \frac{\nu_f}{\kappa_f}, \; A_f = \frac{H}{\delta_f} \tag{4.6}$$

where the subscript f denotes the type of fluid (i.e. 'w' for water and 'a' for air); g is the acceleration due to gravity; ν_f, κ_f and β_f are the kinematic viscosity, thermal diffusivity and thermal expansion coefficient of the working fluid at the reference temperature T_0; δ_f is the thickness of the working fluid (δ_w for water and D for air); and ΔT is the temperature difference between the maximum and minimum sol-air temperatures over a diurnal cycle. Here the nominal Rayleigh numbers are fixed at $Ra_w = 2.1 \times 10^{13}$ for water and $Ra_a = 1.52 \times 10^{12}$ for air, and the water and air flows are assumed to be turbulent. The Prandtl numbers are fixed at $Pr_w = 7$ for water and $Pr_a = 0.71$ for air respectively. The aspect ratio of the room is fixed at $A_a = 1$, whereas the aspect ratio of the water column A_w is a control parameter in the present study.

4.2.3 Governing Equations

The buoyancy-induced turbulent water and air flows are governed by the following unsteady Reynolds Averaged Navier-Stokes and energy equations with Boussinesq assumption:

$$\frac{\partial u_i}{\partial x_i} = 0 \tag{4.7}$$

$$\frac{\partial u_i}{\partial t} + \frac{\partial (u_i u_j)}{\partial x_j} = -\frac{1}{\rho_f}\frac{\partial p}{\partial x_i} + \frac{1}{\rho_f}\frac{\partial}{\partial x_j}\left[\mu_f\left(\frac{\partial u_i}{\partial x_j} + \frac{\partial u_j}{\partial x_i}\right) - \rho_f\overline{u_i'u_j'}\right] - g_i\beta_f(T - T_0) \tag{4.8}$$

$$\frac{\partial T}{\partial t} + \frac{\partial (u_j T)}{\partial x_j} = \frac{1}{\rho_f}\frac{\partial}{\partial x_j}\left[\frac{\lambda_f}{C_{p_f}}\frac{\partial T}{\partial x_j} - \rho_f\overline{u_i'T'}\right] \tag{4.9}$$

where x_i and x_j are the Cartesian coordinates in the i and j directions (i, j = 1 and 2 corresponding to the x and y directions respectively); t is the time; p is the pressure; T and T' are the mean and fluctuating temperatures; u_i and u_j are the mean velocity components in the i and j directions; u'_i and u'_j are the corresponding fluctuating velocity components in the i and j directions; and ρ_f, λ_f, C_{pf} and μ_f are the fluid density, thermal conductivity, specific heat and dynamic viscosity, respectively.

4.2.4 Turbulence Models

In order to close Equations (4.7)-(4.9), the Reynolds stresses $(-\rho_f\overline{u_i'u_j'})$ and the turbulence heat fluxes $(\overline{u_i'T'})$ must be modelled. Different turbulence models have different treatments of the Reynolds stresses and the turbulence heat fluxes. In this study, the shear-stress transport (SST) k-ω model is adopted due to its accuracy for a related problem demonstrated in a previous investigation (Wu & Lei, 2015a). In the SST k-ω model, the Reynolds stresses are modelled through the Boussinesq approximation as:

$$-\rho_f\overline{u_i'u_j'} = \mu_t\left(\frac{\partial u_i}{\partial x_j} + \frac{\partial u_j}{\partial x_i}\right) - \frac{2}{3}\rho_f k\delta_{ij} \tag{4.10}$$

where μ_t is the turbulent eddy viscosity; k is the turbulent kinetic energy; and δ_{ij} is the Kronecker delta (δ_{ij} = 0 if $i{\neq}j$ and δ_{ij} = 1 if $i{=}j$). The turbulent eddy viscosity is computed from:

$$\mu_t = \frac{\rho_f k}{\omega}\frac{1}{\max\left[\frac{1}{\alpha^*},\frac{SF_2}{\alpha_1\omega}\right]} \tag{4.11}$$

where ω is the specific dissipation rate; α_1 = 0.31; and α^* is a coefficient used to predict transition from laminar to turbulent flow (α^* = 1 in fully turbulent flows) (Wilcox, 1998). F_2

is a coefficient computed from an additional equation and S is the modulus of the mean rate-of-strain tensor which is defined as:

$$S = \sqrt{2S_{ij}S_{ij}} \tag{4.12}$$

where S_{ij} is the mean rate of strain tensor and is given by:

$$S_{ij} = \frac{1}{2}\left(\frac{\partial u_i}{\partial x_j} + \frac{\partial u_j}{\partial x_i}\right) \tag{4.13}$$

More details about the SST k-ω model can be found in Menter (1994).

The turbulence heat fluxes are modelled as:

$$\overline{u_i'T'} = -\frac{\mu_t}{\rho_f \sigma_T}\frac{\partial T}{\partial x_i} \tag{4.14}$$

where σ_T is the turbulent Prandtl number, which is equal to 0.85. In the SST k-ω model, two additional transport equations (one for the turbulence kinetic energy (k), and the other for the specific dissipation rate (ω)) are solved. Further details of the SST k-ω model can be found in ANSYS FLUENT User's Guide (Fluent Inc., 2011).

4.2.5 Radiation Models

Among all the radiation models available in ANSYS FLUENT 14.0, the Discrete Ordinates (DO) radiation model is the only model that can deal with radiation problems with both participating and non-participating media. Since water is a participating media, the DO radiation model is adopted. In the DO radiation model, the directional variation of the radiative intensity is represented by a discrete number of ordinates, and integrals over solid angles are approximated by numerical quadrature (Modest, 2013). The radiative transfer equation is solved for a finite number of discrete solid angles for as many transport equations as there are in an associated vector direction at spatial location (x, y). The equation used in the DO model is written as:

$$\nabla \cdot (I(\vec{r}, \vec{s})\vec{s}) + (a + \sigma_s)I(\vec{r}, \vec{s}) = an^2\frac{\sigma T^4}{\pi} + \frac{\sigma_s}{4\pi}\int_0^{4\pi} I(\vec{r}, \vec{s}')\Phi(\vec{s} \cdot \vec{s}')\,d\Omega' \tag{4.15}$$

where $\vec{r}$, $\vec{s}$, and $\vec{s}'$ are the position vector, the direction vector and the scattering direction vector respectively; a and σ_s are the absorption coefficient and the scattering coefficient; n is the refractive index; σ is the Stefan-Boltzmann constant (5.669×10^{-8} W/m^2-K^4); I is the radiation intensity, which depends on the position ($\vec{r}$) and direction ($\vec{s}$); and T, Φ, and Ω' are the local temperature, the phase function and the solid angle respectively.

4.2.6 Numerical Scheme

The governing equations including the two additional transport equations for the turbulence kinetic energy (k) and the specific dissipation rate (ω) along with the specified boundary and initial conditions are solved using the CFD package ANSYS FLUENT 14.0, which is a finite-volume based solver. The pressure-velocity coupling is carried out using the SIMPLE scheme. The advection terms in the governing equations are discretised by a second-order upwind scheme and the diffusion terms are discretised using a second-order central-differencing scheme. A second-order implicit time-marching scheme is adopted for the unsteady term.

4.2.7 Grid and Time-Step Dependency Tests

Grid and time-step dependency tests have been conducted based on a case with the thickness of the water column δ_w = 0.15m under a constant cooling condition. In this case, Surface CS is maintained at a constant temperature T_h = 22°C (corresponding to a heated space), and the outside Perspex panel is kept at a constant temperature T_p = 3°C (corresponding to a cold weather condition in winter). Initially, the fluid and solid temperatures in the model are set to $T_0 = (T_h + T_p)/2 = 12.5^o$C, and the water and air are assumed to be stationary. For the grid dependency test, three different non-uniform meshes 60 × 78, 100 × 130 and 200 × 260 with a fixed time-step of 0.5s are calculated for 12 hours. Since the energy efficiency of the water wall system may be ascertained by the heat flux through Surface CS, this heat flux is calculated for comparison. The time series of the heat flux obtained with the three meshes are shown in Fig. 4.2a. The negative heat fluxes over the time period of 12 hours indicate that heat continuously flows from the controlled room to the uncontrolled room, which is expected. It can be seen in this figure that the results obtained with the two finer meshes produce very similar results, whereas the coarsest mesh produces a discernible variation.
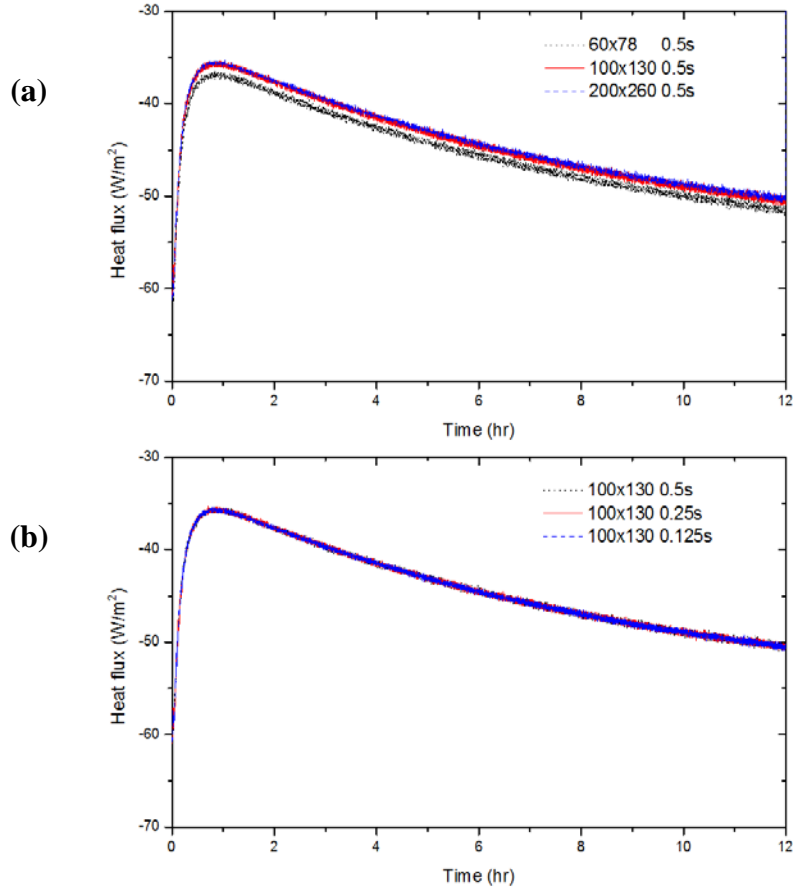
Fig. 4.2 Time history of the predicted heat flux through Surface CS with (a) different meshes and (b) different time-steps.

A quantitative comparison of the results obtained with these three meshes is shown in Table 4.1. Here, $q_{ref,max} = -35.336 \, \text{W/m}^2$ and $\overline{q_{ref}} = -44.077 \, \text{W/m}^2$ are the maximum and average heat fluxes through Surface CS respectively over the time period of 12 hours obtained in the reference case (Case 1) with the 100×130 mesh and the 0.5s time-step. $q_{max} - q_{ref,max}$ represents the variation of the maximum heat fluxes between a test case and the reference case, and $\overline{q} - \overline{q_{ref}}$ is the variation of the average heat fluxes between a test case and the reference case. The comparison of Cases 1, 2 and 3 in Table 4.1 demonstrates that the $100 \times$ 130 mesh is capable of producing a sufficiently accurate solution. The medium mesh, i.e. $100 \times$ 130, is therefore adopted for subsequent calculations in consideration of computing costs.

Table 4.1 Comparisons of the statistical results of the predicted heat flux through Surface CS with different meshes and time-steps.

Case no.	Mesh	Time-step (s)	$\dfrac{q_{max} - q_{ref,max}}{q_{ref,max}}$ (%)	$\dfrac{\overline{q} - \overline{q_{ref}}}{\overline{q_{ref}}}$ (%)
1	100×130	0.5	0	0
2	60×78	0.5	2.72	2.46
3	200×260	0.5	-0.19	-0.42
4	100×130	0.25	-0.10	-0.01
5	100×130	0.125	-0.08	-0.01

Following the above mesh dependence test, three time-steps of 0.5s, 0.25s and 0.125s respectively with the 100×130 mesh are tested for the same water wall model. The heat fluxes through the same monitoring surface obtained with these three time-steps are shown in Fig. 4.2b. It is observed in this figure that the results obtained with the different time-steps are almost identical. A quantitative comparison of the heat fluxes calculated in Cases 1, 4 and 5 with different time-steps is given in Table 4.1, which confirms that the variations of the results are indeed negligible. In consideration of the numerical accuracy and the computational time, the 100×130 mesh and the 0.5s time-step are selected for the present model. Similarly, a mesh and time-step dependency test for the concrete wall model shows that a 100×130 mesh and a 0.5s time-step provide sufficient spatial and temporal resolutions for the concrete wall system, and thus are adopted in this study.

4.3 Results and Discussions

The following subsections present the numerical results obtained from 2D unsteady turbulent simulations using the SST k-ω model and the DO radiation model for the above-described water wall and concrete wall models with periodic sol-air temperature variations on the external surfaces. In Section 4.3.1, the present CFD model of a water wall system is compared with an experimentally validated transient heat balance model (THBM), and the thermal stratification in the water column and in the uncontrolled room air is demonstrated. In Section 4.3.2, the thermal performance of the water wall system is described in terms of the water and uncontrolled room air temperatures as well as the heat fluxes through Surface CS. A parametric study is also presented to illustrate the effect of the thickness of the water column on the thermal stratifications in water and air, the temperature fluctuation in the uncontrolled room and the

supplemental energy consumption of the controlled room. In Section 4.3.3, quantitative analyses are performed to investigate the thermal response to different sol-air temperature variations, which resemble typical winter and summer climate conditions. A comparison is also made between the water wall model and a concrete wall model to illustrate the advantages of the water wall system.

4.3.1 Validation of the CFD Model against the THBM

The above-described CFD model for the opaque water wall system is validated here using a transient heat balance model (Wu & Lei, 2015b), which has been validated against experimental measurements. In the THBM, the time variations of internal convective heat transfer coefficients, the radiation emitted by external surfaces and the internal surface radiation exchanges are all accounted for. Details of the THBM and its validation can be found in Wu & Lei (2015b).

The comparison of the CFD model and the THBM is carried out with the thickness of the water column δ_w fixed at 0.15m. The mean daily ambient temperature T_0 and the maximum daily solar radiation of the outside Perspex panel I_{max} are fixed at 12.5°C and 800 W/m^2 respectively, which resemble a typical winter climate condition in Sydney, Australia. The difference between the daily maximum and minimum ambient temperatures ΔT_a is set to 15°C, whereas the wind speed is assumed to be 3.944 m/s according to the statistical climate data for Sydney in July. Surface CS is maintained at $T_c = 22^{\circ}$C which resembles a typical heated space in winter. The water and air within the computational domain is initially stationary with a uniform temperature T_0. The simulations of both the CFD model and the THBM have been conducted over seven thermal cycles (days), which begins at 6am in Day 1.
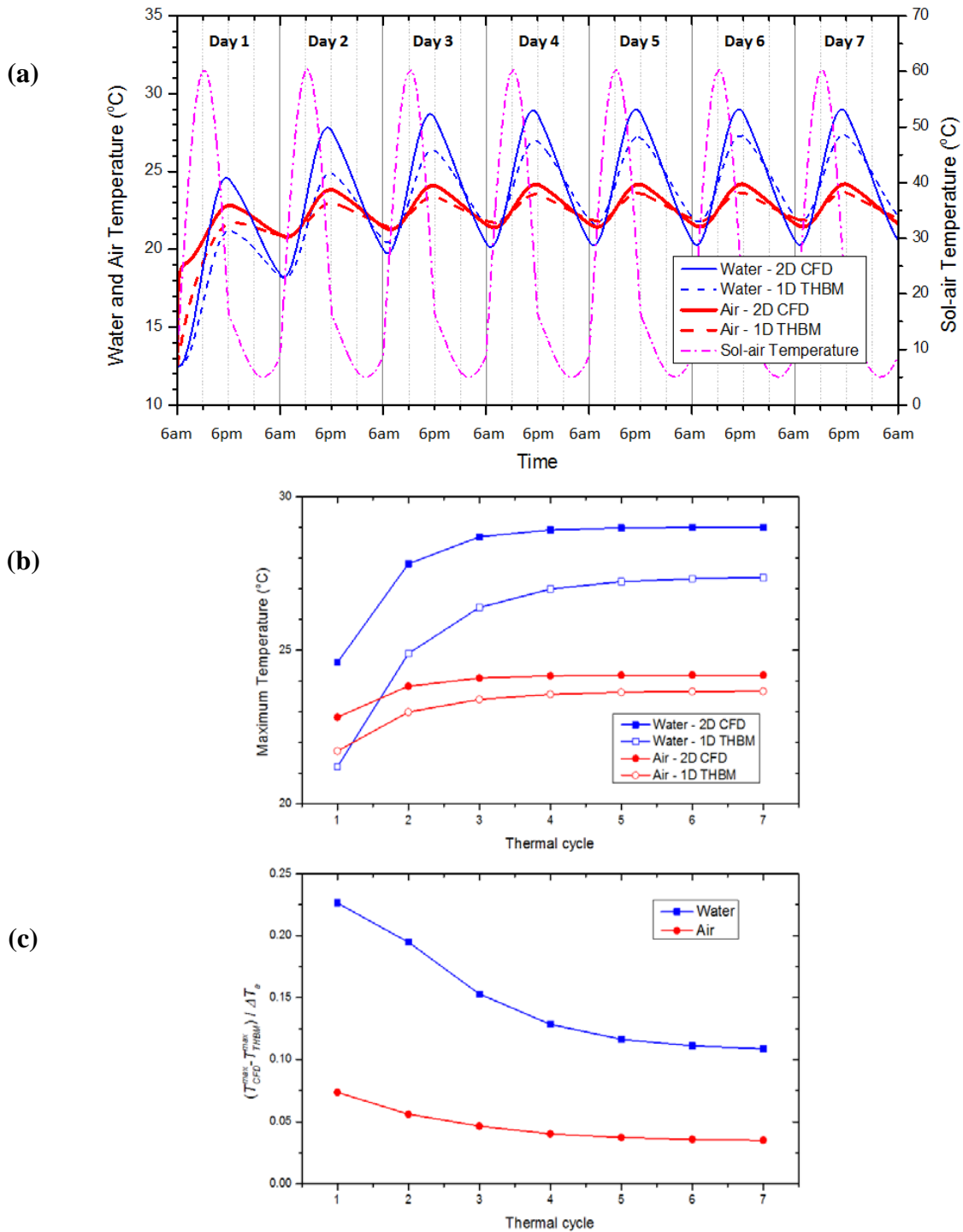
Fig. 4.3 Comparisons of the 2D CFD model and the 1D THBM. (a) Time series of predicted water and air temperatures; (b) Time series of predicted maximum water and air temperatures; and (c) Variations of the differences between the CFD model and the THBM in the predicted daily maximum water and air temperatures.

Fig. 4.3a shows the time series of the averaged water and room air temperatures in the 2D CFD model and the predicted water and air temperatures by the one-dimensional (1D) THBM.

Here the average temperatures of the water column and the room air in the CFD model are evaluated as:

$$\overline{T_w} = \frac{1}{\delta_w H} \int_0^H \int_{\delta_p}^{\delta_p + \delta_w} T_w dx dy \qquad (4.16)$$

$$\overline{T_a} = \frac{1}{DH} \int_0^H \int_{2\delta_p + \delta_w}^{2\delta_p + \delta_w + D} T_a dx dy \qquad (4.17)$$

It is seen in Fig. 4.3a that a generally good agreement between the CFD model and the THBM is achieved for the predicted water and air temperatures, with the difference in the predicted air temperatures much less than that of the water temperatures. It is also clear in Fig. 4.3a that the water temperature fluctuates over an approximate range of 20 to 30°C, which is significantly greater than that of the air temperature. The daily maximum temperatures in the water and air generally occur before 6pm, whereas the daily minimum temperatures in the water and air generally occur after 6am.

Since both the CFD and the THBM models start with stationary fluids and a uniform temperature in the water wall system, start-up effects of these models are evident in Fig. 4.3a. However, quasi-steady states are established in the CFD and THBM models after several thermal cycles. In order to quantify the start-up effect of the individual models, the time series of the daily maximum water and air temperatures are plotted in Fig. 4.3b. It is clear in this figure that both the daily maximum water and air temperatures converge quickly as the number of thermal cycle increases, with the CFD model converging slightly more quickly than the THBM. After 6 full thermal cycles, the variations of both the water and air temperatures become less than 0.5% in both models. It is therefore assumed that a quasi-steady state has been established in the water wall system after 6 thermal cycles.

Fig. 4.3c further displays the quantitative comparison of the maximum daily water and uncontrolled room air temperatures predicted by the CFD model and the THBM. It is seen in this figure that the differences between the CFD model and the THBM in the predicted maximum water and air temperatures both reduce with the increase of the thermal cycles, suggesting that the variations between the CFD model and the THBM are at least in part due to the start-up effects of the diurnal models. Unfortunately, extending the CFD simulations to more diurnal cycles is not feasible due to the constraints of available computing resources. In order to minimise the start-up effects and focus on the thermal performance of the water wall system at the quasi-steady state, only the data obtained in the last thermal cycle (i.e. in Day 7) are analysed and presented in what follows.
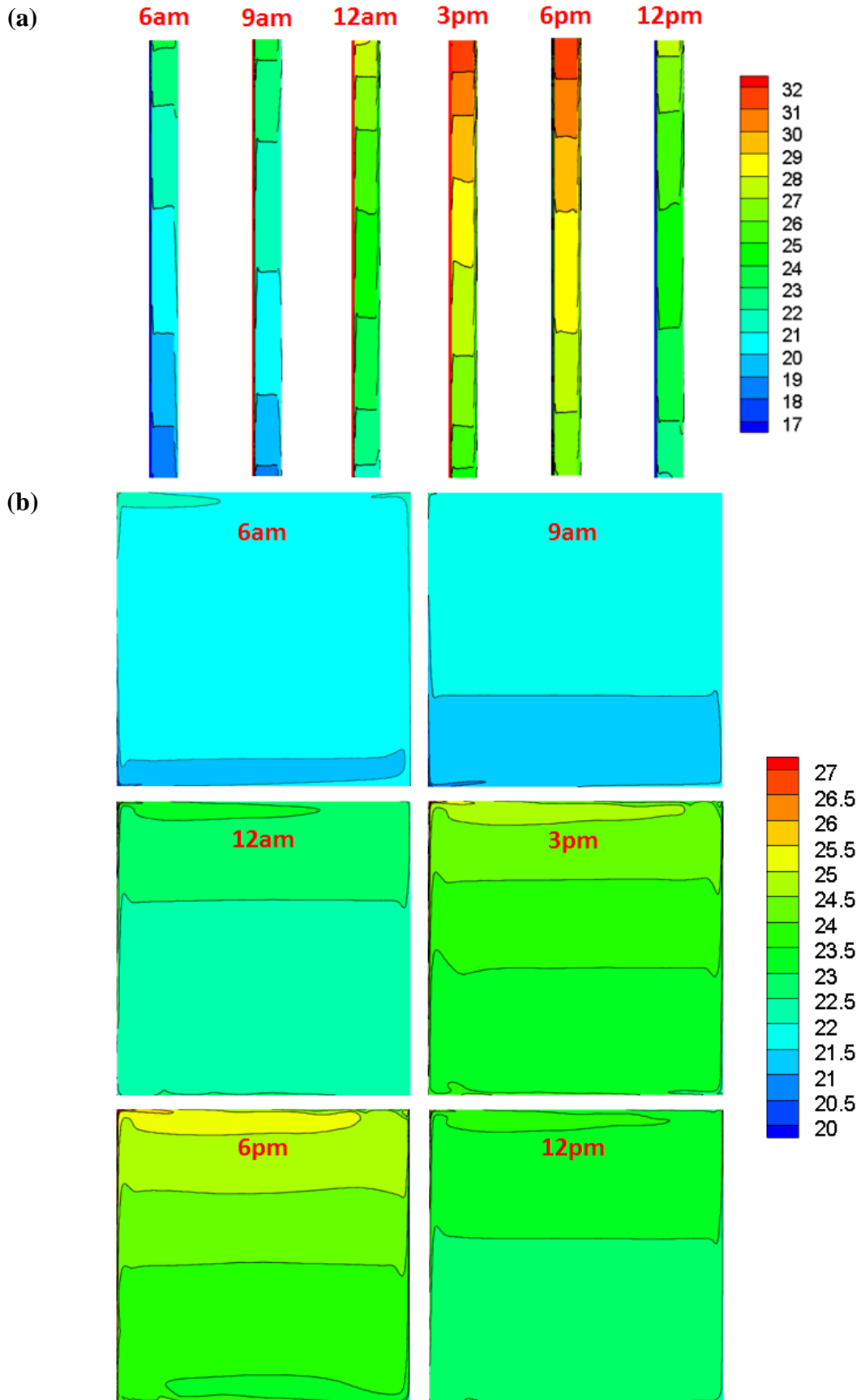
Fig. 4.4 Snapshots of isotherms in the (a) water column and (b) uncontrolled room air obtained with the water wall thickness $\delta_w = 0.15$m in Day 7 under the winter climate condition.

The variations between the CFD model and the THBM may also be attributed to the fact that the CFD model is 2D, whereas the THBM is only 1D. The effect of the horizontal boundaries is neglected in the 1D THBM, but is accounted for in the 2D CFD model. Since full-scale experiment is expensive to run and difficult to control under realistic climate conditions, the predicted results from the experimentally validated THBM provide an alternative way to validate the present CFD model. It is confirmed through the above comparisons that the present CFD model is capable of predicting the water and room air temperatures in the opaque water wall system to a reasonable level of accuracy, and thus will be adopted to explore the thermal performance of the opaque water wall system over a range of parameters.

Whilst the THBM can quickly predict the major features of a water wall system, it does not resolve the details of the convective flows pertinent to the water wall system due to the 1D nature of the model. In contrast, the CFD approach can resolve full details of the convective flows such as the thermal stratifications in the water column and air space. Snapshots of isotherms in the water column and uncontrolled room air obtained with the thickness of the water column $\delta_w = 0.15$m in the seventh thermal cycle under the winter climate condition are presented in Fig. 4.4. It is seen from the isotherms that the interior thermal stratifications are evident in both the water column and uncontrolled room air, although the strength of the temperature stratification in the water column is evidently stronger than that in the uncontrolled room air.

4.3.2 Effect of the Thickness of the Water Column

For comparison purpose, the thickness of the water column δ_w is varied from 0.075m to 0.3m in this study. All the boundary conditions remain the same as those described in Section 4.3.1. In order to quantify the temperature stratifications in the water column and in the uncontrolled room air, time series of the vertical temperature gradient (VTG) obtained with different water column thicknesses are plotted in Fig. 4.5. Here, the VTG is defined as:

$$\text{VTG} = \frac{(T_{2.5} - T_{o.5})/\Delta H}{\Delta T/H} \tag{4.18}$$

where $T_{2.5}$ and $T_{0.5}$ are the water or air temperatures extracted along the centre line at the heights of 2.5m and 0.5m in the water column or uncontrolled room, respectively. ΔH is the difference between the higher and lower points where the temperatures are extracted (i.e. ΔH = 2m in the present case). ΔT is the difference between the maximum and minimum ambient temperatures over one thermal cycle. The comparison of Figs. 4.5a and 4.5b confirms that the temperature stratification in the water column is indeed stronger than that in the uncontrolled

22room air. The former varies over the range of 0.05 ~ 0.1 for the different thicknesses of the water column, whereas the latter only varies over the range of 0.01 ~ 0.05. It is also noteworthy that the temperature stratifications of both water and uncontrolled room air decrease with the increase of the water column thickness.

(a)　　　　　　　　　　　　　(b)
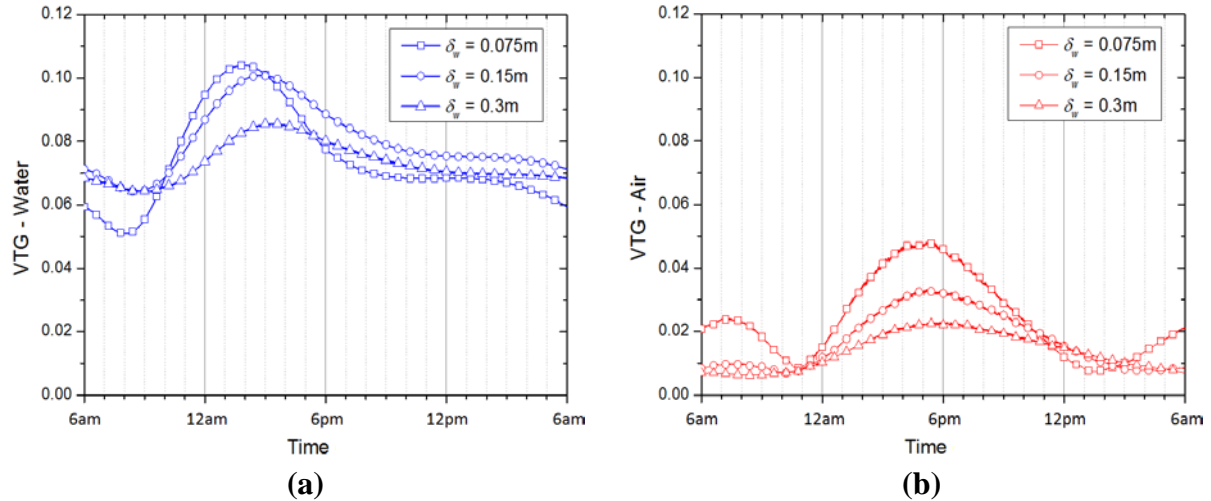
Fig. 4.5 Time series of vertical temperature gradient in (a) the water column and (b) the uncontrolled room air obtained with different water column thicknesses.

(a)　　　　　　　　　　　　　(b)
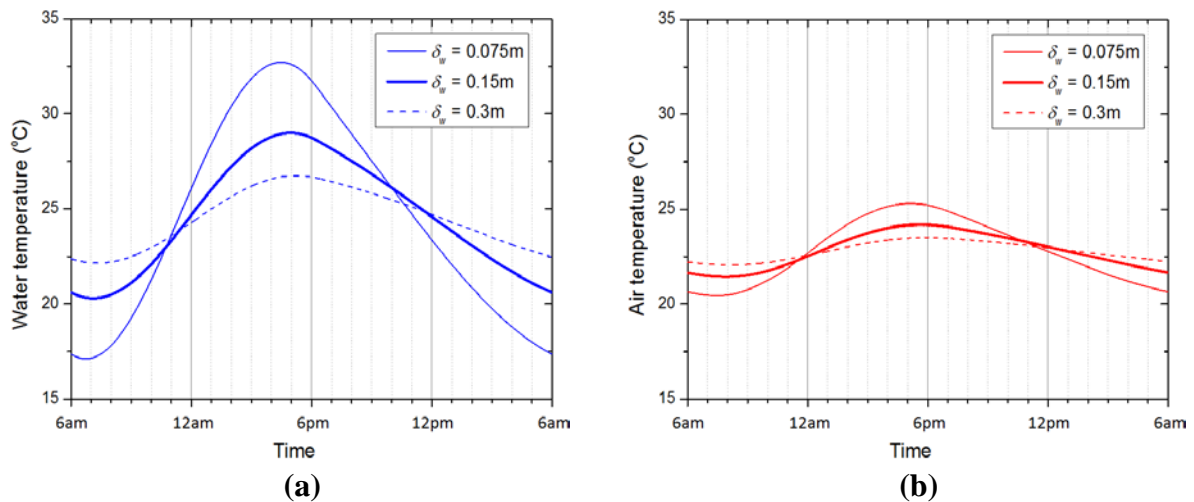
Fig. 4.6 Time series of the averaged (a) water and (b) uncontrolled room air temperatures obtained with different water column thicknesses.

Fig. 4.6 illustrates the time series of the average water and air temperatures obtained with different water column thicknesses under the winter climate condition. It is clear in Fig. 4.6 that the temperature fluctuations of both water and air reduce with the increase of the water column thickness, and the temperature fluctuation of water is much larger than that of air in the present opaque water wall system. This result along with the results shown in Figs. 4.3-4.5 demonstrates

111

that the water column acts as a buffer layer to mitigate temperature fluctuations in the uncontrolled room air.

Quantitative data indicating the temperature fluctuations in water and air obtained with different thicknesses are listed in Table 4.2. In this table, the temperature fluctuation index (TFI) is calculated as (Tiwari and Singh, 1996):

$$\text{TFI} = \frac{T_{max} - T_{min}}{T_{max} + T_{min}} \tag{4.19}$$

where T_{max} and T_{min} are the daily maximum and minimum averaged water or air temperatures, respectively. The results in Table 4.2 show that the temperature fluctuation of water is almost three times than that of uncontrolled room air for all the water column thickness considered.

Table 4.2 Comparisons of the temperature fluctuation index (TFI) of water and air obtained with different water column thicknesses.

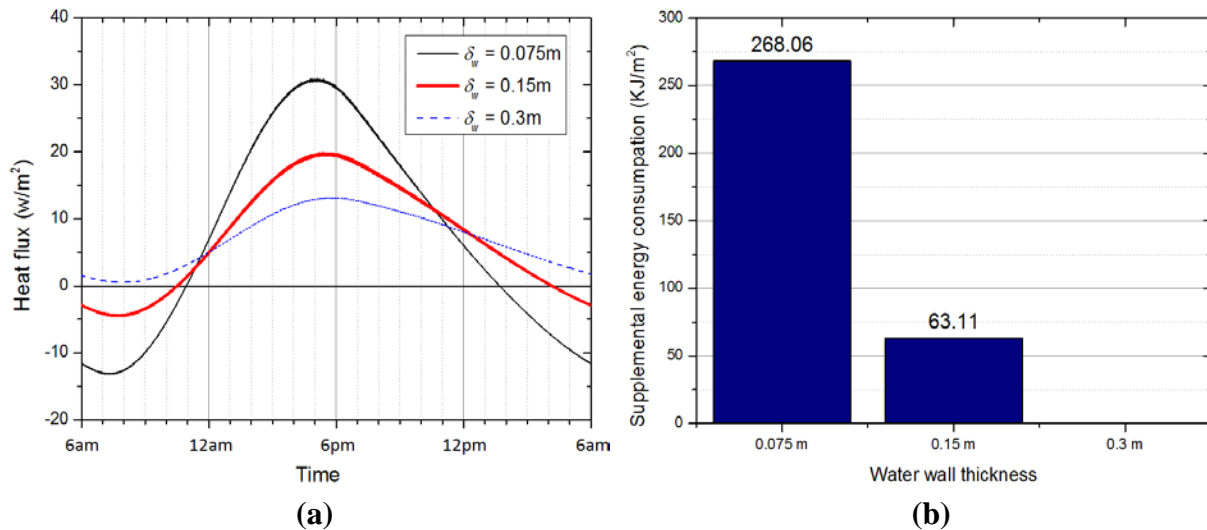| Water wall thickness δ_w (m)	Water	Air
0.075	0.313	0.106
0.15	0.177	0.060
0.3	0.094	0.032

Fig. 4.7 (a) Time series of the heat flux entering into the controlled room; (b) comparisons of supplemental energy consumptions for space heating with the different water column thicknesses.

For the purpose of exploring energy saving potential of various energy saving strategies, the heat flux to or from a temperature-regulated room has been examined in the literature (e.g.

112

Nayak et al., 1983; Kaushik and Kaul, 1989). Here the time series of the heat flux entering into the controlled room is presented in Fig. 4.7a for the different water column thicknesses. In this figure, a positive heat flux means that heat is transferred from the uncontrolled room to the controlled room, whereas a negative heat flux represents heat transfer in the opposite direction. It is found in Fig. 4.7a that both the heat fluxes entering into the controlled room and transferring out of the controlled room decrease with the increase of the water column thickness. This is because that an increase of the water column thickness results in a larger thermal energy storage capacity, and thus the heat transfer into and out of the controlled room becomes smaller. When the water column thickness is 0.3m, the heat flux is positive throughout the thermal cycle, suggesting that no supplemental energy is needed for space heating in the controlled room.

Fig. 4.7b presents the supplemental energy consumptions for heating the controlled room calculated with the different water column thicknesses. Here, the supplemental energy consumption is calculated as:

$$E = -\int_{t1}^{t2} q'' dt \quad \text{for } q'' < 0 \tag{4.20}$$

where q'' is the instantaneous heat flux from the uncontrolled room to the controlled room, and t_1 and t_2 are two time instants, over which period the supplemental energy consumption is integrated. As described above, the negative heat fluxes represent that the air temperature in the uncontrolled room is lower than that in the controlled room, and thus heat is supplied to the controlled room in order to maintain the constant temperature T_c. Fig. 4.7b indicates the supplemental energy consumptions decrease significantly with the increase of the water column thickness, and when the water column thickness is 0.3m, no supplemental energy for heating the space is required. Therefore, increasing the water column thickness of the present opaque water wall system can save a significant amount of supplemental energy for space heating in winter.

4.3.3 Comparison of Water Wall and Concrete Wall Models under Different Climate Conditions

In this section, the concrete wall model shown in Fig. 4.1b is compared with the opaque water wall model under two different climate conditions with both the thicknesses of the water column δ_w and the concrete slab δ_c fixed to 0.15m. One climate condition is the typical winter condition in Sydney, Australia described in Section 4.3.1, and the other climate condition is the typical summer condition in Sydney with a diurnal mean temperature of $T_0 = 27.5^{\circ}$C and the maximum solar radiation of $I_{max} = 1000$ W/m^2. For the summer condition, the difference between the daily maximum and minimum ambient temperatures is also set to $\Delta T = 15^{\circ}$C, whereas the wind speed

is assumed to be 3.681 m/s according to the statistical climate data for Sydney in January. Surface CS is maintained at T_c = 25°C, which is a typical temperature setting for an air-conditioned room in summer.
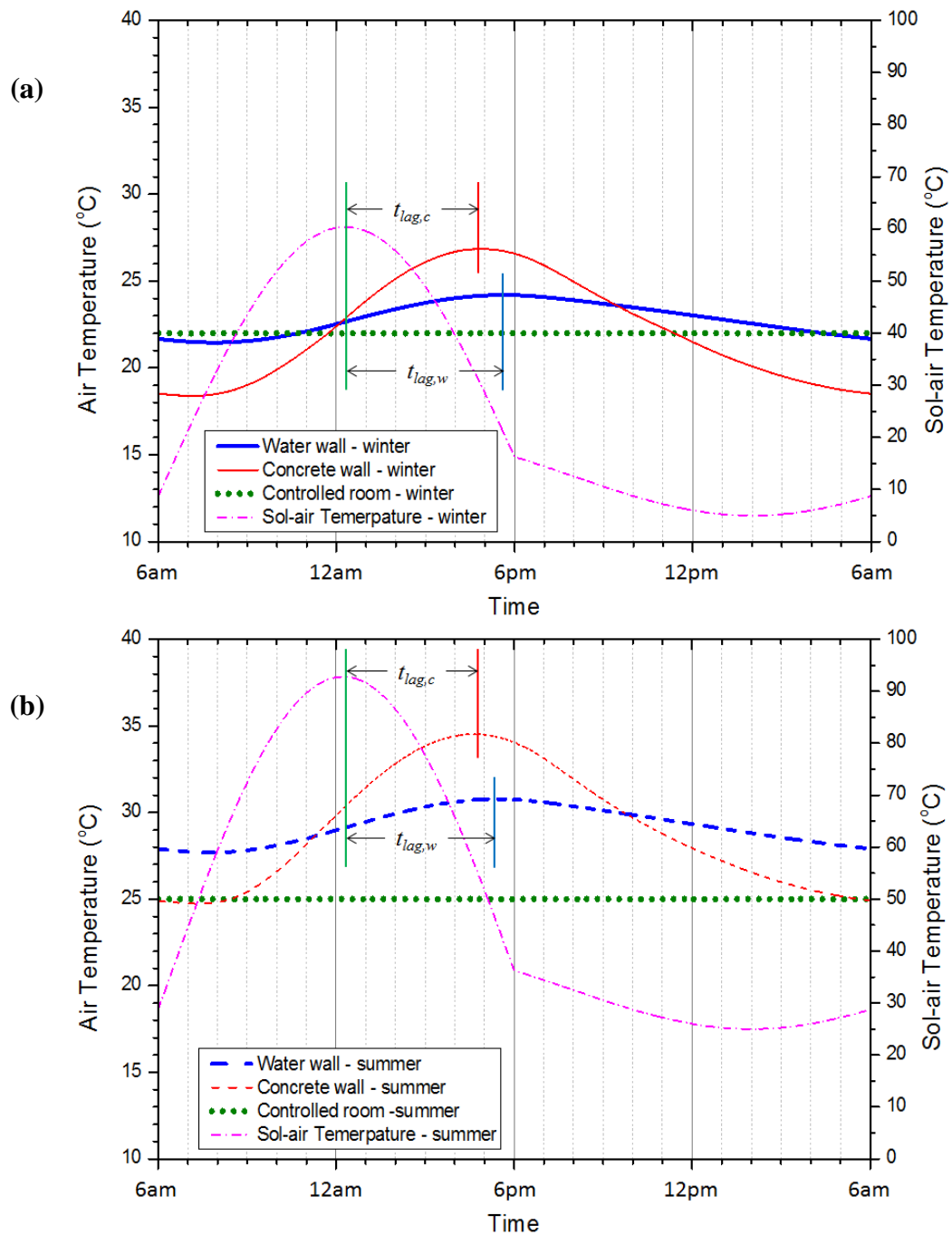
Fig. 4.8 Comparisons of the uncontrolled room air temperatures and the time lags in the water wall and concrete wall models under (a) winter and (b) summer climate conditions.

Fig. 4.8 presents the time series of the uncontrolled room air temperature in the water wall and concrete wall models under the winter and summer climate conditions respectively. It is worth noting that the start-up effect of the CFD model has also been tested for the

concrete wall system, and the results show that a quasi-steady state is achieved in the concrete wall system after only 2 full thermal cycles. The data presented in Fig. 4.8 for the concrete wall model is extracted from Day 7, which is consistent with that for the water wall model. It is clear in this figure that the uncontrolled room air temperature in the water wall model has a smaller fluctuation in both winter and summer than that in the concrete wall model. Under the winter condition (refer to Fig. 4.8a), the uncontrolled room air temperature is higher than the controlled room temperature for most of the time in the water wall model, whereas in the concrete wall model, the daily maximum temperature in the uncontrolled room is significantly higher and the daily minimum temperature in the uncontrolled room is significantly lower than the controlled room temperature. Therefore, the water wall model is better than the concrete wall model in maintaining a stable temperature in the uncontrolled room under the winter condition. This is also true under the summer condition (refer to Fig. 4.8b). However, from the thermal comfort and energy consumption points of view, the concrete wall model is better than the water wall model during the late night and early morning in summer. The comparison of Figs. 8a and 8b also shows that the uncontrolled room air temperatures in both the water wall and concrete wall models are significantly higher than the controlled room temperature in summer, which indicates that both the water wall and concrete wall models have a worse overall performance in summer than that in winter.

Table 4.3 Comparisons of the time lags in the water wall and concrete wall models under the different climate conditions.

Climate conditions	Water wall (hour)	Concrete wall (hour)
Winter	5.45	4.48
Summer	5.08	4.45

The time lags of the daily peak temperature calculated for the water wall and concrete wall models are also shown in Fig. 4.8, which compares the time histories of the averaged air temperature in the uncontrolled room against that of the prescribed Sol-air temperature in Day 7. Clearly the time lag is larger in the water wall model than that in the concrete wall model under both climate conditions, which means that the uncontrolled room air temperature responds to the switch of the thermal forcing more quickly in the concrete wall system than that in the water all

system. A quantitative comparison of the time lags in the water wall and concrete wall models under the different climate conditions is given in Table 4.3. It is found in this table that the concrete wall model results in a similar time lag to that of the water wall model under both climate conditions. It is also seen in Table 4.3 that the time lags resulting from the concrete wall system in winter and summer are almost the same, whereas the time lag resulting from the water wall model in summer is clearly less than that in winter.

Fig. 4.9 depicts the calculated heat fluxes through Surface CS in the water wall and concrete wall models under winter and summer climate conditions. Similar to that observed for the uncontrolled room air temperature, the fluctuation of the heat fluxes is evidently smaller in the water wall model than that in the concrete wall model. It is seen that both the water wall and concrete wall models produce higher heat fluxes in summer than that in winter. Further, the heat fluxes are positive throughout almost the whole thermal cycles under the summer condition, which means excessive heat must be removed by air-conditioning in order to maintain a comfort environment in the controlled room. In winter, however, the heat loss from the controlled room must be compensated by supplemental heating in order to maintain thermal comfort. It can be seen in Fig. 4.9 that negative heat flux occurs for approximately half of the diurnal cycle in the concrete wall model in winter, whereas the occurrence of negative heat flux is insignificant in the water wall model. This comparison indicates that the water wall model has a better thermal performance than the concrete wall model in winter.
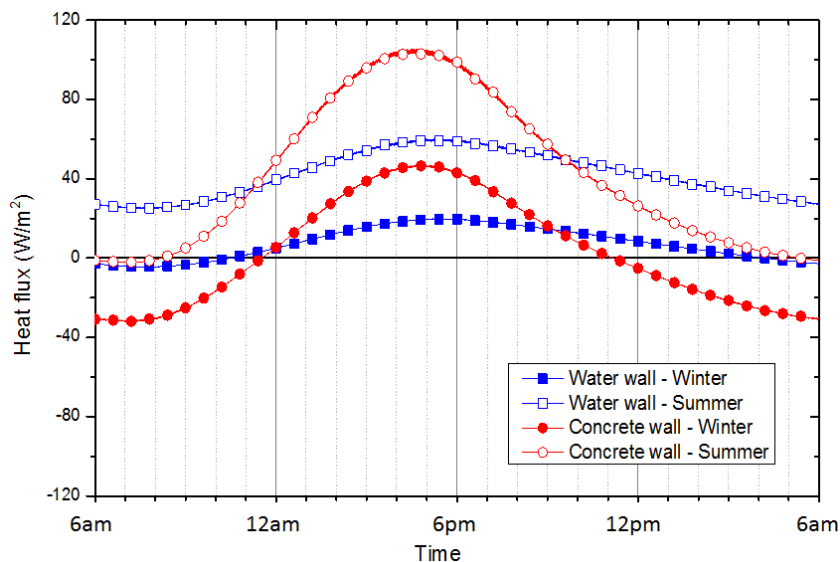

Fig. 4.9 Comparisons of the heat fluxes through Surface CS in the water wall and concrete wall models under the different climate conditions.

A further quantitative comparison of the supplemental energy consumptions in the water wall and concrete wall models under the different climate conditions is given in Table 4.4. It is clear that both the water wall and concrete wall models consume significantly more supplemental energy in summer than that in winter. The difference in the supplemental energy consumptions between the water wall and the concrete wall models is large in winter, but insignificant in summer.

Table 4.4 Comparisons of supplemental energy consumptions in the water wall and concrete wall models under the different climate conditions.

Climate conditions	Water wall (KJ/m^2)	Concrete wall (KJ/m^2)
Winter	63.11	897.94
Summer	3613.32	3652.93

4.4 Conclusions

In this study, the thermal performance of an opaque water wall system is numerically investigated for different thicknesses of the water column by means of unsteady CFD modelling for different thicknesses of the water column by means of transient CFD modelling for the climate of Sydney, Australia. To model the turbulence flows and radiation transfer in the water wall system, the shear-stress transport k-ω turbulence model and the Discrete Ordinates radiation model have been adopted. The present numerical results have revealed that the thermal stratification and the temperature fluctuation decrease with the increase of the water column thickness in the present water wall model under the typical winter climate condition in Sydney, Australia. The energy performance in terms of supplemental energy consumption is also enhanced by increasing the water column thickness. In addition, this study also shows that the thermal performance of the water wall in winter is better than that in summer since significantly less supplemental energy consumption is needed in winter. A comparison between the present water wall system and a conventional concrete wall system indicates that the temperature fluctuations are smaller in the water wall system than that in the concrete wall system for both winter and summer climate conditions, and a relatively larger time lag is found in the water wall model for both climate conditions considered. The water wall system requires significantly less supplemental energy for space heating than that of the concrete wall in winter, whereas both the water wall and concrete wall systems have similar energy performance in summer. Therefore, it

is concluded that an opaque water wall system is more suitable than a concrete wall system for regions with climate conditions similar to the winter condition in Sydney, Australia.

References

Albanese, V., Robinson, S., Brehob, G. & Sharp, K., 2012. Simulated and experimental performance of a heat pipe assisted solar wall. Solar Energy, 86, 1552-1562.

ASHRAE, 1975. Procedure for Determining Heating and Cooling Loads for Computerized Energy Calculations : Algorithms for Building Heat Transfer Sub Routines. New York: ASHRAE.

Balcomb, J.D. & McFarland, R.D., 1978. A simple empirical method for estimating the performance of a passive solar heated building of the thermal storage wall type. In 2nd National Passive Solar Conference. Philadelphia, PA, 1978.

Dutt, D.K., Rai, S.N., Tiwari, G.N., & Yadav, Y.P., 1987. Transient analysis of a winter greenhouse. Energy Conversion and Management, 27 (2), 141-147.

Fluent Inc., 2011. ANSYS FLUENT User's Guide. USA.

Gupta, A. & Tiwari, G.N., 2002. Computer model and its validation for prediction of storage effect of water mass in a greenhouse: a transient analysis. Energy Conversion and Management, 43(18), 2625–2640.

Karabay, H., Arıcı, M. & Sandık, M., 2013. A numerical investigation of fluid flow and heat transfer inside a room for floor heating and wall heating systems. Energy and Buildings, 67, 471-478.

Kaushik, S.C. & Kaul, S., 1989. Thermal comfort in buildings through a mixed water-mass thermal storage wall. Building and Environment, 24, 199-207.

McFarland, R.D. & Balcornb, J.D., 1979. Effect of design parameter changes on the performance of thermal storage wall passive systems. In Third national passive solar conference. San Jose, California, 1979.

Menter, F.R., 1994. Two-Equation Eddy-Viscosity Turbulence Models for Engineering Applications. AIAA Journal, 32, 1598-1605.

Modest, M.F., 2013. Radiative Heat Transfer. 3rd ed. New York: Academic Press.

Moustafa, M.A. & Aripin, S., 2014. CFD evaluation of the pottery water wall in a hot arid climate of Luxor, Egypt. Journal of Green Building, 9(4), 175-189.

Nayak, J.K., Bansal, N.K. & Sodha, M.S., 1983. Analysis of passive heating concepts. Solar Energy, 30, 51-69.

O'Callaghan, P.W. & Probert, S.D., 1977. Sol-Air temperature. Applied Energy, 3, pp.307-311.

Robinson, B.S. Chmielewski, E. Knox-Kelecy, A. Brehob, G. Sharp M.K., 2013. Heating season performance of a full-scale heat pipe assisted solar wall. Solar Energy, 87, 76-83.

Robinson, B.S. Sharp M.K., 2014. Heating season performance improvements for a solar heat pipe system. Solar Energy, 110, 39–49.

Ruivo, C. R., Ferreira, P. M., & Vaz, D. C., 2013. Prediction of thermal load temperature difference values for the external envelope of rooms with setback and setup thermostats. Applied Thermal Engineering, 51(1), pp.980-987.

Sodha, M.S., Kaur, J., Sawhney R.L., 1992. Effect of storage on thermal performance of a building. International Journal of Energy Research, 16 (8), 697-707.

Tiwari, G.N. & Singh, A.K., 1996. Comparative studies of different heating techniques of a non-air conditioned building. Building and Environment, 31, 215-224.

Wilcox, D.C., 1998. Turbulence Modeling for CFD. La Canada, California: DCW Industries, Inc.

Wu, T. & Lei, C., 2015a. On numerical modelling of conjugate turbulent natural convection and radiation in a differentially heated cavity. International Journal of Heat and Mass Transfer, 91, 454-466.

Wu, T. & Lei, C., 2015b. Thermal modelling and experimental validation of a semi-transparent water wall system. To be submitted.

Yumrutas, R., Kaska, O. & Yıldırım, E., 2007. Estimation of total equivalent temperature difference values for multilayer walls and flat roofs by using periodic solution. Building and Environment, 42, 1878–1885.

5. Conclusions and Future Work

Due to the concerns with global energy crisis and climate change, passive solar technologies for saving energy in buildings have attracted a growing research interest in recent years. The adoption of water wall as a passive solar strategy has a huge potential to maintain thermal comfort in buildings while reducing energy consumption. However, the present literature review has revealed that, although much attention has been paid to the water wall research, the understanding of the various water wall systems is still incomplete. More specifically, the majority of the previous water wall investigations have adopted a simple heat balance model (HBM), in which both internal and external convective heat transfer coefficients are assumed constant and the internal surface-to-surface radiation transfer is often neglected. Moreover, few studies have reported Computational Fluid Dynamics (CFD) modelling of water wall systems, and the limited existing CFD studies were all performed for steady state conditions only.

In order to fill the gaps in water wall research and provide advanced understanding of the complex flow and heat transfer processes in water wall systems, a comprehensive transient heat balance model (THBM) of a semi-transparent water wall system and an unsteady CFD model of an opaque water wall system have been developed in this project. The THBM has been validated against both field data and a DesignBuilder model, and the CFD model has been validated against the experimentally validated THBM. Using the validated models, the thermal performance of the above-mentioned two common configurations of water wall systems is investigated under different climate conditions in Sydney, Australia. The major findings from the present work are summarised in Section 5.1 below. Further, recommendations for future investigations on this and other related research topics are made in Section 5.2.

5.1 Major Research Outcomes

5.1.1 THBM of a Semi-transparent Water Wall System

The thermal performance of a semi-transparent water wall system is investigated using the THBM, which is validated by both DesignBuilder and a small-scale experiment under real

climate conditions in Sydney, Australia. In the present THBM, time variations of both internal and external convective heat transfer coefficients, the radiation emitted by external surfaces and the internal surface radiation exchanges are all accounted for. The results from the THBM simulation are compared with filed measurements, and a generally good agreement is achieved. In order to further validate the THBM, a concrete wall system is also investigated using the THBM and DesignBuilder. Again, a good agreement between the THBM prediction and field data is achieved.

The validated THBM is then used to examine the thermal performance of the semi-transparent water wall system under different configurations. The control parameters considered here include the transmissivity of the Perspex panel, the thickness of the water column and the attenuation coefficient of solar radiation in water. The major findings are:

- Over-heating has occurred in the room of the semi-transparent water wall system for approximately 112 hours out of the 504-hours of the testing period from 11 May to 31 May 2015.

- A significantly lower water and air temperatures are achieved by reducing the transmissivity of the Perspex panel(s). This strategy is particularly effective in reducing the diurnal maximum air temperatures.

- Increasing the thicknesses of the water column can reduce the fluctuation of the water temperature and the daily peak air temperature of the room, whereas adding different colour dyes into water has a limited impact on the water and air temperatures.

- Reducing the transmissivity of the semi-transparent panel(s) provides the most effective, practical and economical way to mitigate over-heating in the semi-transparent water wall system among the three strategies considered in this study. This can be achieved by tinting the external and/or internal surfaces of the semi-transparent panels. Furthermore, among the three tinting arrangements on the Perspex panel(s), attaching tint to the outside Perspex panel offers the most cost effective way to reduce the number of over-heating hours.

5.1.2 CFD Modelling of an Opaque Water Wall System

The investigation of the thermal performance of an opaque water wall system is carried out by a transient CFD model. For this purpose, the accuracy of five different two-equation eddy-viscosity models in resolving convective flows is firstly evaluated in a differentially heated cavity, and the effect of internal surface-to-surface radiation transfer is also quantified. It is

found that the shear-stress transport (SST) k-ω model has the best overall performance among the five selected RANS (Reynolds Averaged Navier-Stokes) turbulence models, and radiation exchanges between the internal surfaces have a significant impact on the predicted thermal stratification in the interior of the cavity. Therefore, the SST k-ω turbulence model and the Discrete Ordinates radiation model have been adopted in this study.

In the CFD model of an opaque water wall system, sol-air temperature is specified on the external surface to account for the effects of solar radiation and external convective heat transfer. The CFD model is validated against the above-described and experimentally validated THBM, and a fair agreement between the CFD model and the THBM results is achieved. The validated CFD model is then adopted to assess the thermal performance of the opaque water wall system with different thicknesses of the water column. The performance of the water wall system is also compared with that of a concrete wall system under different climate conditions. The major findings of this study are:

- Increasing the water column thickness in the opaque water wall system reduces the thermal stratification and the temperature fluctuation in both the water column and room air and enhances the energy performance in terms of supplemental energy consumption.

- Less supplemental energy consumption is needed in winter than that in summer for the present water wall system.

- The present water wall system has a smaller temperature fluctuation than a conventional concrete wall system under both winter and summer climate conditions, and the concrete wall system responds to the switch of thermal forcing more quickly than the water all system.

- In terms of energy performance, the water wall system is better than the concrete wall in winter, whereas both the water and concrete wall systems have similar performance in summer.

5.2 Future Work

Whilst the present research based on a coupled analytical, experimental and numerical program has made significant contributions to the understanding of the thermal performance of water wall systems under different climate conditions, several assumptions are embedded in the present models in order to simplify the problem. There are also a number of topics

worth investigating in order to further advance the understanding of water wall systems. Some recommendations for future work are given below.

It is found in Chapter 2 that both the wall to wall radiation and the conduction through the horizontal surfaces may affect the temperature and velocity profiles in the air-filled differentially heated cavity. However, only the effect of the surface radiation has been examined in this thesis. It would be useful if the conduction through the horizontal walls is included in future work. This may provide an alternative to prescribed temperature conditions on the horizontal surfaces for numerical simulation.

The THBM approach described in Chapter 3 assumes a bulk value for the attenuation coefficient of solar radiation in water across the entire wavelength range. In real-life situation, however, the attenuation coefficient of solar radiation in water depends on the wavelength. Therefore, a multiple-waveband attenuation model (e.g. Hattori et al., 2014) is worth investigating in order to obtain more accurate results. In addition, the effects of heat conduction through the roof and floor are neglected in the present THBM, which may have some influence on the simulated results. It is worth including this effect in further investigations. In other words, it is worth extending the present THBM from 1D to 2D. Furthermore, the refractive index and reflection of radiation by the Perspex and insulation panels is also neglected in the present THBM, and may be included in further work.

In Chapter 4, diurnal solar radiation and temperature variations at the outside Perspex panel are assumed to be standard sinusoidal functions of time in the present CFD model of the water wall system. It will be more relevant to practical applications to apply a realistic thermal boundary condition on the external surface based on the climate data. It is also necessary to extend the present 2D CFD model to a full 3D one, in which the Solar Load model available in ANSYS FLUENT may be adopted. In addition to the opaque outside Perspex panel in the water wall system which has been studied in the present thesis, other configurations of water wall system, such as a semi-transparent outside Perspex panel coupled with an opaque inside Perspex panel is also worth investigating.

Further experimental investigations considering different tinting arrangements on the Perspex panel(s), adding different colour dyes into water, and adopting a full-scale prototype of an opaque water wall are worth pursuing in order to further validate the present CFD model and the THBM. Experimental measurements of the attenuation coefficient of solar radiation in water with different colour dyes are also needed since it may be significantly different from the attenuation coefficient of the artificial light in water.

Finally, the effects of a water wall coupled with other passive solar strategies, such as PCMs and solar chimney, are also worth investigating. A better interior thermal environment may be achieved by adopting hybrid passive solar systems under different climate conditions.

References

Hattori, T., Patterson, J. & Lei, C., 2014. Study of unsteady natural convection induced by absorption of radiation based on a three-waveband attenuation model. Journal of Physics: Conference Series, 530(1), 1-7.